FFI RAPPORT

SIMVEX 2001 TRIAL - SPECTRAL IR MEASUREMENTS

BRENDHAGEN Erik, HEEN Lars Trygve

FFI/RAPPORT-2002/04911

FFIE/801/131

Approved
Kjeller 11. December 2002

Stian Løvold
Director of Research

SIMVEX 2001 TRIAL - SPECTRAL IR MEASUREMENTS

BRENDHAGEN Erik, HEEN Lars Trygve

FFI/RAPPORT-2002/04911

FORSVARETS FORSKNINGSINSTITUTT
Norwegian Defence Research Establishment
P O Box 25, NO-2027 Kjeller, Norway

FORSVARETS FORSKNINGSINSTITUTT (FFI)
Norwegian Defence Research Establishment

P O BOX 25
N0-2027 KJELLER, NORWAY

UNCLASSIFIED

SECURITY CLASSIFICATION OF THIS PAGE
(when data entered)

REPORT DOCUMENTATION PAGE

1) PUBL/REPORT NUMBER	2) SECURITY CLASSIFICATION	3) NUMBER OF PAGES
FFI/RAPPORT-2002/04911	UNCLASSIFIED	132
1a) PROJECT REFERENCE	**2a) DECLASSIFICATION/DOWNGRADING SCHEDULE**	
FFIE/801/131	-	

4) TITLE

SIMVEX 2001 TRIAL - SPECTRAL IR MEASUREMENTS

5) NAMES OF AUTHOR(S) IN FULL (surname first)

BRENDHAGEN Erik, HEEN Lars Trygve

6) DISTRIBUTION STATEMENT

Approved for public release. Distribution unlimited. (Offentlig tilgjengelig)

7) INDEXING TERMS

IN ENGLISH:	IN NORWEGIAN:
a) Infrared	a) Infrarød
b) Ship signature	b) Skipssignatur
c) Spectral measurements	c) Spektrale målinger
d) Model validation	d) Modellvalidering
e)	e)

THESAURUS REFERENCE:

8) ABSTRACT

The ship signature model ShipIR/NTCS has been selected as a NATO standard. In 2001 several nations, including Norway, participated in the SIMVEX field trial arranged by NATO in Canada for validation of this model. The measurements were performed on a research vessel under different meteorological conditions, when the ship was sunlit and shaded, and also at night. Knowledge of the spectral distribution of signatures is essential when comparing images acquired with different IR cameras. This report presents spectral results from our high resolution FTIR spectroradiometer, Bomem DA5. Most of our measurements were made with a resolution of 0.5 wavenumbers. Using in-house software that enables correction of non-ideal properties of the spectroradiometer, we obtained improved absolute precision of calibrated spectra.

The FTIR results are most interesting for sources with strong spectral variations, like the ship's plume, sunlit surfaces and sea and sky backgrounds. We also measured the ship in positions giving specular sun reflection. Sea and sky backgrounds were measured at different elevations, and the sea spectra show a significant contribution from sky reflection. Results from our spectral measurements have been compared with ShipIR/NTCS predictions. By comparing the results from plume measurements with simulated spectra, using the Fascode atmospheric model, we have estimated the plume temperature and the concentration of the most important IR contributing molecules.

9) DATE	AUTHORIZED BY This page only	POSITION
11. December 2002	Stian Løvold	Director of Research

ISBN-82-464-0731-7

UNCLASSIFIED

SECURITY CLASSIFICATION OF THIS PAGE
(when data entered)

CONTENTS

APPENDIX

SIMVEX 2001 TRIAL - SPECTRAL IR MEASUREMENTS

1 INTRODUCTION

In September 2001 project 801 at FFI, IR-missiles, participated in the SIMVEX trial (Ship Infrared Model Validation EXperiment) in Halifax, Canada. FFI (Espen Stark[1]) has been a member of the NATO RTO/SET/TG16 group; "Infrared measurements and modelling for ship self defense" since year 2000. This group was organizing the SIMVEX trial. The TG16 group (and its predecessors TG06, RSG-5, and RSG-8) has selected the ship signature model ShipIR/NTCS (Naval Threat / Countermeasure Simulator) as a NATO standard (1). As a member of this group, the project has received the ShipIR/NTCS model and has started using it for generation of synthetic infrared images of ships and backgrounds. For simplicity ShipIR/NTCS will be referred to as ShipIR in this report.

For several years, the participating countries in TG16 have been exchanging validation data and results on the ShipIR model. This has resulted in a demonstrable improvement in prediction accuracy of the model. The project has contributed to this work with spectral measurements of ship plume signatures. The plume measurements were obtained during the NATO SWG/4 EW Trial in Stavanger, Norway in August 1999 (2). The improved ShipIR model will predict the ship signature more accurately under various conditions. On board a military ship with sufficient computing power, this could provide real time information on the ship's vulnerability to threat IR sensors (e.g incoming missiles with infrared seekers). The improved model will also provide more accurate information on the IR signature of a ship under design, or for an existing ship on the success of passive IR countermeasures in a set of standard environmental conditions.

The SIMVEX trial had two objectives:

1. Comparison of radiometric measurements from the various participating NATO countries in order to validate their methodology.

2. Collection of high quality UNCLASSIFIED radiometric data on a test ship for subsequent collaborative validation of the ShipIR model.

If measurements obtained by different countries do not agree, one can not assume the model to agree with the measurements. To fully understand the comparison, it is important that the same

[1] Lars Trygve Heen is currently the Norwegian TG16 member

quantities are compared. During the trial, comparisons were performed on a panel painted with high emissivity paint, and for the ship, CFAV Quest.

For the panel comparisons the quantities to be compared during the trial were; 3-5 μm and 8-12 μm equivalent blackbody temperature (corrected for atmosphere, e.g temperature at the target plane).

For the ship, 3-5 μm and 8-12 μm equivalent blackbody temperature of a part of the port hull was compared. In addition, the full-ship apparent radiant intensity contrast (not corrected for atmosphere) was calculated from the measured IR-images. The apparent radiant intensity contrast is not wholly comparable between different sensors due to differences in optical bandwidth. However, the results of different nations can be compared to some extent.

For the trial, a ship named CFAV Quest was made available by Canada. CFAV Quest is a research vessel belonging to the Defence Research & Development Canada Atlantic (DRDCA) in Halifax. The ship normally does acoustic, hydrographic and general oceanographic work. Figure 1.1 shows an image of the ship.

Figure 1.1 Image of the test ship, CFAV Quest

Results from the IR camera measurements performed by FFI are described in a separate report (3). The same report also describes ShipIR simulations that have been performed, and presents the results of the simulations and comparisons with the measurements.

This report will concentrate on the results of spectral measurements by a high resolution FTIR spectroradiometer. Our instrument is a DA5 spectroradiometer from ABB Bomem Inc (in the following referred to as Bomem). In chapter 2 we give a summary of the principal operation of the spectroradiometer, and we will present the signal processing required to obtain calibrated spectra at high radiometric precision. The theory behind our plume measurement analysis is also given. In chapter 3 we present technical data on our FTIR instrument, and describe

additional instrumentation required to obtain high quality results from the measurements. In chapter 4 a description of how the measurements were performed is given, and results from reference measurements are presented.

During the SIMVEX trial we measured the ship surface and plume as well as sea and sky backgrounds. Knowledge of the infrared properties of the atmosphere and the sea surface is important for the analysis of the ship measurements. We have therefore chosen to present our results from the sea and sky background measurements first, in chapter 5, which also includes comparisons with ShipIR simulations of the backgrounds.

In chapter 6 results from day and night time measurements of the ship surface are presented. During day time, sun illuminated and shaded parts of the ship were measured. We will also present comparisons between apparent temperatures calculated from measured spectra and ShipIR temperature predictions. In chapter 7 results from measurements of the ship plume are shown. The measured plume signatures are compared with simulated spectra using a plume model. In chapter 8 we give a summary of the results.

The report also contains some appendices. In Appendix A an overview of the SIMVEX runs is presented, including the most important meteorological parameters during the runs. Appendix B presents the spectral response of the FTIR spectroradiometer when the different detectors are used, and the line shape function given by instrument properties. A discussion of the signal to noise properties of the instrument is given in Appendix C.

2 FTIR OPERATIONAL PRINCIPLE AND CALIBRATION

In this chapter we present the operation principle of an FTIR spectroradiometer. First we describe how the apparent spectral radiance input to the instrument is related to the Fourier Transform of the output signal for an ideal interferometer. Then a description of procedures required to obtain a calibrated spectrum follows, including correction of distortions due to non-ideal properties of the instrument, such as wavenumber dependent optical phase shifts, non-linear properties of components and self emission from the instrument. Procedures to correct the effects of asymmetrical truncation of the measured signal are also presented. In the final part of this chapter we discuss how to interpret spectra calculated from measurements by the instrument.

A complete understanding of this theory is not required to benefit from the rest of this report, and readers that are primarily interested in results from the SIMVEX trial may skip this chapter.

2.1 FTIR Spectroradiometer principles

2.1.1 Ideal Michelson interferometer

The main component of the FTIR Spectroradiometer is a Michelson interferometer. A schematic drawing illustrating the operational principle of the instrument is shown in Figure 2.1. A collimated input beam is propagated through a beam splitter, which splits the beam to a fixed and a movable mirror. The interfering beams reflected from the mirrors are focused on a detector. The output signal from the detector is then amplified and digitized and stored in a computer. Beams from a white light source and a laser are also propagated through the optical system and detected with separate detectors. These signals control the mirror movement and the discrete sampling of the detector signal.

The principles of Michelson interferometers are well described in literature, for instance (4) or (5) (in Norwegian), but we will give a brief description here.

In the following description it is assumed that the solid angle of the source is greater than (or equal to) the collecting solid angle of the instrument, Ω.

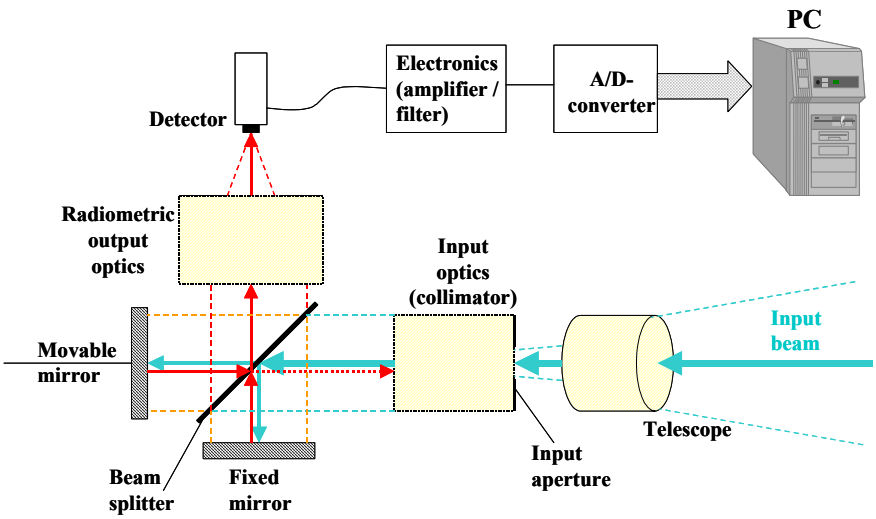

Figure 2.1 Schematic illustration of the Bomem DA5 FTIR operational principle

When radiation from a source is entering the interferometer, the output spectral power, (W/cm^{-1}), striking the detector is a function of the optical path difference x. For an ideal interferometer, the output spectral power is given by

$$P_{out}(x,\sigma) = A\Omega\tau(\sigma)N(\sigma)(1+\cos 2\pi\sigma x) \qquad (2.1)$$

where

$P_{out}(x,\sigma)$ - Interferometer output spectral power [W/cm^{-1}]
A - Area of the instrument aperture [cm^2]
Ω - Instrument collecting solid angle [sr]
σ - Wavenumber related to each spectral component in the radiation flux [cm^{-1}]
$N(\sigma)$ - Source apparent spectral radiance (i.e spectral radiance at input aperture) [W/(cm^2 sr cm^{-1})]
$\tau(\sigma)$ - Instrument spectral transmittance
x - Optical path difference between fixed and movable mirror [cm]

The term $A\,\Omega\,N(\sigma)$ in equation (2.1) is simply the spectral power at the interferometer input, denoted $P_{in}(\sigma)$, where[2]

$$P_{in}(\sigma) = A\,\Omega\,N(\sigma) \tag{2.2}$$

Equation (2.1) also contains a term that is independent of the optical path difference. The signal connected to this "DC-offset" in output spectral power, is removed by the instrument electronics, and will be omitted from this description.

The variable part of the output spectral power, which is received by the detector, is then for an ideal interferometer according to equations (2.1) and (2.2)

$$P_{out}(x,\sigma) = \tau(\sigma)\,P_{in}(\sigma)\cos 2\pi\sigma x \tag{2.3}$$

A detector in the instrument converts this output spectral power to a voltage (or a current) signal. This signal is normally called an interferogram. The relation between output spectral power and the interferogram is given by

$$I(x) = G\int_0^\infty P_{out}(x,\sigma)\,R_{\text{det}}(\sigma)\,d\sigma \tag{2.4}$$

where

[2] If the source solid angle at range R is less than the instrument's solid angle, Ω, the input spectral power is given by

$$P_{in}(\sigma) = A\left[\Omega_S\,N(\sigma) + (\Omega - \Omega_S)\,N_{bgr}(\sigma)\right]$$

where

Ω_S - Source solid angle (A_s/R^2) [sr]
$N_{bgr}(\sigma)$ - Background spectral radiance at input aperture

$R_{det}(\sigma)$ - Detector spectral responsivity [V/W]
G - Gain factor

The total Instrument Response Function (IRF) is defined by

$$R(\sigma) = G\ \tau(\sigma)\ R_{\text{det}}(\sigma) \tag{2.5}$$

According to equations (2.3), (2.4) and (2.5) the interferogram from an ideal interferometer is connected to the input spectral power by

$$I(x) = \int_0^\infty P_{in}(\sigma)\, R(\sigma) \cos(2\pi\sigma x)\, d\sigma \tag{2.6}$$

Solving this equation for the input spectral power, given the interferogram and the instrument response function, will according to equation (2.2) also determine the spectral radiance at the instrument's aperture.

Equation (2.6) shows that the interferogram will reach its maximum level when the optical path difference is zero. We will refer to this position of the movable mirror as "zero path difference" (ZPD).

2.1.2 Optical phase shift

Equation (2.6) applies for an ideal interferometer. In real instruments there will be a wavenumber dependent phase shift due to properties of optical components inside the instrument, which affects the interference between the two optical beams illustrated in Figure 2.1. For the DA5 instrument this phase shift is rather small, such that the interferogram will still have a well-defined peak. However, the calculated spectrum is sensitive to small phase shifts, such that a phase correction algorithm should be included in the signal processing of the measured interferogram.

To include the phase shift, we rewrite equation (2.6) as

$$I(x) = \int_0^\infty P_{in}(\sigma)\, R(\sigma) \cos\big(2\pi\sigma x + \varphi(\sigma)\big)\, d\sigma \tag{2.7}$$

where

$\varphi(\sigma)$ - Interferometer spectral phase shift function

The phase shift function complicates the procedure to determine the input spectral power, since the phase shift function must be known in order to obtain the input spectral power.

2.1.3 Non-linearity corrections

During the development of equation (2.6) and (2.7) it is assumed that the instrument response function, R(σ), is independent of the power absorbed by the detector. If not, there will be a non-linear relationship between the interferogram and the received power, especially near zero path difference, i.e near interferogram maximum. This effect will reduce the accuracy of calibrated measured spectra, if not corrected using an established model during the computing process.

Non-linearity is, in the literature, commonly attributed to the detector, but non-linearity in electronic amplifiers will give an equal effect. Our instrument is equipped with a CdHgTe (CMT) detector and an InSb detector, which are described in section 3.2.

For an ideal detector the output signal should be proportional to the intensity of the optical beam reaching the detector. For a real CMT detector a non-linear response is normally observed. Figure 2.2 shows the non-linear response of the CMT detector in our FTIR spectroradiometer.

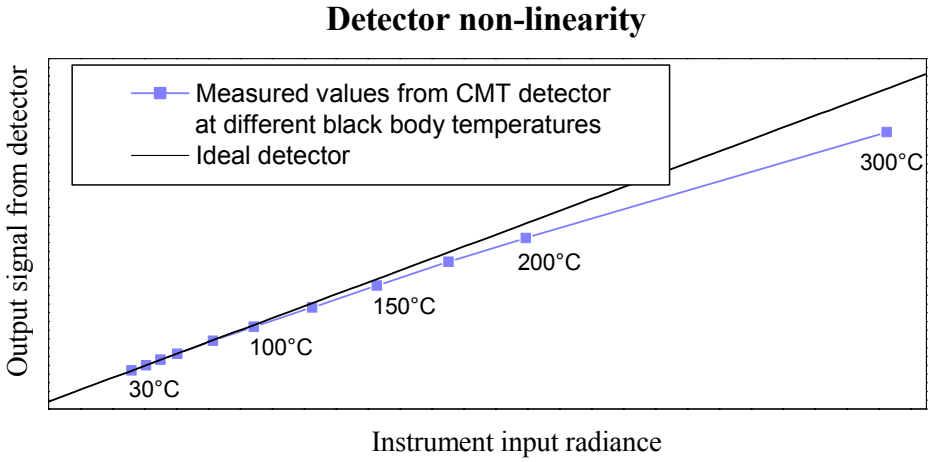

Figure 2.2 Non-linear response of the CMT detector used in FFI's spectroradiometer

The non-linear response may be reduced, but so far not removed, by careful design of the preamplifier system. In an FTIR instrument, the effect of the non-linearity is artifacts introduced in the calculated spectrum. Different methods for correcting non-linear response have been proposed, (6) and (7). At FFI we have developed our own method for non-linearity characterization and correction (8), based upon a combination of the work presented in the

cited references. The detector responsivity as a function of intensity is modelled as a quadratic function. Three or more blackbody measurements are used to determine coefficients for performing a correction. At least one of the reference measurements should be of a source at high temperature where the non-linearity effect is clearly visible. We have used a maximum temperature of 300°C, which is the upper temperature limit of our blackbody. Correction of non-linearity is most important when calibrating spectra from high temperature sources. The remaining part of the description of the signal processing of the measured interferogram assumes that the non-linear operation of the detector has been corrected. Figure 2.3 illustrates the effect of non-linearity corrections, when reference measurements of blackbodies at 30°C and 100°C were used to calibrate the measurement of a blackbody at 300°C.

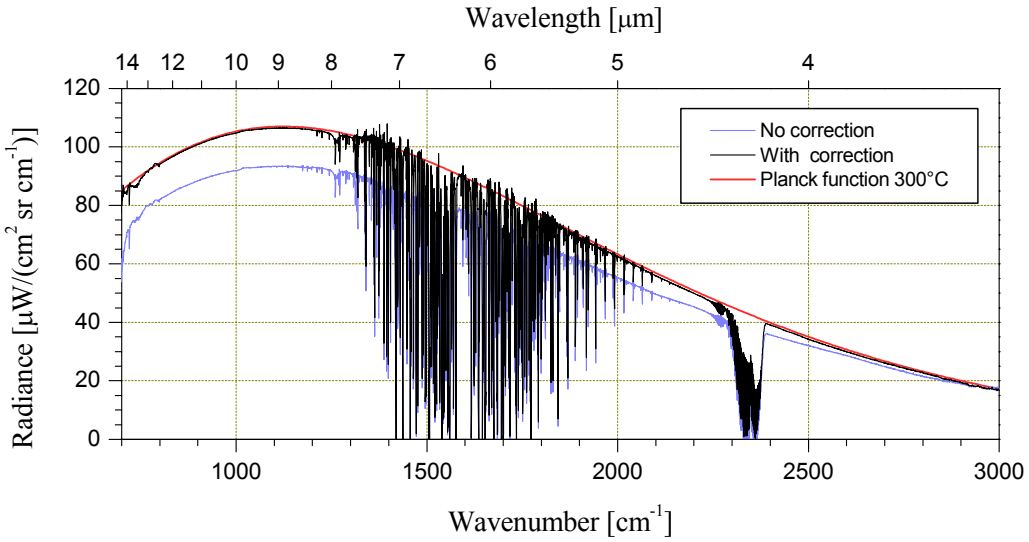

Figure 2.3 Effect of non-linearity correction on a measurement of a blackbody at 300°C

2.1.4 Electronics and Fourier transformation

The interferogram from the detector is filtered and amplified by the electronics, and then converted to digital data that are stored in a PC during each measurement. In order to determine the input spectral power, equation (2.7) is transformed by analytic continuation introducing negative wavenumbers. The measured interferogram $I_m(x)$ is then related to the input spectral power $P_{in}(\sigma)$ by

$$I_m(x) = \tfrac{1}{2} \int_{-\infty}^{\infty} P_{in}(\sigma)\, R(\sigma)\, e^{i(2\pi\sigma x + \varphi(\sigma))}\, d\sigma \qquad (2.8)$$

Equation (2.8) shows that the input spectral power multiplied with the instrument response and phase function may be found by calculating the complex Fourier transform of the measured interferogram. This property is the origin of the term “Fourier Transform Spectroradiometer”. The calculated complex spectrum is then according to equation (2.2) related to apparent radiance by

$$S(\sigma) = \tfrac{1}{2} A\Omega N(\sigma) R(\sigma) e^{i\varphi(\sigma)} \tag{2.9}$$

where

S(σ) - Complex Fourier transform of measured interferogram [V/cm^{-1}]

The apparent spectral radiance from the source is then by complex conjugation given by

$$N(\sigma) = \frac{2\left|S(\sigma)\right|}{A\Omega R(\sigma)} \tag{2.10}$$

The process described to determine apparent spectral radiance requires that the interferogram is measured as a function of optical path difference in the interval [-x’, x’]; i.e a symmetrical truncation of the interferogram. The true radiance of any physical source is a function with infinite resolution, but the length of the truncation function defines the actual resolution of spectra calculated from FTIR measurements. When we use the term radiance in this report, we refer to the true radiance convolved with the Fourier transform of the associated symmetrical truncation function.

The requirement of a symmetrical truncation function is normally not fulfilled in high resolution FTIR spectroradiometers (including our DA5 instrument), leading to an increased computational complexity in solving equation (2.8). This problem is partly discussed in chapter 2.3.1.

As shown by equation (2.10) the instrument response function, R(σ), multiplied with two geometrical constants should be known to convert the calculated raw spectrum, S(σ), to received apparent spectral radiance. The accuracy in the resulting spectral radiance rests upon a precise determination of the instrument response function. The following sections 2.2 to 2.4 describe the different effects which must be taken into account in order to establish an accurate instrument response function.

2.2 Radiometric calibration principles for symmetrically truncated interferograms

2.2.1 Instrument self emission

Our deduction so far has assumed that only radiation originating from the source to be measured reach the detector. In a real instrument, radiation from components inside the instrument will also enter the optical path and contribute to the measured interferogram. This self emission is discussed in (4). The design of the instrument leads to a phase shift of π of the interferogram contribution originating from components on the detector side of the beam splitter. Radiation from the beam splitter material itself will induce a contribution to the interferogram with a phase shift of $\pi/2$. This property was probably unknown when reference (4) was written, but was described in (9), and later confirmed by several other authors. The consequence of these phase shifts is that the phases of the contribution to the spectrum from external and internal radiation as well as the total spectrum may all be different. Thus all spectra should be handled as complex data throughout the calibration process.

A method of correcting the self emission phase shift was presented in (9). We will now recall the main principles of this method, followed by a presentation of our implementation of the algorithms for the DA5 spectroradiometer.

By defining the instrument response function $R(\sigma)$ to be a real function, and assuming a symmetrically truncated interferogram, the calculated spectrum from a measured source may be written as[3]

$$\begin{aligned} S_m(\sigma)\, e^{i\varphi_m(\sigma)} &= R(\sigma)\left(N(\sigma)\, e^{i\varphi(\sigma)} + N_{SE}(\sigma)\, e^{i(\varphi(\sigma)+\varphi_{SE}(\sigma))}\right) \\ &= R(\sigma)\, e^{i\varphi(\sigma)}\left(N(\sigma) + N_{SE}(\sigma)\, e^{i\varphi_{SE}(\sigma)}\right) \end{aligned} \tag{2.11}$$

where

N	- Apparent radiance from an external source
φ	- Phase of the contribution to the spectrum originating from an external source
N_{SE}	- Self emission radiance from instrument components contributing to the interferogram
φ_{SE}	- Phase difference between contributions to spectrum originating from self emission and from an external source
S_m	- Modulus of the spectrum calculated from the measured interferogram
φ_m	- Phase of the spectrum calculated from the measured interferogram

[3] To simplify notation, the instrument response function in chapter 2.2 and 2.3 also includes the factor ½AΩ, see equation (2.9).

2.2.2 Self emission correction and calibration equations

The purpose of performing measurements with an FTIR instrument is to retrieve the spectral apparent radiance N(σ) of an external source from equation (2.11). The equation shows that a number of unknown parameters are included in the spectrum calculated from a measured interferogram: The instrument response function, R(σ), the self emission from the instrument $N_{SE}(\sigma)$, and the phase shifts of the external and internal contributions, φ(σ) and $\varphi_{SE}(\sigma)$. It might be possible to measure some of the unknown parameters, like the detector spectral response. But other parameters, such as the total optical throughput, self emission and phase shifts are difficult to measure or estimate directly.

In order to solve equation (2.11), reference measurements of sources with well-defined radiance are required. Blackbodies are used for this purpose. The spectral radiance of an ideal blackbody is given by the Planck's function

$$N_{BB}(\sigma) = \frac{2hc^2\sigma^3}{e^{\frac{hc\sigma}{k_bT}} - 1} \tag{2.12}$$

where

T - Temperature [K]
c - Vacuum speed of light, $3 \cdot 10^8$ m/s
h - Planck's constant, $6.63 \cdot 10^{-34}$ Ws^2
k_b - Boltzmann's constant, $1.38 \cdot 10^{-23}$ Ws/K

Measurements of two blackbodies at different temperatures are required to find the unknown parameters in equation (2.11). Since equation (2.11) is valid for symmetrically truncated interferograms only, the measured interferograms must consist of an adequate symmetrical part. By using the measured spectral values and the theoretical radiance functions for the two blackbodies in equation (2.11), we obtain two equations. By solving these equations we find the instrument response function, R(σ), the phase function associated with external radiation, φ(σ), the instrument self emission $N_{SE}(\sigma)$, and the phase difference $\varphi_{SE}(\sigma)$. R(σ) and φ(σ) are given as the modulus and phase respectively from the solution shown in equation (2.13). The complex self emission component is given by equation (2.14).

$$R(\sigma)\, e^{i\varphi(\sigma)} = \frac{S_{m,BBH}(\sigma)\, e^{i\varphi_{m,BBH}(\sigma)} - S_{m,BBC}(\sigma)\, e^{i\varphi_{m,BBC}(\sigma)}}{N_{BBH}(\sigma) - N_{BBC}(\sigma)} \tag{2.13}$$

$$N_{SE}(\sigma)\, e^{i\varphi_{SE}(\sigma)} = \frac{S_{m,BBC}(\sigma)\, e^{i\varphi_{m,BBC}(\sigma)}\, N_{BBH}(\sigma) - S_{m,BBH}(\sigma)\, e^{i\varphi_{m,BBH}(\sigma)}\, N_{BBC}(\sigma)}{S_{m,BBH}(\sigma)\, e^{i\varphi_{m,BBH}(\sigma)} - S_{m,BBC}(\sigma)\, e^{i\varphi_{m,BBC}(\sigma)}} \tag{2.14}$$

where

$S_{m,BBH}$ - Modulus of measured spectrum from hot blackbody
$\varphi_{m,BBH}$ - Phase of measured spectrum from hot blackbody
N_{BBH} - Radiance from hot blackbody
$S_{m,BBC}$ - Modulus of measured spectrum from cold blackbody
$\varphi_{m,BBC}$ - Phase of measured spectrum from cold blackbody
N_{BBC} - Radiance from cold blackbody

The apparent radiance from an external source may now be found by solving equation (2.11) with respect to N(σ)

$$N(\sigma) = \frac{S_m(\sigma)\, e^{i\varphi_m(\sigma)}}{R(\sigma)\, e^{i\varphi(\sigma)}} - N_{SE}(\sigma)\, e^{i(\varphi_{SE}(\sigma))} \qquad (2.15)$$

To get valid results from equations (2.13) to (2.15) it is assumed that both blackbodies and the external source all fill the instrument's field of view, and that all parts of the external source inside the field of view have the same radiance. If the latter condition is not fulfilled, the result should be interpreted as the average apparent radiance from all parts inside the field of view.

2.3 Effect of asymmetrical truncation

A high resolution FTIR spectroradiometer requires that the movable mirror is able to move a long path. This requirement causes large sizes of such instruments. To reduce the instrument size, the instrument may be constructed so that the movable mirror moves a long path at one side of the ZPD position, but only a short path on the other side. The Bomem DA5 instrument is constructed this way. The measured interferogram will thus have an asymmetrical truncation, a property that requires additional signal processing.

2.3.1 Phase correction algorithm

It is shown in (4) and (5) that asymmetrical truncation will lead to distortions of the spectrum when the FFT algorithm is applied on the interferogram, and the spectrum is calculated according to equation (2.10).

A method to completely correct distortions due to asymmetrical truncation, originally developed by Mertz (10), is also presented in (4) and (5). The principle of this method, called phase correction, is to use the symmetrical part of the interferogram to calculate the phase according to equation (2.13). Then the phase is interpolated to the desired spectral resolution,

and used to correct the spectrum calculated from the full interferogram according to the following equation

$$S_{pm}(\sigma) = \mathrm{Re}\left[\frac{S_m(\sigma)\, e^{i\varphi_m(\sigma)}}{e^{i\varphi(\sigma)}} \right] \tag{2.16}$$

where

S_{pm} - Phase corrected, measured spectrum
φ_m - Phase of spectrum calculated from the full, asymmetrical interferogram
φ - Phase of spectrum calculated from the symmetrical part of interferogram

Equation (2.16) is based on the fact that an asymmetrical truncation function always can be regarded as a sum of a symmetrical (even) and an antisymmetrical (odd) function. Their Fourier transforms are real and imaginary, respectively, giving the result in (2.16).

This phase correction algorithm requires that the phase is a slowly varying function. According to the physical properties causing a $\varphi(\sigma)$ phase shift, this condition should normally be fulfilled in spectral regions where the phase of the self emission contribution does not deviate from the external phase (i.e $\varphi_{SE}(\sigma) = 0$). The phase calculated from the symmetrical part of the interferogram then represents the correct phase of the external radiance contribution, $\varphi(\sigma)$.

In spectral regions where $\varphi_{SE}(\sigma)$ has significant values, the condition is also assumed to be fulfilled regarding this component separately. However, a closer look at equation (2.11) shows us that this condition may not be fulfilled when regarding the total phase of a measured spectrum, φ_m. Even though $\varphi(\sigma)$ and $\varphi_{SE}(\sigma)$ vary slowly, $N(\sigma)$ may vary rapidly when there are emission or absorption lines present. The consequence is that both the modulus and phase of $S_m(\sigma)$ may also vary rapidly, especially when the $N_{SE}(\sigma)$ contribution is a significant part of the total spectrum. In this case the phase calculated from the symmetrical part of the interferogram does not represents the correct phase of the external radiance contribution, $\varphi(\sigma)$.

The effect of applying an erroneous phase in the denominator of equation (2.16) when φ_m is not varying slowly, is a severe distortion of spectral lines. A typical example could be a spectrum from a cold, clear sky, when the instrument including the beam splitter has a higher temperature than the sky. The effect of the distortions is shown in Figure 2.4, where the black curve is the spectrum calculated by applying this method in a spectral region where $\varphi_{SE}(\sigma)$ has significant values. The blue curve in this figure will be discussed in section 2.4.

2.3.2 Phase correction using pre-stored phase

A solution to eliminate these distortions, also included in standard software for the DA5 instrument (11), has been to use the symmetrical part of the interferogram measured from a high temperature blackbody to calculate the phase. If $N(\sigma) \gg N_{SE}(\sigma)$ in equation (2.11), the

measured phase φ_m is dominated by φ, and rapid variations in $N(\sigma)$ will only lead to small fluctuations of the phase. Assuming that the instrument phase function does not change from scan to scan, the calculated phase may be used to correct the phase of the complex spectrum from a low radiance source. The phase spectrum, determined using this method, $\varphi(\sigma)$, is not the correct phase spectrum to determine the spectral radiance from the external source, $N(\sigma)$, using equations (2.16) and (2.8). In addition, the instrument's internal spectral radiance, $N_{SE}(\sigma)$, and the phase $\varphi_{SE}(\sigma)$ is not known, since only one high temperature blackbody is used. The consequence is reduced precision of calibrated spectra.

2.4 FFI implementation of calibration and phase correction for asymmetrically truncated interferograms

We have so far seen that distortions due to self emission phase shifts may be corrected for symmetrically truncated interferograms, by using measurements from two reference sources in addition to the external source measurement, and complex data signal processing. We have shown that applying the Mertz phase correction directly upon asymmetrically truncated interferograms results in distortions if there are rapid spectral phase shifts in the total interferogram (external source radiation plus self emission). These distortions are partly, but not completely, removed by using the phase obtained from a high temperature source when performing phase correction on a spectrum calculated from a low radiance source measurement.

To improve the precision of calibrated spectra measured with the DA5 spectroradiometer, FFI has developed a method based upon a combination of the principles described in the previous sections. Our method is designed to remove distortions due to self emission phase shifts, even for asymmetrically truncated interferograms.

2.4.1 Differential phase correction

The method is still based on the assumption that the operation of the instrument is so stable, that the phase function does not change from one measurement to another. We recall from equation (2.13) that the phase associated with external sources, which should be slowly varying, could be determined using the difference between two blackbody measurements. By using the symmetrical parts of the measured interferograms from the two blackbodies to calculate the phase, a low resolution, slowly varying phase, $\varphi(\sigma)$, associated with the external radiation is found. The phase is interpolated to the resolution corresponding to the full interferograms, and applied in equation (2.16) as phase correction to all measured spectra. We recall that the Fourier transform of an asymmetrically truncated interferogram also includes a contribution given by the antisymmetrical part of the truncation function. To include this contribution, equation (2.11) should be rewritten as

$$S_m(\sigma)\, e^{i\varphi_m(\sigma)} = R(\sigma)\begin{pmatrix} N(\sigma)\, e^{i\varphi(\sigma)} + i\, B(\sigma)\, e^{i\varphi(\sigma)} + \\ N_{SE}(\sigma)\, e^{i(\varphi(\sigma)+\varphi_{SE}(\sigma))} + i\, B_{SE}(\sigma)\, e^{i(\varphi(\sigma)+\varphi_{SE}(\sigma))} \end{pmatrix} \tag{2.17}$$

$$= R(\sigma)\, e^{i\varphi(\sigma)}\left[\left(N(\sigma) + i\, B(\sigma)\right) + \left(N_{SE}(\sigma) + i\, B_{SE}(\sigma)\right) e^{i\varphi_{SE}(\sigma)}\right]$$

where

B - Apparent radiance from an external source convolved with the Fourier transform of the antisymmetrical part of the truncation function

B_{SE} - Self emitted radiance from instrument, contributing to the interferogram, convolved with the Fourier transform of the antisymmetrical part of the truncation function

When applying phase correction (i.e equation (2.17)) to equation (2.16) we obtain

$$S_{pm}(\sigma) = \mathrm{Re}\left[\frac{S_m(\sigma)\, e^{i\varphi_m(\sigma)}}{e^{i\varphi(\sigma)}}\right]$$

$$= R(\sigma)\, \mathrm{Re}\left[\frac{e^{i\varphi(\sigma)}\left(N(\sigma) + i\, B(\sigma) + N_{SE}(\sigma)\, e^{i\varphi_{SE}(\sigma)} + i\, B_{SE}(\sigma)\, e^{i\varphi_{SE}(\sigma)}\right)}{e^{i\varphi(\sigma)}}\right] \tag{2.18}$$

$$= R(\sigma)\left(N(\sigma) + N_{SE}(\sigma)\cos\varphi_{SE}(\sigma) - B_{SE}(\sigma)\sin\varphi_{SE}(\sigma)\right)$$

Regarding the effect on the contributions from asymmetrical truncation when performing phase correction, we observe that the term $B(\sigma)$ is removed, but the term $B_{SE}(\sigma) \sin \varphi_{SE}(\sigma)$ remains in the expression. Still, it is usually possible to remove the effect of this term in the final, calibrated spectrum. If the time between the measurements of the blackbodies and the external source is short, the instrument self emission is assumed to remain stable. The terms $N_{SE}(\sigma) \cos \varphi_{SE}(\sigma)$ and $B_{SE}(\sigma) \sin \varphi_{SE}(\sigma)$ should then be constant during all three measurements. Thus the difference between these terms is also a constant. Using the phase corrected, measured values for both blackbody measurements and the external source; equations (2.13) to (2.15) may be transformed to the following equations.

$$R(\sigma) = \frac{S_{pm,BBH}(\sigma) - S_{pm,BBC}(\sigma)}{N_{BBH}(\sigma) - N_{BBC}(\sigma)} \tag{2.19}$$

$$N_{SE}(\sigma)\cos\varphi_{SE}(\sigma) - B_{SE}(\sigma)\sin\varphi_{SE}(\sigma) = \frac{S_{pm,BBC}(\sigma)\, N_{BBH}(\sigma) - S_{pm,BBH}(\sigma)\, N_{BBC}(\sigma)}{S_{pm,BBH}(\sigma) - S_{pm,BBC}(\sigma)} \tag{2.20}$$

$$N(\sigma) = \frac{S_{pm}(\sigma)}{R(\sigma)} - \left(N_{SE}(\sigma)\cos\varphi_{SE}(\sigma) - B_{SE}(\sigma)\sin\varphi_{SE}(\sigma)\right) \tag{2.21}$$

Applying these equations to the calculated spectra obtained from the blackbody and external source measurements, the external source radiance is found from equation (2.21). The spectral resolution is defined by the symmetrical part of the truncation function associated to the asymmetrical truncation function applied during the measurements.

The blue curve in Figure 2.4 shows a spectrum calculated with the method presented in this section, phase corrected with the phase found from the difference between the symmetrical parts of two blackbody interferograms. As discussed in section 2.3.1, the black curve was phase corrected using the erroneous phase found from the symmetrical part of the external source interferogram. The figure shows that the line shape is clearly improved when using differential phase correction. In addition, the total precision of the signal level is improved.

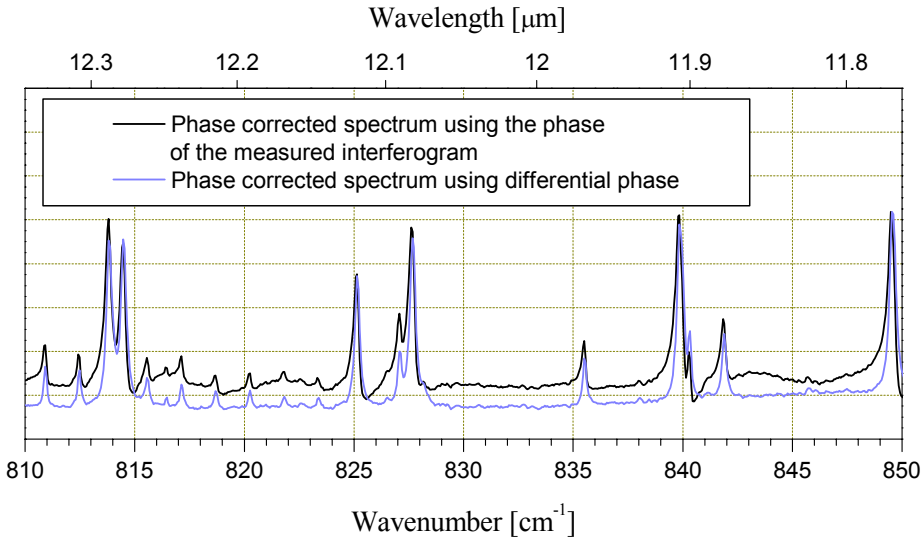

Figure 2.4 *High resolution spectrum from a clear sky measurement. Comparison of spectra calculated using the measured interferogram's own phase and differential phase calculated from blackbody measurements*

Application of equations (2.19) to (2.21) represent a general solution for processing asymmetrically truncated interferograms. The method is in principle only valid if the same resolution is applied to both blackbody and external source measurements, since all functions are related to the length of the applied truncation function. If the number of averaged interferograms is the same for all measurements, the noise level of all three phase corrected spectra will be the same. This might lead to an unnecessary high noise level of the calibrated spectrum.

In practice, valid results may be obtained, and the noise level may be reduced, when shorter interferograms (lower resolution) are used for blackbody measurements than for the external source. Since the instrument is purged with nitrogen during the measurements, both $R(\sigma)$ and

$N_{SE}(\sigma)$ are expected to be smooth, slowly varying functions. Thus equations (2.19) and (2.20) may be evaluated with lower resolution than for the external source. The calculated calibration functions are then interpolated to the desired resolution and applied to equation (2.21). Due to absorption in the short path from the blackbodies through the telescope to the instrument aperture, spectral lines might appear in the blackbody spectra. The effect of these lines is also strongly reduced during this interpolation process.

We will make one more comment on the expression $N_{SE}(\sigma) \cos \varphi_{SE}(\sigma) - B_{SE}(\sigma) \sin \varphi_{SE}(\sigma)$, evaluated in equation (2.20) and applied in equation (2.21). Practical experience from our DA5 instrument indicates that $\varphi_{SE}(\sigma)$ only differs from zero in a part of the 8-12 μm band, where the atmospheric transmittance is high. The contribution from the expression $B_{SE}(\sigma) \sin \varphi_{SE}(\sigma)$ in our instrument seems to be so small that it may be regarded as negligible throughout the entire spectral range covered by the instrument's beam splitter.

Numerical examples of calculated spectral responsivity and instrument self emission are presented in appendix B for both detectors.

2.5 Interpretation of calculated spectra

2.5.1 Definition of terms

In the previous sections we have used the term "apparent spectral radiance", which refers to the radiance received at the sensor. Similarly we use the term "apparent temperature" for the temperature of a blackbody which has a spectral radiance equal to the apparent spectral radiance from the source. The apparent temperature is found by solving equation (2.12) with respect of T, which gives

$$T_{app}(\sigma) = \frac{hc\sigma}{k_b \ln\left(\frac{2hc^2\sigma^3}{N_{app}(\sigma)} + 1\right)} \tag{2.22}$$

when using the apparent radiance $N_{app}(\sigma)$. Please note that the FTIR apparent temperature is a spectral function, reflecting the apparent spectral radiance function. For IR cameras the term is associated with the integrated radiance within the sensor's bandwidth.

When atmospheric transmittance and path radiance are known, measured spectra may be corrected for the influence of the atmosphere, such that the calculated spectrum will refer to the radiance at the target location. We use the term equivalent temperature, also a spectral function, for the temperature of a blackbody that has a spectral radiance equal to the spectral radiance from the target at the target position.

Later in this report we frequently use the term “radiance” when describing the apparent spectral radiance received from an object, and the term “integrated radiance” when describing the apparent spectral radiance integrated over a specific optical band.

2.5.2 Correction for atmospheric transmittance and path radiance

The measured apparent spectral radiance from a target covering the solid angle of the instrument (calibrated), $N_{ct}(\sigma)$ is given by

$$N_{ct}(\sigma) = N_t(\sigma)\,\tau_{atm}(\sigma, x_t) + N_{atm}(\sigma, x_t) \tag{2.23}$$

where

N_t - Target radiance (emitted plus reflected)
τ_{atm} - Atmospheric transmittance
x_t - Range to target
N_{atm} - Sensor to target path radiance

The spectral radiance from the atmospheric path between target and sensor (assuming a horizontal path with constant temperature) is given by

$$N_{atm}(\sigma, x_t) = \left(1 - \tau_{atm}(\sigma, x_t)\right) N_{BB}(\sigma, T_{atm}) \tag{2.24}$$

where

T_{atm} - Atmospheric temperature
N_{BB} - Spectral radiance from a blackbody

Equation (2.23) may then be written as

$$N_{ct}(\sigma) = N_t(\sigma)\,\tau_{atm}(\sigma, x_t) + \left(1 - \tau_{atm}(\sigma, x_t)\right) N_{BB}(\sigma, T_{atm}) \tag{2.25}$$

When the meteorological conditions have been measured, T_{atm} is known, and $\tau_{atm}(\sigma, x_t)$ may be found using an atmospheric modelling tool such as FASCODE (12) or MODTRAN (13). When using FASCODE, line information for all molecules is taken from the HITRAN database (14). The spectral radiance from the target may then be found (when $t_{atm}(\sigma, x_t) \neq 0$), using

$$N_t(\sigma) = \frac{N_{ct}(\sigma) - \left(1 - \tau_{atm}(\sigma, x_t)\right) N_{BB}(\sigma, T_{atm})}{\tau_{atm}(\sigma, x_t)} \tag{2.26}$$

Similarly, the radiance from the background (at range x_t) is found using a calibrated background measurement. The usage of equation (2.26) is most relevant in spectral regions with good atmospheric transmittance, i.e $\tau_{atm}(\sigma, x_t)$ is close to 1. In spectral regions with strong absorption lines, the calculated $N_t(\sigma)$ will be sensitive to noise and calibration inaccuracies. Equation (2.26) is not usable when $\tau_{atm}(\sigma, x_t) = 0$.

When both the target and the background spectra have been measured, the contrast may be found using the difference between the measured spectra. The term $N_{atm}(\sigma, x_t)$ is then cancelled, and the contrast (i.e difference between spectral radiance from target and background) is given by

$$\Delta N_{tb}(\sigma) = \frac{N_{ct}(\sigma) - N_{cb}(\sigma)}{\tau_{atm}(\sigma, x_t)} \tag{2.27}$$

Assume that the target within a limited spectral band radiates as a blackbody. We may then replace $N_t(\sigma)$ in equation (2.25) with $N_{BB}(\sigma,T_{eq})$, where T_{eq} is the equivalent blackbody temperature of the target. If we introduce the spectral contrast radiance $\Delta N(\sigma)$ as the difference between radiances from blackbodies with target equivalent temperature and atmospheric temperature,

$$\Delta N(\sigma) = N_{BB}(\sigma, T_{eq}) - N_{BB}(\sigma, T_{atm}) \tag{2.28}$$

equation (2.25) may be rewritten as

$$N_{ct}(\sigma) = N_{BB}(\sigma, T_{eq}) - \left(1 - \tau_{atm}(\sigma, x_t)\right) \Delta N(\sigma) \tag{2.29}$$

When the atmospheric transmittance is high and the contrast is low, $N_{ct}(\sigma)$ will be close to $N_{BB}(\sigma,T_{eq})$, and calculated apparent temperature will be close to the target equivalent temperature.

Numerical example for a typical SIMVEX run: If the equivalent temperature of the target is 20°C, the atmospheric temperature 17°C, and the atmospheric transmittance within a selected band is 0.9, the calibrated spectrum gives an apparent temperature of 19.7°C, only 0.3°C from the equivalent temperature.

For many SIMVEX runs, the temperature contrasts are lower than in this example. For most runs the atmospheric transmittance is higher than 0.9 in parts of the spectrum. Since the errors in most of our spectra are expected to be 0.5-1°C (discussed in section 4.2.2), a conversion of the results from apparent to equivalent temperature will in most cases not have any significant impact on the interpretation of the results.

2.5.3 Interpretation of plume measurements

As mentioned earlier, a condition for the preceding deduction is that the measured target fills the entire field of view. During the SIMVEX trial we measured the ship plume. The size of the plume was so small that only a fraction of the field of view was filled. The instrument will then also see radiation from the background covering the rest of the field of view. In spectral regions where the emission from the plume is low, a contribution from the background is also transmitted through the plume. This scenario requires an extension of the expressions presented in the previous section. The following deduction is made with help from (15).

If the plume fills the field of view, and the contribution from the background transmitted through the plume is taken into account, the calibrated spectrum from a plume measurement is given by

$$N_{cp}(\sigma) = \left(N_p(\sigma) + N_b(\sigma)\,\tau_p(\sigma)\right)\tau_{atm}(\sigma, x_t) + N_{atm}(\sigma, x_t) \tag{2.30}$$

where

N_p - Radiance from the plume
τ_p - Transmittance of the plume
N_b - Radiance from the background

If the plume does not fill the field of view, the fraction of the field of view covered by the plume, ω, should be included in the calculations. This fraction is given by

$$\omega = \frac{A_p}{\Omega_S\, x_t^2} \tag{2.31}$$

where

A_p - Estimated area of the plume
Ω_S - Field of view of the FTIR spectroradiometer (2.7 mrad)

The calibrated spectrum is then given by

$$N_{cp}(\sigma) = \left(\omega\, N_p(\sigma) + \omega\, N_b(\sigma)\,\tau_p(\sigma) + (1-\omega)\, N_b(\sigma)\right)\tau_{atm}(\sigma, x_t) + N_{atm}(\sigma, x_t) \tag{2.32}$$

assuming that the fraction of the field of view *not* filled by the plume, 1-ω, has the same radiance as the background behind the plume, $N_b(\sigma)$

The calibrated spectrum from the background measurement is given by

$$N_{cb}(\sigma) = N_b(\sigma)\,\tau_{atm}(\sigma, x_t) + N_{atm}(\sigma, x_t) \tag{2.33}$$

The measured radiance difference between the plume and the background (the plume contrast) is then

$$\Delta N_{cpb}(\sigma) = \omega \left(N_p(\sigma) - (1 - \tau_p(\sigma))\, N_b(\sigma) \right) \tau_{atm}(\sigma, x_t) \tag{2.34}$$

We see that the calculated contrast includes a contribution from the background, and we will analyze this expression further.

If the plume is assumed to be in thermodynamical equilibrium with temperature T_p, the radiance from the plume is given by

$$N_p(\sigma, T_p) = \varepsilon_p(\sigma)\, N_{BB}(\sigma, T_p) \tag{2.35}$$

where

$N_{BB}(\sigma,T_p)$ - Radiance from a blackbody with temperature T_p
$\varepsilon_p(\sigma)$ - Spectral emittance of the plume

The radiance from the background is given by

$$N_b(\sigma, T_b) = \varepsilon_b(\sigma)\, N_{BB}(\sigma, T_b) \tag{2.36}$$

where

$N_{BB}(\sigma,T_b)$ - Radiance from a blackbody with temperature T_b
$\varepsilon_b(\sigma)$ - Spectral emittance of the background

In section 5.2 we will see that equation (2.36) is actually a simplification, since the plume is seen against a sea background, which also includes sky radiation reflected from the sea. However, the background may still be modelled by equation (2.36) by adjusting $\varepsilon_b(\sigma)$.

Further, assuming that the reflectance of the plume is zero, we have

$$\varepsilon_p(\sigma) = 1 - \tau_p(\sigma) \tag{2.37}$$

Equation (2.34) may then be written as

$$\Delta N_{cpb}(\sigma) = \omega\, \varepsilon_p(\sigma) \left(N_{BB}(\sigma, T_p) - \varepsilon_b(\sigma)\, N_{BB}(\sigma, T_b) \right) \tau_{atm}(\sigma, x_t) \tag{2.38}$$

For a typical ship plume we have $T_p \gg T_b$, and thus $N_{BB}(\sigma,T_p) \gg N_{BB}(\sigma,T_b)$. In spectral regions where $\varepsilon_p(\sigma) \approx 1$ we have

$$\Delta N_{cpb}(\sigma) \approx \omega\, N_{BB}(\sigma, T_p)\, \tau_{atm}(\sigma, x_t) \tag{2.39}$$

If the temperature of the plume is known, or can be estimated with reasonable precision, a more precise calculation of the radiance from the plume is possible. If we use equations (2.33), (2.35) and (2.37), equation (2.34) may be transferred to

$$\Delta N_{cpb}(\sigma) = \omega\, \varepsilon_p(\sigma) \left(N_{BB}(\sigma, T_p)\, \tau_{atm}(\sigma) - N_{cb}(\sigma) + N_{atm}(\sigma) \right) \tag{2.40}$$

Combining equation (2.40) with (2.24) we obtain the following expression

$$\Delta N_{cpb}(\sigma) = \omega\, \varepsilon_p(\sigma) \left[\left(N_{BB}(\sigma, T_p) - N_{BB}(\sigma, T_{atm}) \right) \tau_{atm}(\sigma, x_t) + N_{BB}(\sigma, T_{atm}) - N_{cb}(\sigma) \right] \tag{2.41}$$

From this expression we can find the plume emittance $\varepsilon_p(\sigma)$, using the measurements of the plume and the background, as well as the atmospheric transmittance calculated by FASCODE. The plume radiance is then given by (2.35).

3 INSTRUMENTATION

A detailed description of the instrumentation operated by FFI during the SIMVEX trial was given in (16). In this chapter we give an overview of those parts of our and other nations' instrumentation, from which data have been used during the analysis of the FTIR spectroradiometer data.

3.1 Test site

The measurements were performed at the FMF Cape Scott test facility (NESTRA) at Osborne Head (near Halifax), Canada. The participants were: Canada, USA, France, Italy, Poland, Denmark, The Netherlands and Norway. Figure 3.1 shows the facility with all the different measurement teams in position. The Norwegian equipment was operated from a 20 ft container equipped as a complete laboratory. During the measurements the FTIR spectroradiometer was placed on a platform in front of the container door, as shown in Figure 3.2. From this position, the sea could be observed over a wide range in azimuth angle. The instrument's altitude above sea level was 24.5 m.

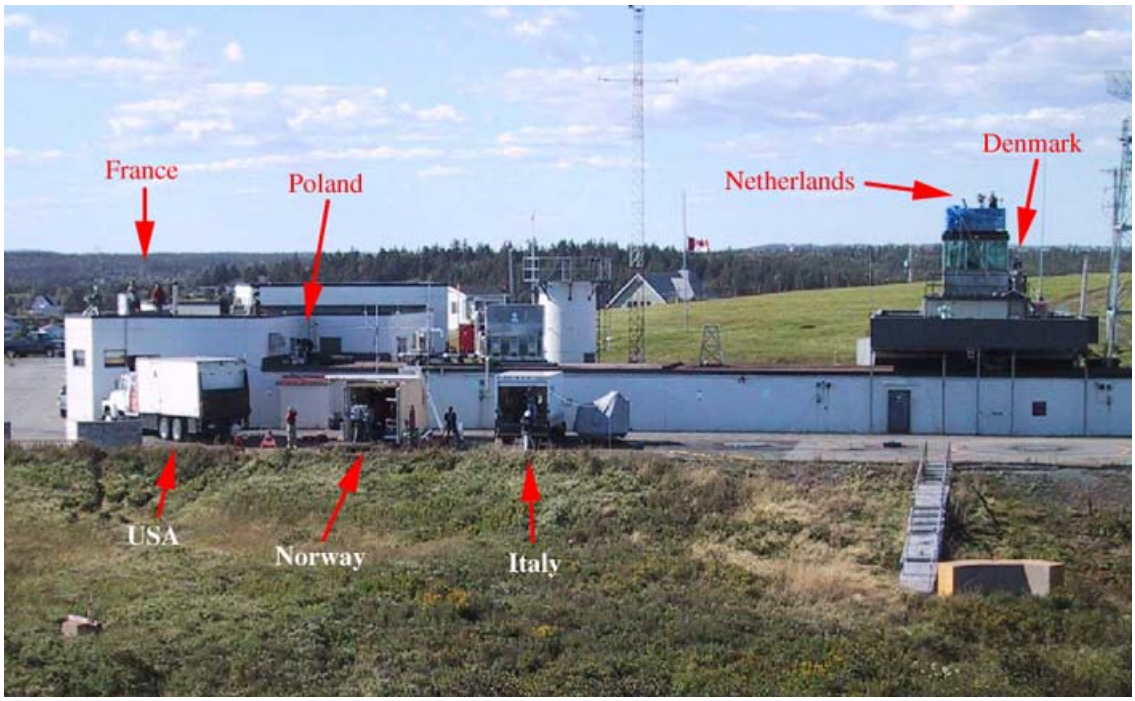

Figure 3.1 The NESTRA facility at Osborne Head, with all the different measurement teams in position

3.2 Operational data of the Bomem DA5 spectroradiometer

Our instrument is equipped with two detectors. The InSb detector covers the spectral range 1800-5000 cm^{-1} (2-5.5μm), while the CdHgTe (CMT) detector covers the range 700-5000 cm^{-1} (2-14 μm). However, the CMT detector is primarily used for the band covering 700-1400 cm^{-1} (7-14 μm), since the signal to noise ratio is much lower for this detector within the spectral band covered by the InSb detector. In our instrument the detectors cannot be used simultaneously. A physical replacement of the detector device is required to obtain results from both detectors. FFI has modified the cover of the instrument to simplify and speed up the replacement procedure. When operated, the detectors are cooled to liquid nitrogen temperature.

The beam splitter has a KCl substrate, with Ge/Sb_2S_3 coating

The maximum optical path difference during a mirror scan is 50 cm, giving a spectral resolution of 0.02 cm^{-1} (Bomem definition, (11)). This resolution is not practical to use at trials like SIMVEX, since long measurement times are required to obtain an acceptable signal to noise ratio. In most of the SIMVEX runs a resolution of 0.5 cm^{-1} was used. A few plume runs were recorded with resolution 0.2 cm^{-1}, while a resolution of 1.0 cm^{-1} was used for blackbodies and the FFI reference plate.

When the term “resolution” is used in this report, the term is related to the definition given in the previous paragraph, except when a different definition is stated. If a monochromatic wave

is applied as input, the line shape in the calculated spectrum is determined by the maximum optical path difference related to the selected resolution, and the apodization of the interferograms. The monochromatic instrument line shape function at resolution 0.5 cm^{-1} is presented and discussed in appendix B.

The mirror speed was 1 cm/s for all runs. At resolution 0.5 cm^{-1} the acquisition time for a single interferogram is then 1.1 s, and the interval between consecutive interferograms is 2 s. Even at this resolution averaging of several interferograms is required to improve the signal to noise ratio. For most measurements, an acceptable signal to noise ratio is then obtained for the 8-12 μm band using the CMT detector, and for the low wavenumber part of the 3-5 μm band using the InSb detector. Still, the signal to noise ratio in the high wavenumber part of the 3-5 μm band is not very good. To improve the visual impression, we have reduced the effective resolution of calculated spectra to 0.8 cm^{-1} for most of the InSb spectra presented in this report.

Figure 3.2 The Bomem DA5 Spectroradiometer in position for measurement on the platform outside the container

The instrument was configured such that raw data from all individual interferograms were stored on disk. Typically 150 interferograms were acquired during a ship run, giving a total measurement time of 5 minutes. Each measured part of the ship was aimed at for an interval of approximately 1 minute. This allows averaging of 25-40 interferograms in each calculated spectrum. In background measurements we acquired and averaged 64 interferograms in each run.

The aperture of the instrument input optics was set to 3.5 mm, which gives a field of view of 2.7 mrad, when Bomem's narrow angle telescope with diameter 25 cm is mounted.

3.3 Blackbodies

Two blackbodies of type HGH RCN 300 were used for reference measurements. The active surface of the blackbodies is 30×30 cm, and consists of a black-painted pyramid structure designed to increase the effective emissivity. The temperature controller does not include any active cooling, such that the blackbody may be operated between ambient and 300°C. The temperature is monitored by a thermocouple, and typical fluctuations of 0.5°C have been observed after the device has stabilized. The temperature settings used during the SIMVEX trial and a discussion of the emissivity are presented in section 4.2.1.

Figure 3.3 shows the blackbodies mounted on the inside of the container door. The blackbodies were mounted at the same height as the instrument telescope. This way the blackbodies could easily be brought into and out of the field of view by swinging the door and the instrument.

Figure 3.3 The two blackbodies mounted on the container door for FTIR reference measurements

Two black-painted plates, supplied by Naval Research Laboratory (NRL) and FFI, respectively, were also measured during the trial. These plates were neither heated nor cooled, but were supplied with I-buttons to monitor the temperature.

3.4 IR and CCD cameras

A JVC CCD camera mounted on the spectroradiometer provided images of the same field of view as the infrared detector. The images document the measured scenario, but are not practical to use for aiming the instrument due to the narrow field of view.

An operator manually aims the FTIR instrument when a moving object is measured. To ensure that the desired object is tracked, the operator needs to see a real time IR image of the scenario. An IR camera mounted on the same platform as the spectroradiometer provides this function. Unfortunately our camera (Amber Aurora) broke down before the trial, and was not returned from repair in time. We are grateful that we could borrow an Inframetrics Milcam camera from NRL instead. The Milcam camera, which operates in the 3-5 μm band, is the device to the right in Figure 3.4. The camera is used together with the Matrox 4sight device, described in the next section, to output an IR image that also shows the FTIR instrument's field of view. The field of view of the Milcam camera is 4.4 × 4.4°.

Figure 3.4 The Amber Sentinel and Inframetrics Milcam IR cameras

The camera to the left in the figure is our Amber Sentinel camera that operates in the 8-12 μm band. Images from that camera are not directly used in the FTIR data analysis. The camera is mounted on the same platform as the Milcam camera to ensure that both are aiming in the same direction. The results from the analysis of IR images from both cameras are presented in (3).

In our analysis of the plume measurements we have also used images from an Indigo Merlin 3-5 μm camera operated by NRL from a helicopter.

A Sony CCD camera mounted inside our container acquired visual images of the ship. During the runs, images from all cameras were recorded on digital video recorders.

3.5 Laser range finder and GPS reporting system

To calculate atmospheric transmittance and path radiance with FASCODE, the distance from shore station to ship must be known. During the SIMVEX trial this information was obtained in two ways. A laser rangefinder from Simrad Optronics was operated at the shore site, and the distance to the ship was measured frequently during the runs. In addition the position of the ship was continuously transmitted from a GPS receiver on board via radio link to the shore station. The distance was then calculated and displayed on a PC monitor by software developed by FFI.

3.6 Matrox 4sight unit

The Matrox 4sight unit is a programmable device that allows text and figures to be added into video images in real time. We use the device to put a circle in the IR image from the Milcam camera (17). The circle represents the spectroradiometer's field of view. The Matrox 4sight also logs a digital output signal from the spectroradiometer that indicates when interferograms are recorded. Signal status is displayed in the video image, and is used to synchronize acquired interferograms and IR images during data analysis. Data from the laser range finder is also read by Matrox 4sight, and displayed in the image. The FTIR synchronization signal and range are both stored on the local hard disk in the Matrox 4sight unit. Figure 3.5 shows an example of the output image from Matrox 4sight, with the Milcam IR image plus added information.

3.7 Meteorological stations

FFI operated a meteorological station mounted at the shore station. Knowledge of meteorological data is essential to run reliable FASCODE and ShipIR simulations. Air temperature and humidity are especially important in order to calculate atmospheric transmittance properly. The air temperature is also used for calibration of the FTIR measurements. This will be described in section 4.2.2. We also operated a meteorological station close to the shoreline that measured sea temperature in addition to data measured by the other station. Meteorological data measured during the SIMVEX runs are shown in appendix A. Description of the meteorological sensors in use, and more complete meteorological data, may be found in (3).

In addition to our own data we have also used data from meteorological sensors mounted on board the ship. For modelling of the sky we have further used radiosonde data from balloon launches collected by Environment Canada.

Figure 3.5 Output video image from the Matrox 4sight unit, showing the Milcam IR image with the FTIR field of view (red circle), plus additional text information

3.8 Sensors mounted on board the ship

Results from the ship surface FTIR measurements have been compared with temperatures measured by thermocouples and I-buttons mounted on board the ship. These sensors were mounted and operated by W. R. Davis Engineering Ltd. (in the rest of this report referred to as Davis). Davis also instrumented the ship with a gas analyzer, which measured temperature and concentration of specific molecules in the combustion gas leaving the stack outlet (18). Results from the latter have been compared with FTIR measurements of the plume.

4 MEASUREMENT PROCEDURES AND REFERENCE MEASUREMENTS

In this chapter we will discuss how the measurements were carried out, and show results from some reference measurements.

4.1 Run geometries

During the trial the ship made runs in different geometries. Positioned in front of the container we were able to measure all ship run geometries. For all runs the ship passed the waypoint at

the same distance from the shore station (1 km). From our position the ship was then surrounded by sea background. IR cameras were used to measure this background and the ship simultaneously, since both are present in the same images. With the FTIR instrument a measurement of the sea background was made immediately after each ship run.

Measurements of the ship were performed both at day and night time. At day time both shaded and sun illuminated parts of the ship were measured. The measurements were performed at 3 different geometries. Figure 4.1 shows a map of the area around Osborne Head including the nominal ship course for the 3 geometries A, B and C. The same geometries were used at the same time every day to study the influence of meteorological variations from day to day. To ensure that the ship reached thermal equilibrium, the ship was sailing at constant speed and heading for 30 minutes prior to passing the waypoint. Analysis performed by Davis (19) on surface mounted thermocouple data has shown that this time could be too short in some cases.

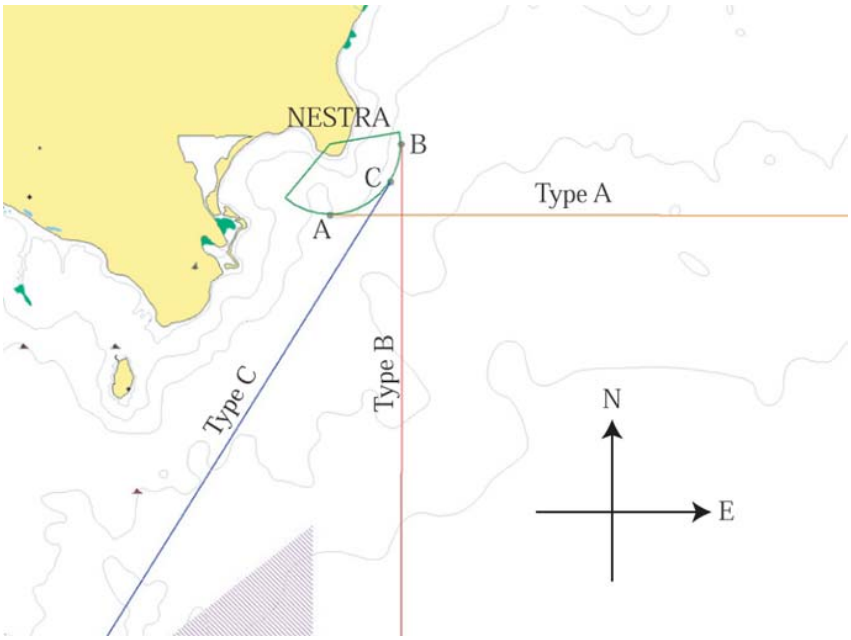

Figure 4.1 Map of the Osborne Head area showing the 3 different run geometries

Run type A was used early in the afternoon (around 18:30 UTC) to enable measurement of a shaded ship side. In this geometry there was an intense sun illumination of the front of the ship. Run type B was used at day time (17:00 UTC) when the sun was in a high position, but illuminating the ship hull at a narrow angle. Run type C was used later in the afternoon (21:00 UTC) when the sun was lower, but giving strong illumination of the shipside. In run types B and C the front of the ship was shaded. The same geometry as type C was used for measurements of the ship at night time (except that some runs were shorter). These runs are referred to as type D. Special runs were set up to measure the plume. The geometry was the same as run type C, but a higher engine power was used to maximize the plume intensity, which naturally increases the ship speed. A more detailed description of the geometries can be found in (3).

Measurements by the participating nations' IR cameras were primarily performed when the ship passed its waypoint and only the shipside was visible. Measurements of shaded and sun illuminated parts of the ship were made in separate runs (Type A and C). Since the field of view of the FTIR instrument only covers a small part of the ship, the instrument is not suitable for measuring the total radiant intensity of the ship, but the radiance and apparent temperatures of specific part may be measured. Regarding the FTIR measurements, we expected to get the best results for studying the influence of sun illumination, if shaded and sun illuminated parts of the ship could be measured in the same run. Any effect of calibration function variation and change in meteorological conditions would then be minimized. Thus we started the FTIR run at a distance of approximately 1500 m, about 5 minutes before the ship reached its waypoint. Thus there are small variations in the pitch angle between the horizon and the ship during an FTIR run, but the ship was always surrounded by sea background. First the front of the bridge was measured, followed by the ship hull and the side of the bridge. In most runs we also measured the funnel, and in some runs the stack outlet. The sea background was measured behind the ship, after the ship had passed the waypoint, usually in a new FTIR run.

Almost the same number of runs was measured with the CMT and the InSb detectors to cover the 8-12 μm and the 3-5 μm bands, respectively. Most of the days the same detector was used for the A, B and C runs and the first D run. The detector was then changed before the last D run. Thus we acquired D run data with both detectors on the same day.

Most of the results presented in chapter 6 are from type C and D runs, but some results from type A runs are also included.

The plume was also measured with both detectors, but the results presented in chapter 7 will show that only the InSb data were usable for analysis.

4.2 Procedures for radiometric calibration

4.2.1 Blackbody measurements

The method presented in chapter 2 has been used during the analysis of the SIMVEX measurements. The blackbody temperatures were set to 150°C and 30°C. The low temperature is chosen to be as close as possible to the measured targets, but sufficiently high to remain constant during the trial, independent of air temperature variations. The blackbody in use does not have any active cooling. The high temperature is chosen to give significant radiation within the bandwidth covered by each detector. The choice is a compromise between getting a reasonable signal to noise ratio at high wavenumbers and the precision of the nonlinearity correction of CMT detector measurements. Regarding the latter, a lower temperature of the hot blackbody would be preferable. Measurements of the reference blackbodies were made in

connection with every SIMVEX run. The selected temperatures enable calculation of the instrument response function, $R(\sigma)$, up to approximately 3500 cm^{-1}. In addition, single measurements of one blackbody at 300°C were made for each detector, before the official trial runs started. The spectral range up to 4800 cm^{-1} is then covered.

In order to get an exact calibration, the spectral emissivity of the blackbodies should also be included in the deduction in chapter 2. A measurement of emissivity of the blackbodies in use was presented in (3). The emissivity of the blackbodies is 0.99-1.00 through most of the 8-12 μm band, reaching a minimum of 0.98 close to 10 μm. Since there is some uncertainty in these results, we have chosen not to include any correction of the blackbody emissivity, thus assuming it to be equal to 1.

4.2.2 Precision improvement using properties of the atmosphere

A series of measurements of the blackbodies, the target and the background takes some time. In order to obtain high quality data, the calibration functions (instrument response and self emission) must remain stable during this interval. Experience from earlier trials has shown that stability may often be the factor limiting the achievable precision. This was also confirmed during the SIMVEX trial, for the FTIR results, as for the IR camera results described in (3). To monitor the variation of the calibration functions, we normally measured the blackbodies both before and after each ship run. By studying the difference in the calibrated spectra, an impression of the actual level of precision was obtained. The results show significant changes in the calibrated spectra; converted to apparent blackbody temperature difference of typically 1-4°C. But in the worst case (SIMVEX run 8) the change is more than 10°C.

To improve our precision we have implemented a method, using the knowledge of atmospheric properties as a third reference. In some spectral regions the atmospheric transmittance is very low. The consequence is that the measured spectrum is dominated by path emission from the atmosphere, independent of the object measured at long range. The correct spectrum should then equal the spectrum from a blackbody at atmospheric temperature. This fact is used to interpolate spectra calculated with different calibration functions, in order to get a good fit in selected spectral regions. We have tested this method on spectra from the FFI reference plate that will be presented in section 4.3.2. These tests and earlier experience have shown that significant improvement in absolute precision is also obtained in regions with good atmospheric transmittance, when this method is used.

The major challenge when using this method is temperature variations along the path between the instrument and the ship. We think the best choice is to use a spectral region where the total radiance is dominated by the atmospheric path between 10 and 100 m from the container, since the temperature here is considered to be close to the shore station temperature measurement. It is easiest to find a spectral region having this property when the CMT detector is used, but we have also used the method for InSb measurements. We estimate the radiometric precision to be

improved so that most measurements converted to apparent blackbody temperature, now have a maximum error of 0.5-1°C. For some runs the error may be up to 2°C.

The noise level in calculated spectra also limits the possibility to distinguish between spectra from objects with small radiance differences. A description of the noise properties of our instrument is given in appendix C.

4.2.3 Apparent temperature calculation

Later in this report many spectra will be shown. But since the spectral variations between many runs are quite small, not all measured spectra will be shown. Instead we have calculated apparent temperatures, which are presented in tables and figures and compared with temperature measurements on board the ship and ShipIR predictions.

Knowing the spectral apparent radiance from an object, the spectral apparent temperature may be calculated from equation (2.22). The apparent temperatures have been calculated in spectral regions where the atmospheric transmittance is high. According to equation (2.29), the difference between apparent and equivalent temperatures is very small when the temperature difference between ship and atmosphere is small. From our spectra we have calculated the apparent temperatures around 950 cm^{-1} for CMT runs, and close to 2100 cm^{-1} for InSb runs. The atmospheric transmittance is high in these regions, so that the apparent temperatures should represent the surface equivalent temperature quite well, normally within the estimated precision of the FTIR measurement.

For InSb runs the atmospheric transmittance is best in the region 2500-2700 cm^{-1}. However, this region is not optimal for apparent temperature calculations, due to reduced signal to noise ratio. For comparison, we have calculated an average apparent temperature for the spectral region 2600-2700 cm^{-1} for some InSb runs. In section 6.2.3 we will see that the choice of spectral region for apparent temperature calculations is important, when the measured object contains contributions from reflected sunlight.

To facilitate comparison of radiation from measured objects and Planck functions, we have included some Planck functions in most of our plots showing measured spectra. The blackbody temperatures of the plotted Planck functions are normally chosen to be close to the apparent temperatures of the measured objects. But usually the chosen temperatures do not exactly represent the best estimate of apparent temperature. This temperature choice would make the curves cover each other too much. To obtain the apparent temperature for a specific measurement, we recommend using the appropriate tables.

4.3 Reference measurements

In the following sections we present the results from measurements of reference plates that were used during the trial.

4.3.1 NRL plate

In order to compare the participating nations' methodology, the first days of the trial were spent performing measurements of a black painted reference plate prepared by NRL. The measurements were repeated several times, which allowed different sun heating conditions. The plate was also measured by the FTIR spectroradiometer, at a distance of 140 m. In order to test both detectors we made a measurement with one detector at the same time as the other teams measured with IR cameras. Then the detector was replaced, and the measurement was repeated.

Figure 4.2 shows spectra measured with the CMT detector for SIMVEX runs 2 and 4, and Figure 4.3 shows spectra measured with the InSb detector for SIMVEX run 3 plus an additional measurement performed with this detector 20 minutes after SIMVEX run 4. The results show that the spectra fit blackbody functions very well in spectral regions with high atmospheric transmittance.

In run 4 the plate was strongly illuminated by sun, which leads to a highly increased plate temperature. But deviation from blackbody even at high wavenumbers as in Figure 4.3 is very small compared to what we will show in chapter 6 for sun reflections off the ship. This result indicates that the emission coefficient of the plate is very high, and the plate may thus be regarded as a good blackbody source.

Table 4.1 summarizes the calculated apparent temperatures from the plate measurements and the actual temperature measured with a temperature sensor mounted on the plate. We see that for some measurements we have good agreement, while there is up to 4°C deviation for other measurements.

We believe that the reason for this deviation is temperature drift of the instrument. To minimize the time between measurements, we did not follow our normal calibration procedures with blackbody measurements both before and after the plate measurements.

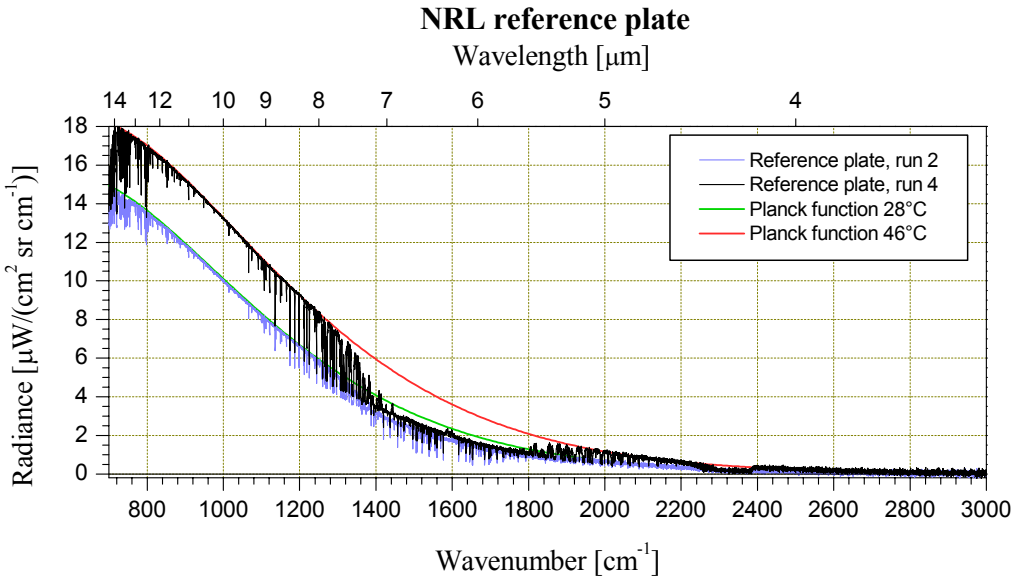

Figure 4.2 Two measurements of the NRL reference plate with the CMT detector, SIMVEX runs 2 and 4

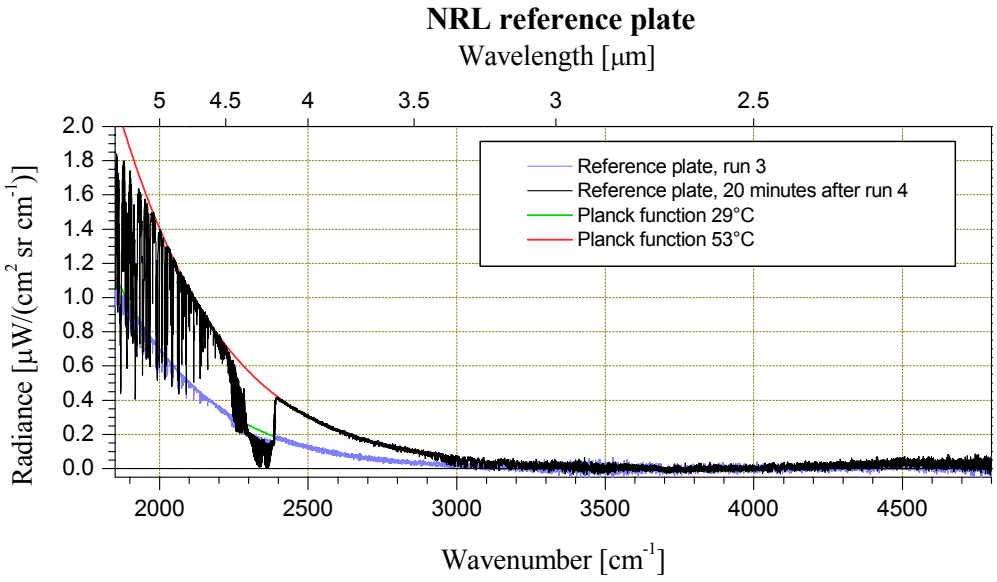

Figure 4.3 Two measurements of the NRL reference plate with the InSb detector, SIMVEX run 3 and a measurement 20 minutes after SIMVEX run 4

Date	Time (UTC)	SIMVEX run	Detector	I-button temperature [°C]	FTIR apparent temperature [°C]
11	16:30	1	CMT	24.3	25.5
11	18:35	2	CMT	27.4	27.4
11	19:06	Extra	InSb	32.3	36.5
12	14:59	3	InSb	27.1	29.0
12	15:27	Extra	CMT	27.6	24.2
12	17:59	4	CMT	46.5	45.8
12	18:22	Extra	InSb	50.1	53.0

Table 4.1 Comparison of NRL reference plate temperature measured by I-button and apparent temperature calculated from FTIR measurement

Therefore only a single set of calibration data was available, and we were unable to compensate any temperature drift. The absolute precision is then reduced. Since the time between the detector replacement and "Extra" runs was short, the temperature of the detector dewar surface and the atmosphere inside the instrument might not be stabilized. These factors will influence on the instrument self emission, and thus the absolute precision. For all ship and background measurements the calibration has included temperature drift correction, so that we believe the absolute precision should be according to the numbers in section 4.2.2.

4.3.2 FFI plate

FFI supplied a black painted reference plate that was mounted 15 m from the FTIR instrument on some of the trial days. At day time, while the sun was up, the temperature gradients across the plate were generally too high to use the plate as a reference. At night time the gradients were much smaller, and the plate was measured after the ship and background measurements during the type D runs on these days. Figure 4.4 and Figure 4.5 show the spectra from this plate measured with the CMT and InSb detectors respectively. The results show that the spectra fit blackbody functions very well in spectral regions with high atmospheric transmittance. Due to the short distance this is the case over broader spectral regions than for the NRL plate measurements. Figure 4.6 shows apparent temperatures calculated from the spectrum and temperatures measured with I-buttons mounted on the plate. The figure shows that the absolute precision of these measurements seems to be within 0.5°C for most of the runs, but up to 1°C for a couple of runs. We think that the precision obtained in these measurements should represent a lower bound on the precision of the ship measurements.

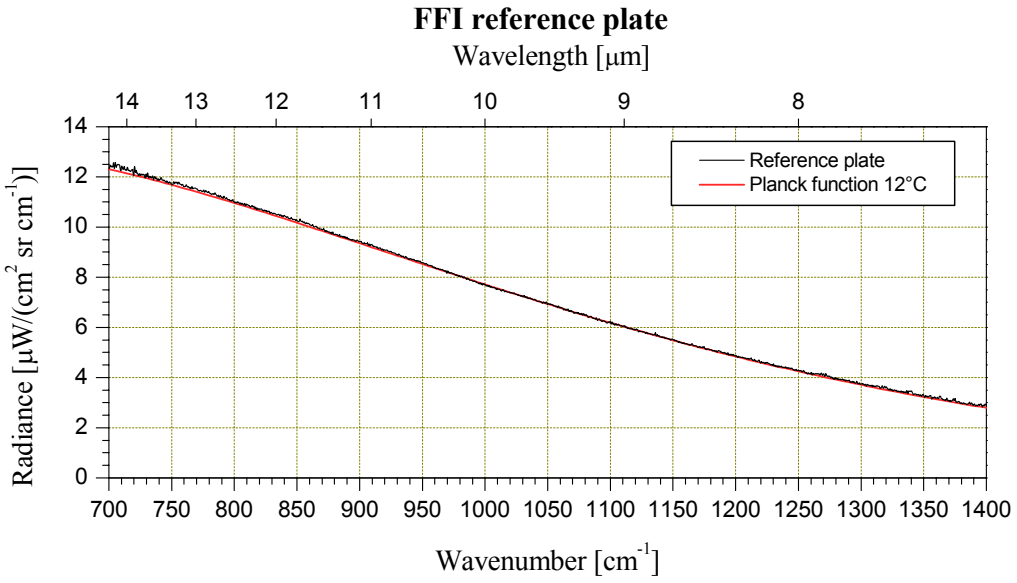

Figure 4.4 Measurement of the FFI reference plate with the CMT detector, SIMVEX run 35

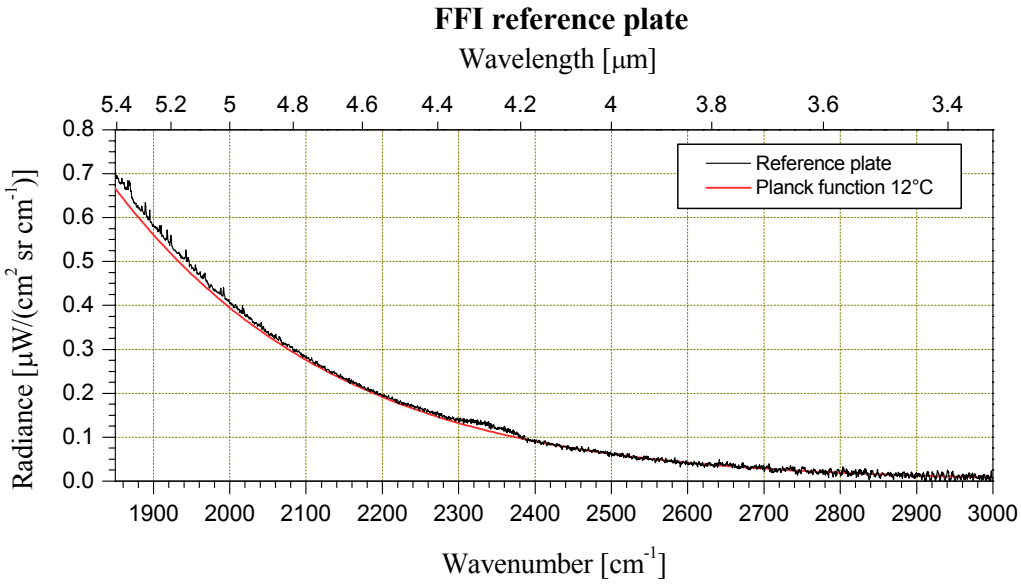

Figure 4.5 Measurement of the FFI reference plate with the InSb detector, SIMVEX run 34

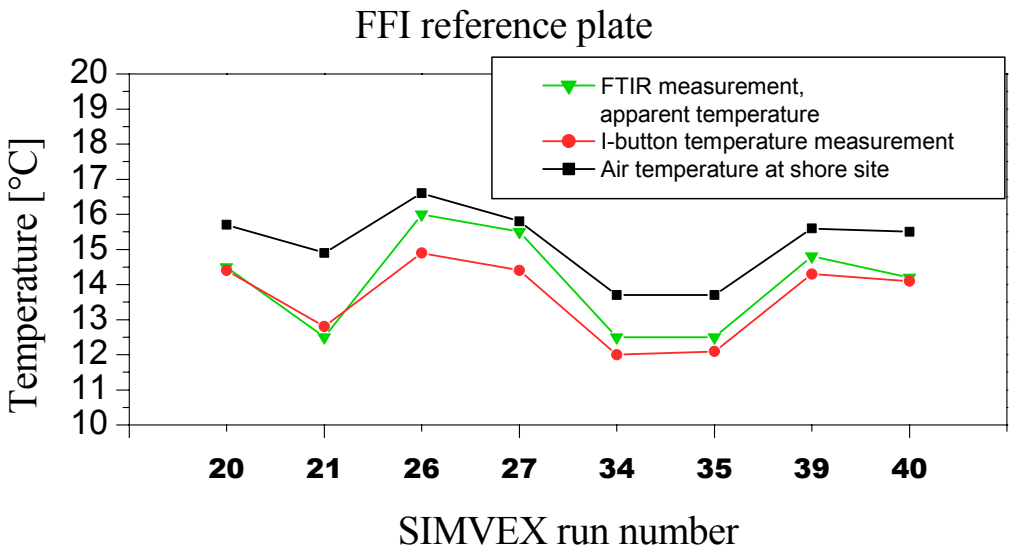

Figure 4.6 Comparison of FFI reference plate temperature measured by I-button and apparent temperature calculated from FTIR measurement

5 SEA AND SKY BACKGROUND MEASUREMENTS

In addition to sea background measurements made after each ship run, we made separate measurements of both the sea and the sky at different pitch angles. These measurements were carried out once during the trial for each detector. We have compared the results from the spectral measurements with ShipIR predictions. Sky measurements were also compared with FASCODE and MODTRAN calculations. A summary of the runs and meteorological parameters is presented in appendix A.

5.1 Sky background measurements

When the sky is clear, the radiance from the sky background is composed of radiation from emission lines and continuum contributions from different molecules in the atmosphere. The infrared signature of the sky then has strong spectral variations. In addition to meteorological conditions, the signature is dependent on the pitch angle, since the length of the atmospheric path (i.e the amount of emitting gas) contributing to the radiation varies with the angle. When observing the sky just above the horizon, the length of the path is very long, only limited by the curvature of the earth's surface. The signature then approaches a blackbody corresponding to the atmospheric temperature (assuming the temperature is constant along the path). When

increasing the pitch angle, the radiation decreases rapidly in spectral regions with high atmospheric transmittance, dependent on the meteorological conditions. Due to the earth's curvature the angle to the horizon was -0.16° from the position of the instrument at Osborne Head. Thus only the sky was inside the field of view when the instrument was set to aim at pitch angle 0°.

Figure 5.1 and Figure 5.2 show measured spectra of sky radiance in the 8-12 µm and 3-5 µm bands respectively, measured with the CMT and InSb detectors, respectively. For each spectral band the radiance from the sky at angles 0°, 1° and 15° is shown. The time interval between the first and the last measurement was approximately 15 minutes. When performing the CMT measurements, the air temperature was stable during this interval, around 17.2°C. The InSb measurements were performed on another day. The temperature then dropped from 15.5°C to 14.7°C during the measurement interval. Absolute humidity at sea level was 10 g/m^3 during the CMT measurements and 6.3 g/m^3 during the InSb measurements.

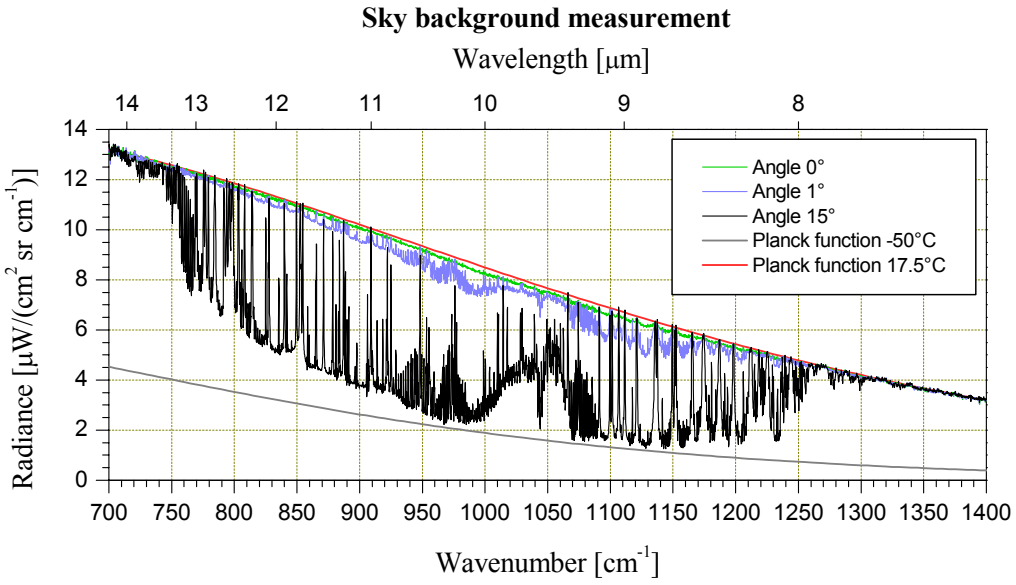

Figure 5.1 Radiance from the sky measured at different pitch angles with the CMT detector

The results confirm that the radiance from the sky is close to a blackbody at atmospheric temperature when looking close to the horizon. When looking up in the sky, there are spectral variations in accordance with atmospheric transmittance variations. In spectral regions with low atmospheric transmittance, for instance 1300-1400 cm^{-1}, the radiance is close to blackbody at all angles, as discussed in section 4.2.2.

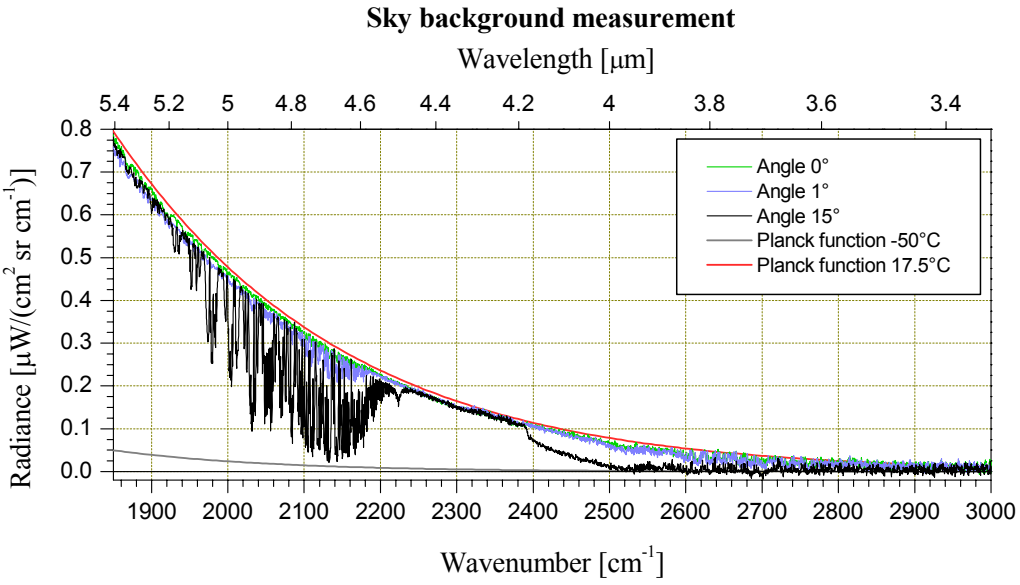

Figure 5.2 Radiance from the sky measured at different pitch angles with the InSb detector

5.2 Sea background measurements

Just before making the sky measurements described above, we also measured the sea radiance at different angles. Figure 5.3 and Figure 5.4 show the results from the measurements for the 8-12 μm and 3-5 μm bands, respectively, at angles -4° and -0.3°. The latter angle is just below the horizon. The sea temperatures measured close to the shore station during these measurements were 16.1°C and 16.7°C respectively.

The results show that we have the same spectral variations in the sea background signature as for the clear sky, although with reduced amplitude. The reason is reflection of sky radiance from the sea surface. At low angles the emissivity of the sea surface is not very high. In addition to emission from the sea surface given by the sea temperature, the total radiation includes a contribution of radiation reflected from the sky. The sea surface area that is covered by the instrument's field of view is quite large. Due to the wave structure of the sea, the surface reflects the sky over a wide range of angles, so that the total contribution from reflected sky radiance should be interpreted as the average of the covered surface. Analysis of individual interferograms recorded at the same angle during a run indicates that this average is quite stable. The measurement closer to the horizon (-0.3°) gives higher radiance than the -4° result. This result seems reasonable. When measuring the sea at a low angle, the contribution from reflected sky is more dominated by lower angles. The contribution from reflected sky radiance is still clearly visible, which is in accordance with observations by IR cameras. In IR images recorded in clear weather the horizon is usually seen as a distinct line, even when the

temperature of the sky and the sea is equal. IR images of the sea and sky backgrounds recorded by the Inframetrics Milcam (3-5 μm) and the Amber Sentinel (8-12 μm) cameras, respectively, are shown in Figure 5.5 and Figure 5.6.

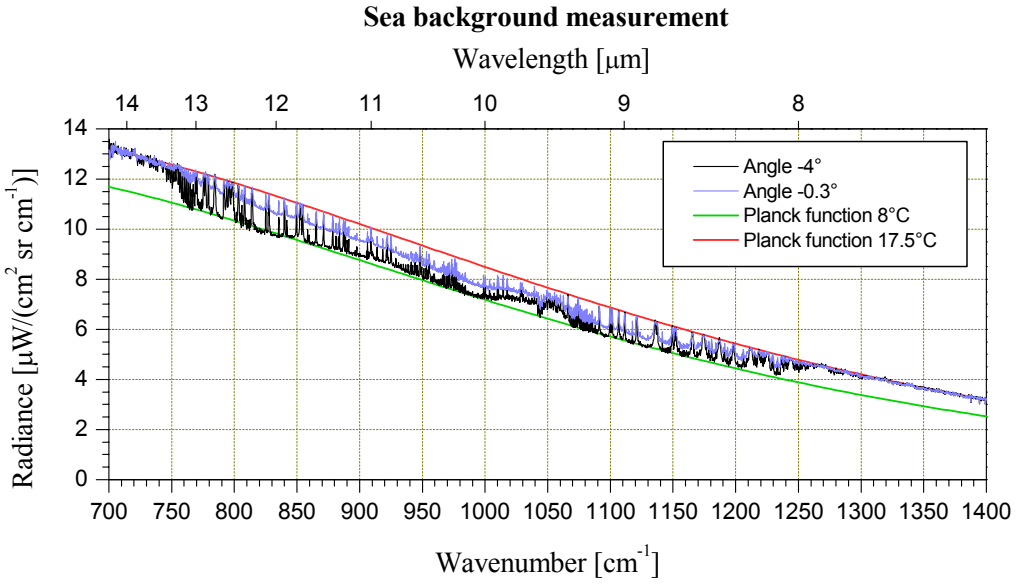

Figure 5.3 Radiance from the sea measured at different pitch angles with the CMT detector

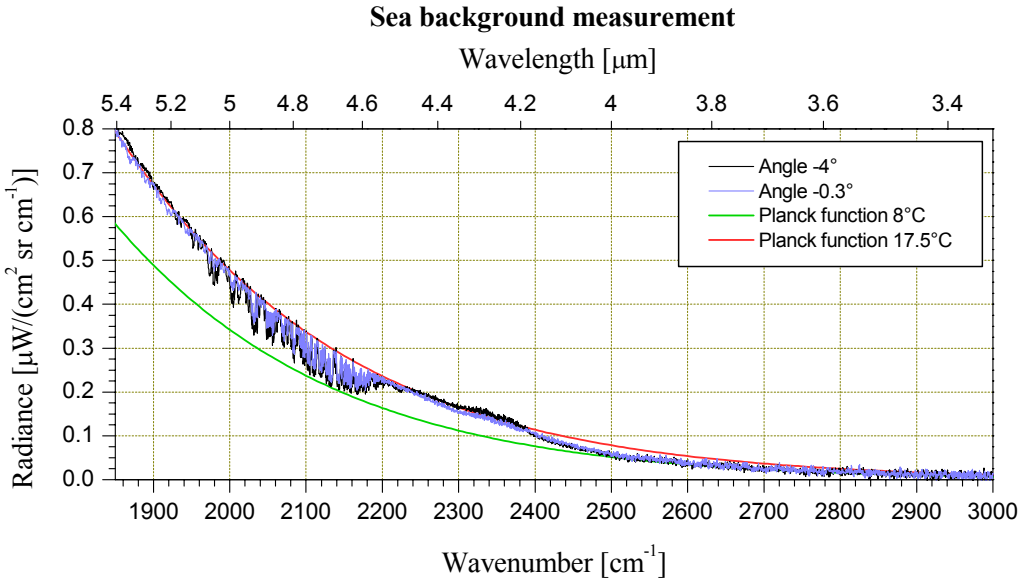

Figure 5.4 Radiance from the sea measured at different pitch angles with the InSb detector

The spectral characteristics of clear sky and sea backgrounds indicate that it is not possible to represent these parts of a naval scenario very well by blackbodies. If images recorded by IR cameras are converted to equivalent temperature, one cannot expect to get the same result if the cameras operate in different spectral bands. The same precautions apply to radiation contrasts between a ship and the background, when calculated from IR images from different cameras.

In overcast weather the sky radiance is dominated by radiance from the clouds, which is normally close to blackbody radiance corresponding to the air temperature at the cloud base. When the cloud base is low, this temperature is close to the air temperature near the surface. If, in addition, the difference between ground air temperature and sea temperature is small, the total radiance from the sea is also expected to be close to blackbody. Due to the fine weather during the whole SIMVEX trial we were unable to confirm this scenario with our measurements.

Figure 5.5 IR image from the Milcam camera showing the sky and the sea at 19 Sep 01, 22:34 (UTC). The red circle is located at pitch angle 1°

However, we had some days when most of the sky was clouded, but the cloud base was located at high altitude. In this case the temperature of the clouds is much lower than the ground air temperature. Due to atmospheric absorption and path radiance, the spectral sky radiance will contain much of the same line structure as observed from a clear sky. The line structure will then also appear in the reflected sky radiance contribution from the sea. Figure 5.7 shows measurements of the sea in runs 16 and 39, recorded with the CMT detector. In run 16 we had very few clouds, cloud cover < 1/8, while the sky was almost overcast in run 39, cloud cover > 7/8. The spectral influence of reflected sky radiation is clearly visible in both spectra, but we observe that the line structure is less dominating when the sky is mostly cloudy. Figure 5.8 shows similar spectra recorded on the same days by the InSb detector, runs

15 and 40. Sea background spectra for some more runs are shown in chapter 6 together with the ship surface measurements.

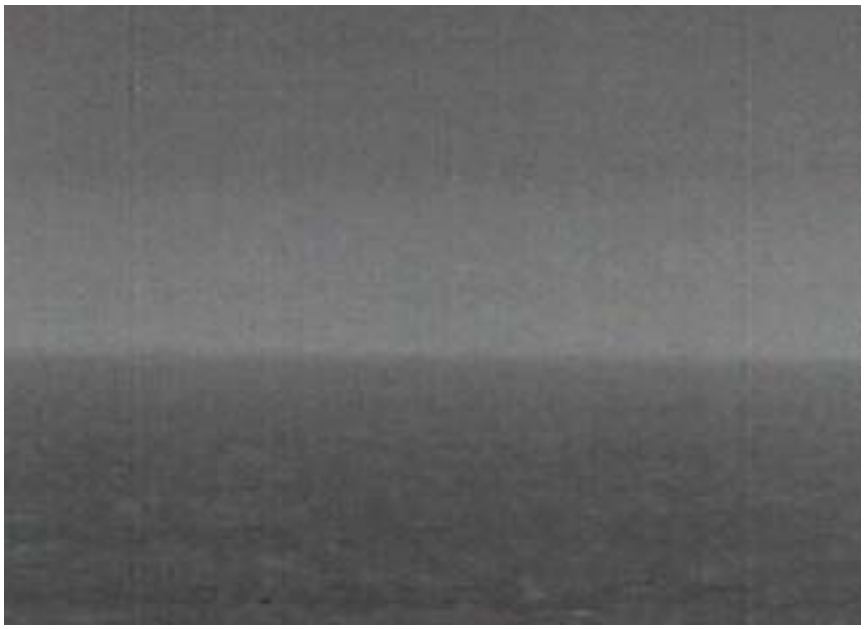

Figure 5.6 *IR image from the Sentinel camera showing the sky and the sea at 16 Sep 01, 18:00 (UTC). The field of view is approximately the same as Figure 5.5*

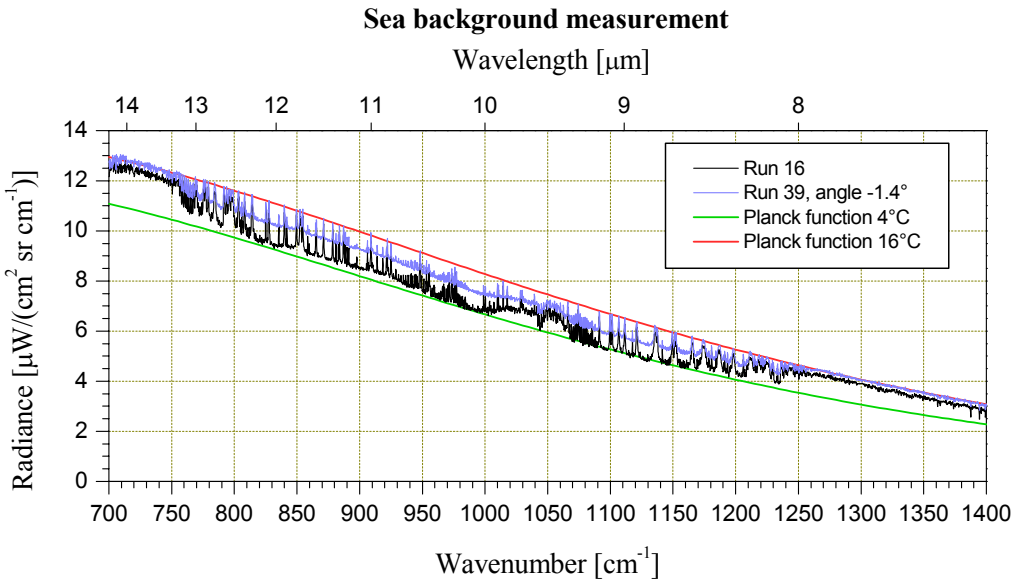

Figure 5.7 *Radiance from the sea measured at different cloud conditions with the CMT detector, SIMVEX runs 16 and 39*

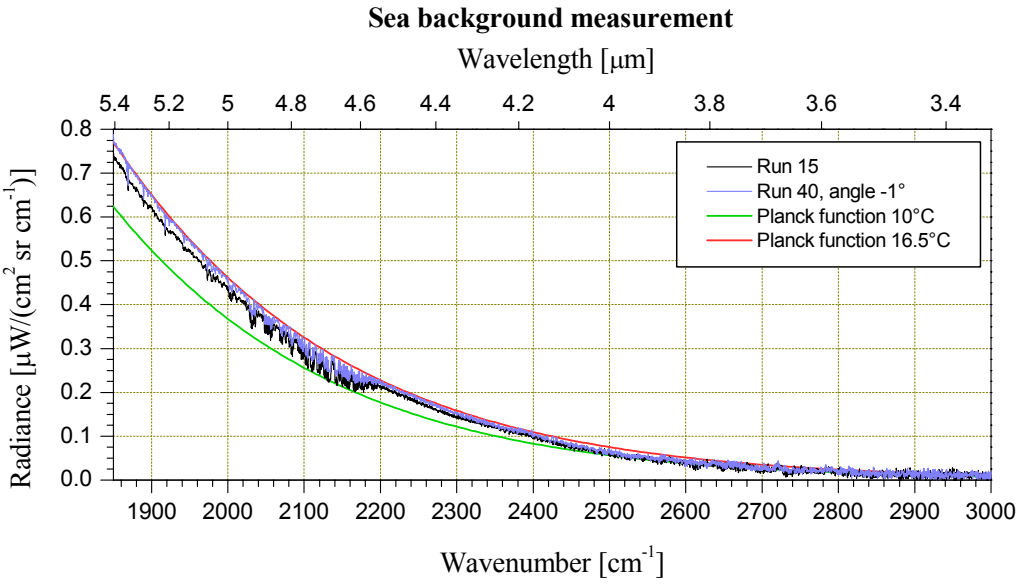

Figure 5.8 Radiance from the sea measured at different cloud conditions with the InSb detector, SIMVEX runs 15 and 40

5.3 Background measurements integrated over spectral bands

In addition to the results shown in Figure 5.1 to Figure 5.4, we also measured the sea and sky backgrounds at other angles. Altogether the sky was measured at angles of 0°, 1°, 5° and 15°. The sea was measured at angles of -4°, -2°, -1°, -0.5° and -0.3°. A measurement was also performed at an angle of -0.15° with the horizon line inside the field of view. In this case the field of view was partly filled with sky and partly filled with sea.

The sea measurements show small variations in spectral radiance when the angle is between -4° and -1°. Approaching the horizon the radiance increases. The sky measurements show that the radiance decreases when the angle increases. The tendency is clear for all parts of the measured spectral bands, maximum radiance occurs just above the horizon.

Some differences in spectral properties between the sea and the sky are noteworthy. Figure 5.9 shows two spectra of the sky and sea backgrounds, measured at pitch angles of 1° and -1°, respectively. The typical atmospheric line pattern appears in both spectra, but with different strength. While the sky clearly radiates more than the sea in the spectral band 800-900 cm^{-1}, the difference between the two spectra is much less in the spectral band 1100-1200 cm^{-1}. This result could be an indication of spectral variations of the reflection coefficient of the sea surface, but may also be influenced by the distribution of directions to the sky due to sea surface wave reflections, since sky radiance is varying more as a function of pitch angle in

spectral regions with high atmospheric transmittance than in spectral regions with low atmospheric transmittance.

To illustrate the sky and sea background radiances as function of pitch angle, we have integrated all measured spectra over specific spectral bands. The results for the 8-12 μm region are shown in Figure 5.10.

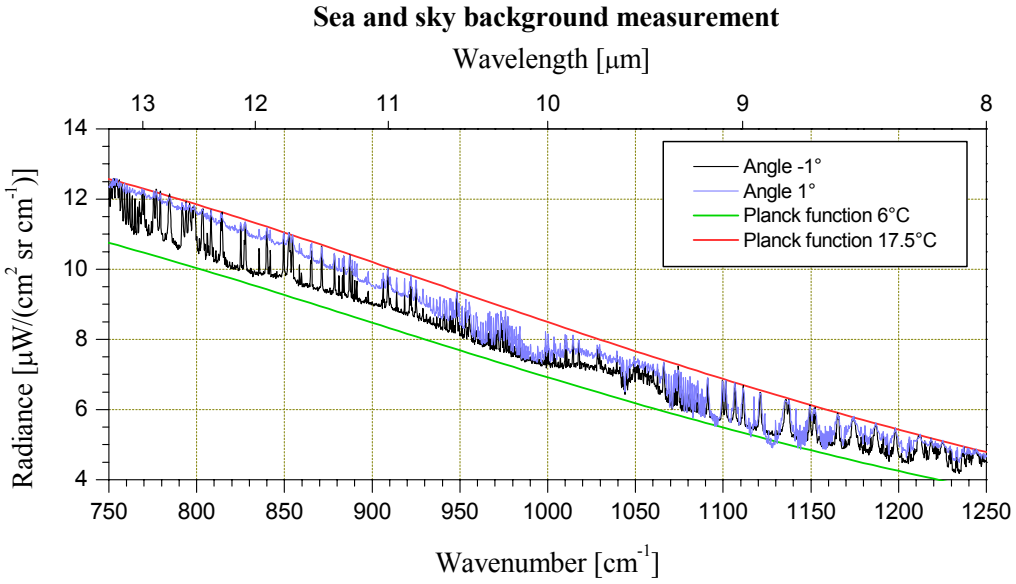

Figure 5.9 Comparison of sky and sea backgrounds measured with the CMT detector

Figure 5.11 shows the integrated radiance for the 3-5 μm band. In addition to the InSb measurements, the figure also includes integrated spectra from CMT measurements, which were made another day under different meteorological conditions. The signal to noise ratio is poor for each individual spectrum, but the integration seems to give reasonable results. However, the result is sensitive to noise and calibration errors, for instance the flat line from 0.5° to 1.0° is probably not correct. But the radiance difference between the two measurements, increasing with sky angle, shows the influence of variation in air temperature and absolute humidity.

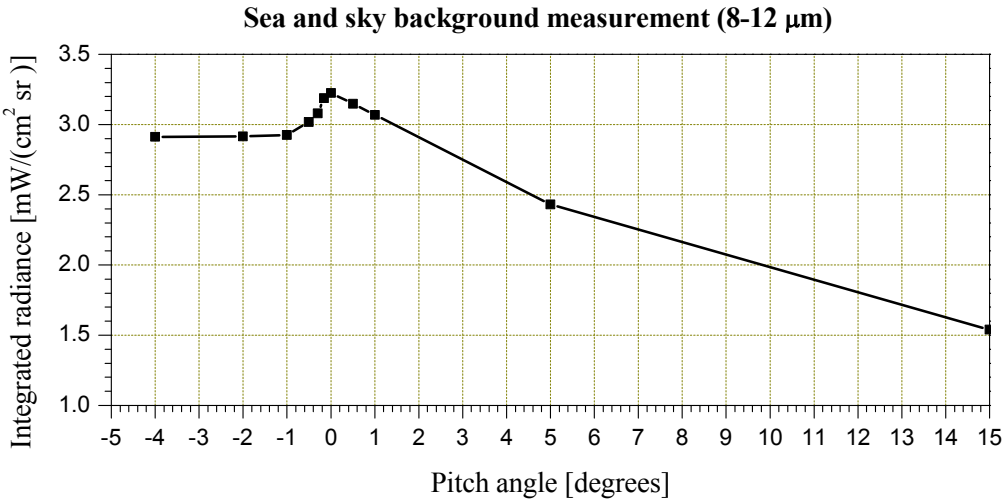

Figure 5.10 Radiance from sea and sky measured with the CMT detector integrated over the spectral band 833-1251 cm^{-1} (8-12 μm), 16 September 2001, 17:30 to 18:10 (UTC)

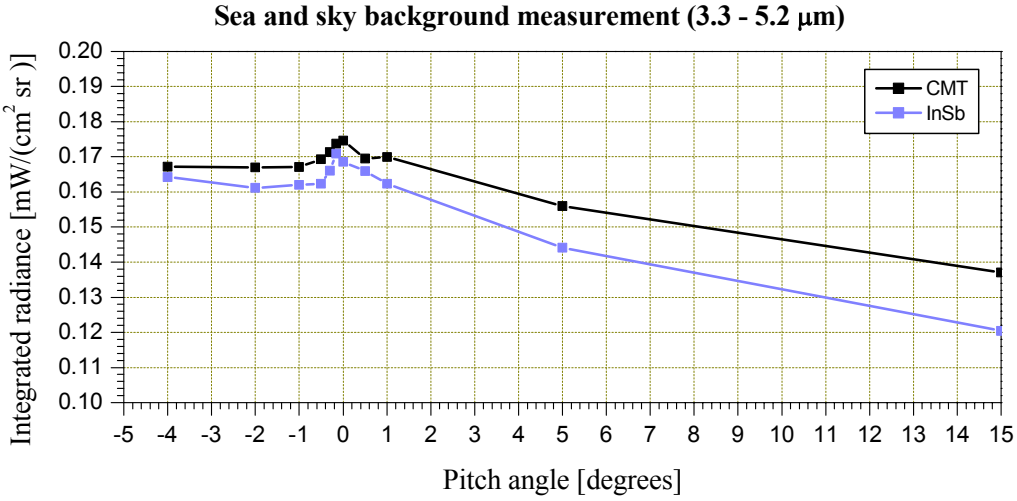

Figure 5.11 Integrated radiance over the spectral band 1910-3040 cm^{-1} (3.3-5.2 μm) for two measurements of sea and sky at different days using both the CMT and the InSb detectors. CMT measurement: 16 September 2001, 17:30 to 18:10 (UTC) InSb measurement: 19 September 2001, 22:00 to 22:45 (UTC)

5.4 Comparison with IR modelling tools

The spectral radiance from the sky may be modelled using IR modelling tools such as FASCODE and MODTRAN. To obtain a spectral resolution comparable with measured spectra, the FASCODE model is required. The FASCODE model includes 6 default models of meteorological parameters at different altitudes, varying from "Subarctic winter" to "Tropical". In addition, the model may be run with a user specified profile of meteorological parameters and molecular concentrations. To work properly in this mode, the meteorological conditions (pressure, temperature, absolute humidity) should be known at all altitudes up to 100 km. These parameters were only measured close to the earth's surface at the SIMVEX test site, but radiosonde data from balloon launches collected by Environment Canada were available for our analysis. These data were collected two times a day at Sable Island and Yarmouth (both more than 200 km from Osborne head), and once a day on the 17th and 18th September from Shearwater Airport, just a few kilometers from Osborne Head. Shearwater data are not available for the times when we measured sea and sky backgrounds, and the other data sets are collected far from the shore station. Thus we cannot expect the radiosonde data to precisely represent the meteorological conditions during the runs. However, we have run FASCODE simulations with user defined profiles based upon the data we have. The details of the meteorological parameters in our user defined profiles are presented in appendix A.

Figure 5.12 shows the spectral radiance from the sky at an angle of 15° calculated with a user defined profile (see Table A.8) compared with the standard models "US Standard", "Subarctic Summer" and "Midlatitude Summer".

We see that the selection of model has a significant impact on the spectral radiance. Although the "Subarctic Summer" and "US Standard" models are fairly close in ground temperature, the radiances deviate a lot in spectral regions with good atmospheric transmittance, due to differences in absolute humidity. Figure 5.13 shows the measured FTIR spectrum of the sky at the same angle compared with the FASCODE calculation using the user defined profile. The modelled spectrum fits the measured result quite well, remembering the uncertainty of the radiosonde data validity, but the modelled spectrum is slightly below the measured spectrum. Figure 5.14 compares the same results at an angle of 1°. We see that the fit is not so good here, and the modelled spectrum is above the measured spectrum. The reason for the deviation is probably that the calculation is more sensitive to precise meteorological data along the line of sight, due to the long atmospheric path at this angle.

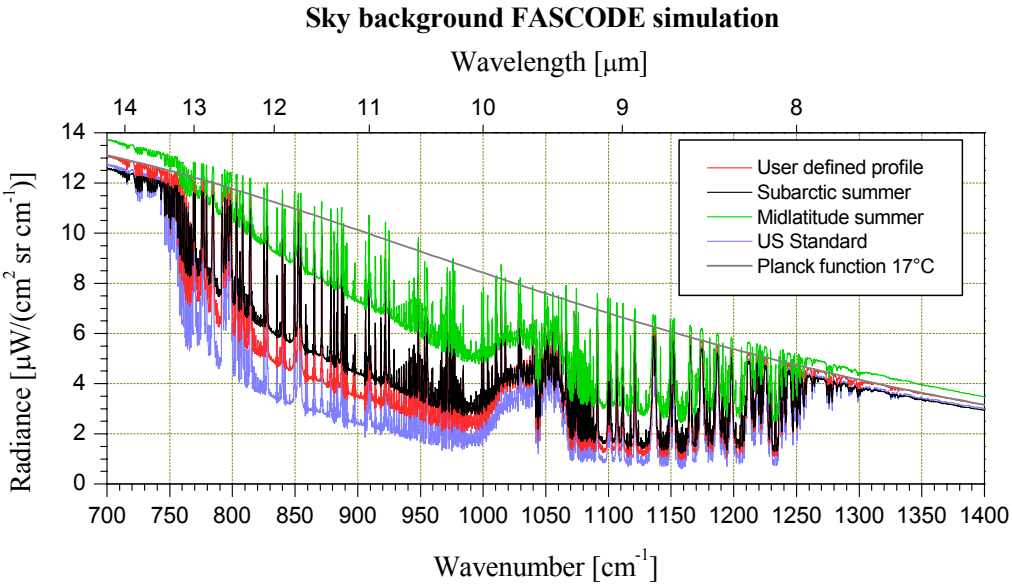

Figure 5.12 Radiance from the sky at pitch angle 15° simulated with FASCODE 3 using different atmospheric models.

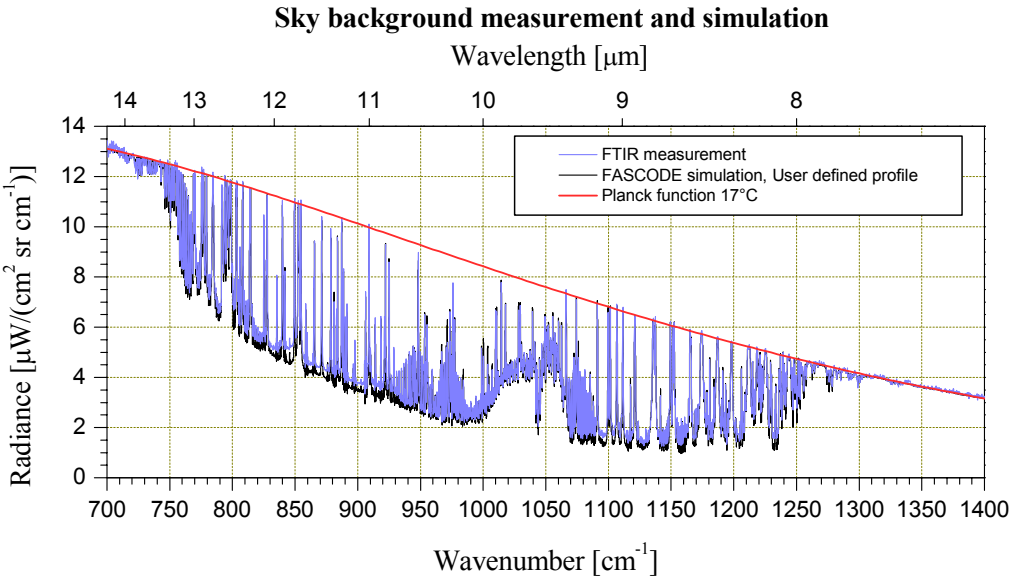

Figure 5.13 Comparison of measured and simulated sky radiance at pitch angle 15°

When running ShipIR, the meteorological parameters are normally only specified at sea level, and the parameters at other altitudes are automatically scaled using the profiles of the standard

models, but an option exists to input a user defined profile. We have run the ShipIR model to predict the sea and sky background for this scenario. Figure 5.15 shows the spectral radiance from the MODTRAN calculation performed by ShipIR at angle 15° using a scaled "Midlatitude Summer" model, compared with a MODTRAN calculation using the same user defined atmospheric profile as the FASCODE calculation above.

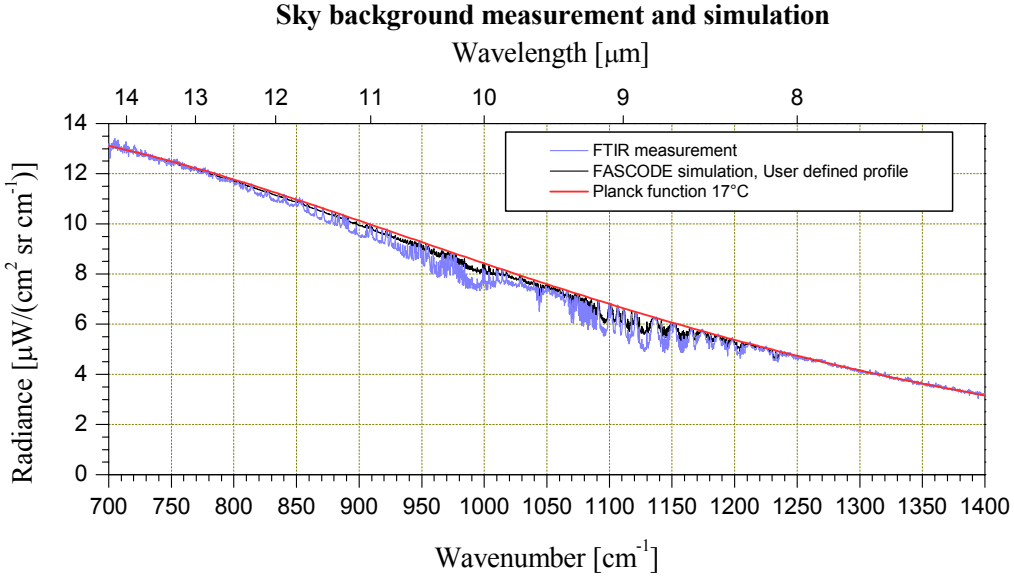

Figure 5.14 Comparison of measured and simulated sky radiance at pitch angle 1°

Figure 5.15 shows that the MODTRAN result is very close to the FASCODE result (see Figure 5.13) when the same atmospheric profile is used. The figure also shows that the spectral radiance changes significantly when using a scaled default model, as in Figure 5.12, resulting in an overprediction of sky background radiance compared to the user defined profile and the measured radiance.

Figure 5.16 shows the sea and sky background integrated radiance predicted by ShipIR as a function of pitch angle, integrated over the 8-12 μm band, using the scaled "Midlatitude Summer" model and the user defined profile for both available sea models, Mermelstein and Cox-Munk. The pitch angle range -5° to 15° is covered. Changing the sea model does not affect the sky radiance, but the radiance from the sea changes slightly. However, the effect is small compared to changing the atmospheric profile, which has a significant influence on the radiance both from the sea and the sky.

Figure 5.17 shows integrated sky and sea radiance, comparing radiances measured by the FTIR instrument and modelled by ShipIR using the Mermelstein sea model. For angles above the horizon, the radiance modelled with FASCODE is also included. Similar to the individual

spectra presented in Figure 5.13 and Figure 5.14, the integrated spectra show that FASCODE underpredicts the radiance at high angles a little when using our user defined profile, while there is a small overprediction at low angles.

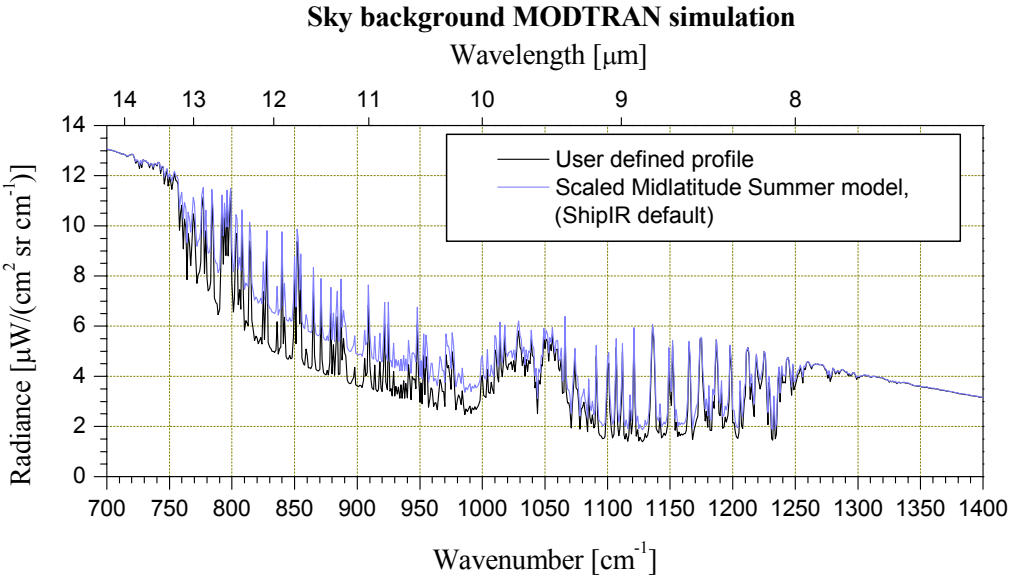

Figure 5.15 Sky radiance simulations using MODTRAN. Comparison of user defined profile and an automatically scaled Midlatitude Summer model similar to ShipIR simulation

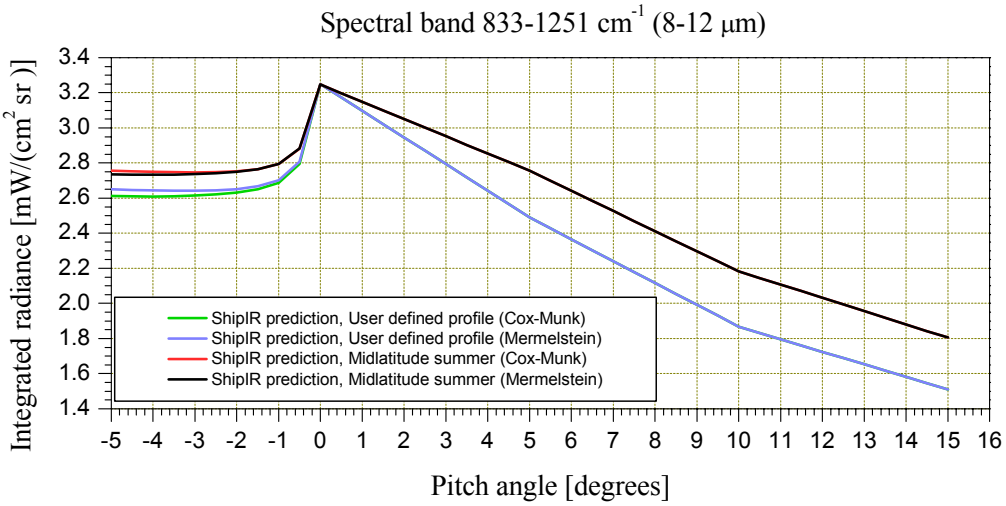

Figure 5.16 ShipIR prediction of sea and sky background, comparing different atmospheric profiles and sea models

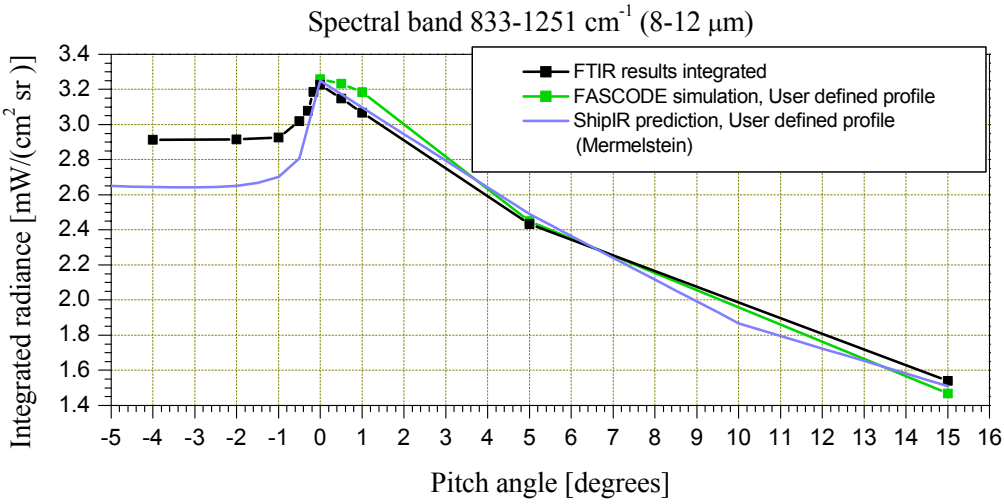

Figure 5.17 Comparison of integrated sea and sky radiance as a function of pitch angle

The figure also shows that ShipIR and FASCODE predict the same radiance as the measured radiance just above the horizon. At higher angles the ShipIR prediction is close to the measured radiance and the FASCODE calculation. If the pitch angle resolution had been similar for the FASCODE and ShipIR calculations, the results of these calculations would have been very close. The sea background radiance from ShipIR is underpredicted compared to measured radiance, but the shape of the curves as a function of pitch angle agrees quite well. The reason for the deviation in absolute values could be that the actual emission coefficient of the sea surface is higher than modelled in ShipIR, or the distribution of reflected directions to the sky from the sea surface could be different.

Considering the 3-5 μm band, a comparison between measured and modelled radiance is more challenging. First, the variation in air temperature was greater during the time period the sea and the sky was measured. Second, the absolute humidity at the shore station was lower than any of the radiosonde data. Third, the signal to noise ratio is low in the high wavenumber part of the 3-5 μm band. We have still performed some calculations to model the InSb measurements. The blue and the green curve in Figure 5.18 shows the spectral radiances from the FTIR measurement and a FASCODE calculation for a small part of the 3-5 μm band, using the same user defined profile as for the CMT measurements. The agreement between the two curves is not very good, which is not surprising, due to the differences in temperature and humidity.

The black curve shows the radiance calculated by a modified user defined profile. The meteorological parameters at sea level are set to the shore station data during the InSb measurement, and the parameters up to 1.5 km are scaled correspondingly (see Table A.9. Although the modified user defined profile is quite uncertain, a reasonable agreement is now

achieved. The results in Figure 5.18 confirm the results from Figure 5.12, in that the spectral sky radiance is very sensitive to meteorological parameters.

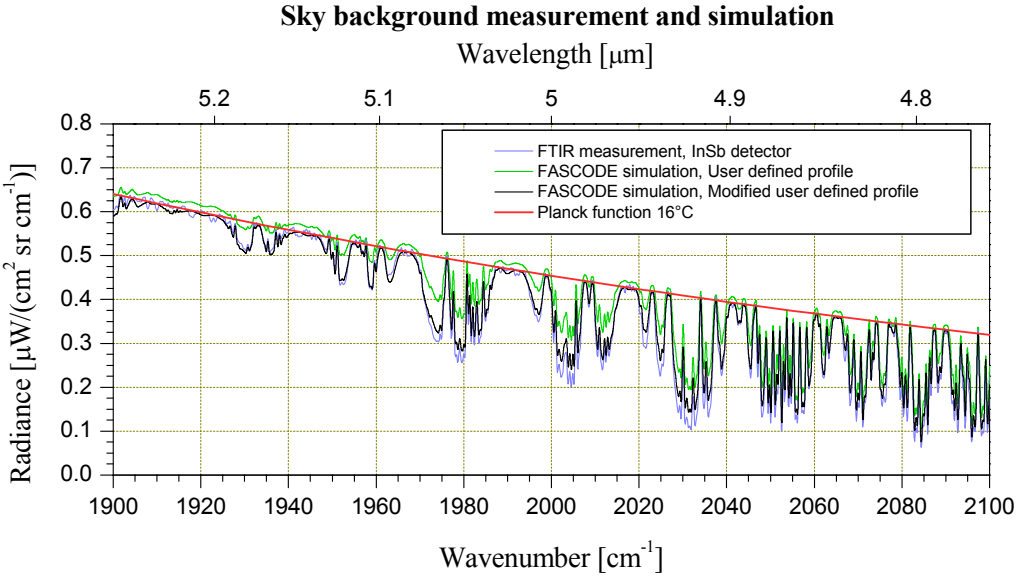

Figure 5.18 Comparison of measured and simulated sky radiance at pitch angle 15°

Integrated sky and sea radiance, measured by the FTIR instrument and modelled by ShipIR and FASCODE are shown in Figure 5.19. The modelled sky radiances fit the measured spectra quite well, but the deviations are greater than for the 8-12 μm band, resulting in an overprediction of the modelled sky radiance at high pitch angles. The reason is probably higher uncertainty regarding the atmospheric profile. For the sea radiance, the results are quite similar to the 8-12 μm band results, showing an underprediction of the modelled sea radiance. This result does not agree with the results from the analysis of NRL images, which concluded that ShipIR overpredicts the sea radiance in the 3-5 μm band (20).

The results presented in this section have shown that the spectral radiance from the sky is sensitive to variations in meteorological conditions. Except for angles close to the horizon, the meteorological conditions several kilometers above sea level influence upon the sky radiance. If the parameters are known and used as input to ShipIR, it should be possible to model sky radiance with high precision. If the parameters are unknown, and the ShipIR automatic scaling is applied, a reduced precision should be expected. We have also shown a disagreement in absolute values between predicted and measured sea radiance. This subject should be investigated further in order to improve the ShipIR model. Measurements of the sea surface radiance at different sea states and meteorological conditions are then probably required.

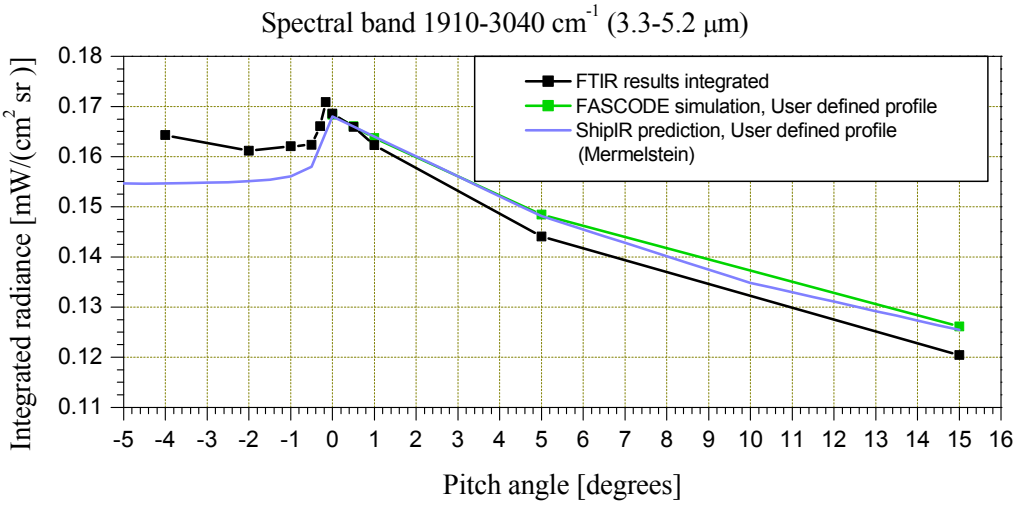

Figure 5.19 Comparison of integrated sea and sky radiance as function of pitch angle

5.5 Atmospheric transmittance and path radiance

Before presenting the results from ship surface measurements in the next chapter, atmospheric transmittance and path radiance affecting these measurements will be discussed in this chapter. Equation (2.23) states that the measured radiance is affected by atmospheric transmittance and path radiance. Figure 5.20 shows a calculation of the atmospheric transmittance between the ship and the shore station (range 1 km) for run 19, which should represent a typical meteorological situation during the SIMVEX trial. The transmittance is calculated with FASCODE 3, with a resolution corresponding to the FTIR measurements (0.5 cm^{-1}, Bomem definition) of the ship surface. The figure shows that the average atmospheric transmittance is high in the 3-5 μm and 8-12 μm bands. However, there are rapid spectral variations in transmittance inside these spectral bands, due to strong absorption lines.

The path radiance from the atmosphere for a horizontal path of 1 km is shown in Figure 5.21 and Figure 5.22. These figures show similar spectral variations, with the same lines appearing as emission lines. According to equation (2.29) the atmospheric lines appear as absorption lines if the measured source radiates as a blackbody, and the source temperature is higher than the atmosphere. However, if the source temperature is lower than the atmosphere, the lines appear in the spectrum as emission lines. If the temperatures of the source and the atmosphere are equal, the effects of absorption and emission cancel each other, and the apparent radiance should be equal to a blackbody. Thus we may conclude that independent of the absolute precision of calibrated spectra, the apparent radiance from external sources will show whether the equivalent temperature of the source is above, below or close to the atmospheric temperature.

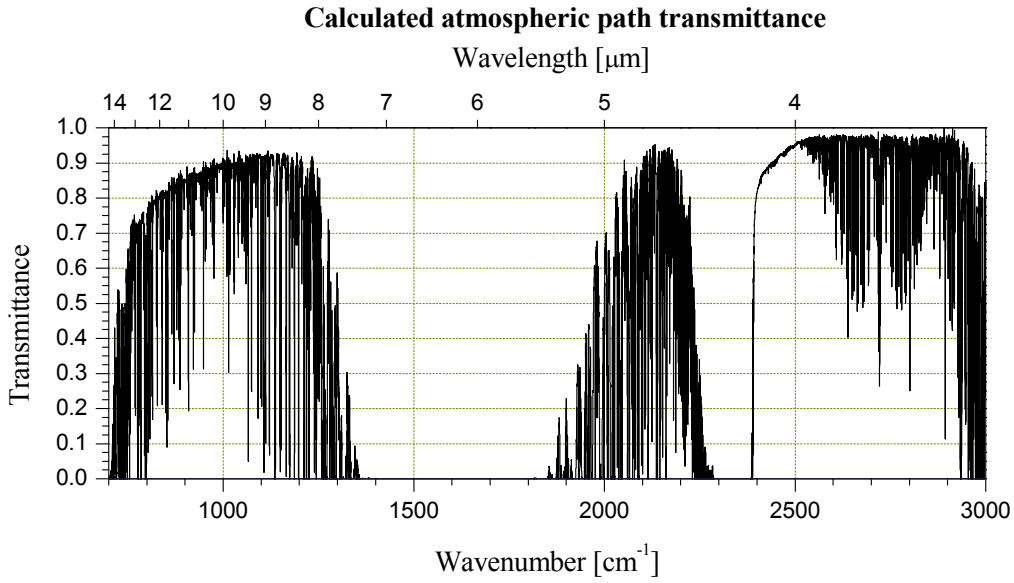

Figure 5.20 Calculated atmospheric transmittance (FASCODE) at distance of 1 km for a typical meteorological situation, SIMVEX run 19

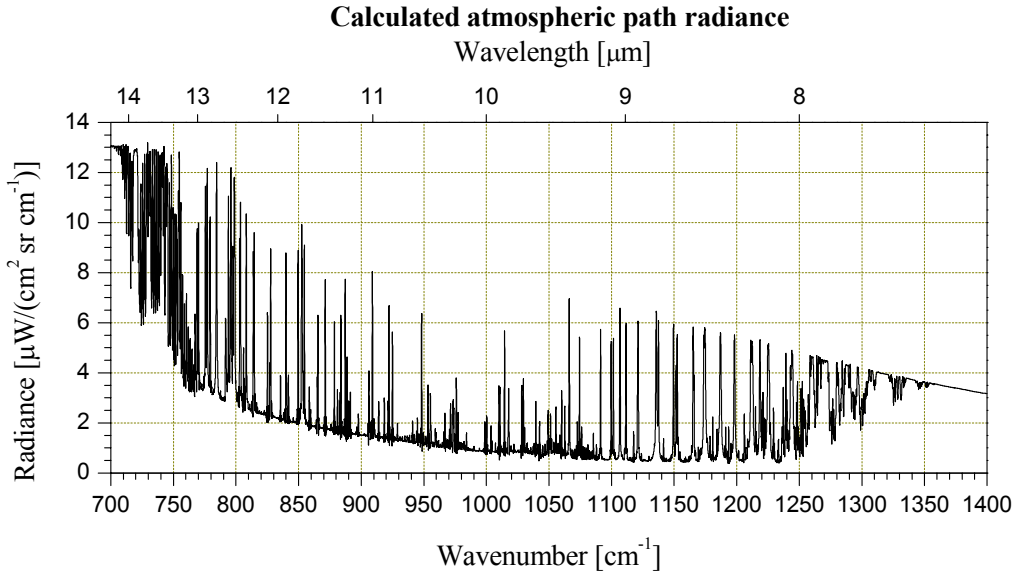

Figure 5.21 Calculated radiance (FASCODE) from a 1 km horizontal atmospheric path in the 8-12 μm band for a typical meteorological situation, SIMVEX run 19

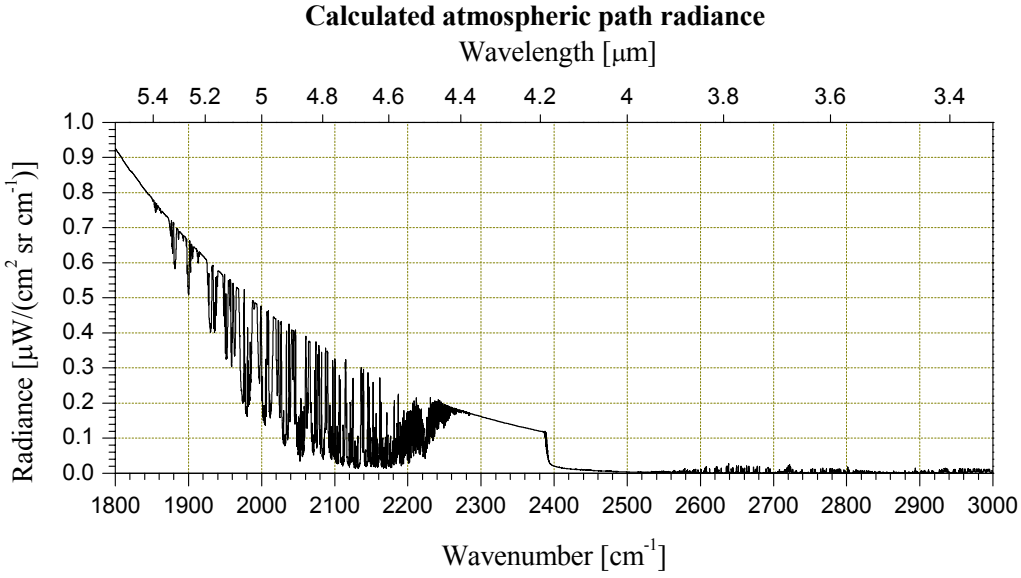

Figure 5.22 Calculated radiance (FASCODE) from a 1 km horizontal atmospheric path in the 3-5 μm band for a typical meteorological situation, SIMVEX run 19

6 SHIP SURFACE MEASUREMENTS

In this chapter we present results obtained from measurements of the ship surface. We start our study by presenting the results from the night runs, comprising measurements of the port side hull, the funnel and the front of the ship. From day runs we present spectra of both shaded and sun illuminated parts of the ship. The measurements of shaded parts include the starboard side of the hull in A runs and the front of the ship in C runs. We also present results from the port side of the hull and the funnel when the ship was illuminated by the sun, including a scenario with specular reflection from the ship hull. To illustrate the positions of the FTIR field of view on the ship during spectral measurements, we also show examples of Milcam IR images with a red circle indicating the FTIR field of view. However, we do not include IR images for all spectra shown.

A CAD drawing of CFAV Quest was supplied by NRL, and a complete target input file for running the ShipIR model was prepared by Davis before the trial. Many of the SIMVEX runs have been processed by running ShipIR at FFI. Results from these simulations are presented in (3). Temperature predictions from ShipIR simulations as well as temperatures measured with thermocouples on board the ship are presented in this chapter and compared with FTIR ship surface measurements.

A summary of the runs and meteorological parameters is presented in appendix A.

6.1 Night runs

6.1.1 Port side measurements

During the D type night runs the port side of the ship was measured with the FTIR spectroradiometer. Figure 6.1 shows an IR image from the Milcam camera during a measurement of the bridge.

Figure 6.2 shows the results from measurements of the bridge in runs 16 and 26, both measured with the CMT detector. A more detailed view is presented in Figure 6.3. The spectra indicate that the signature of the ship surface is very close to a blackbody spectrum at a temperature close to the atmospheric temperature.

Although the radiance from the ship surface is very close to a blackbody, the atmospheric lines are barely visible, but appear as weak emission lines. According to the discussion in section 5.5, this indicates apparent surface temperatures just below air temperature. However, we will discuss this result in more detail, since the result may be affected by reflections of the sky from the surface that may also cause a similar line structure in the spectrum. At FFI we measured the total and specular reflection from test samples painted with the same white and yellow paints as used on CFAV Quest. The results of these measurements, carried out before the trial, are presented in (3).

Figure 6.1 Milcam IR image of the port side of the bridge from a night run, SIMVEX run 26

Since the surface paints are reflecting, radiation from the sea and sky foreground reflected from the ship surface should contribute to the total signature of the ship. Due to a complicated mixture of diffuse and specular reflection of sea and sky, and even some land foreground, a prediction of this effect is difficult. Although the reflection coefficient is not very high, one

would expect to get a spectrum showing the same line structures as the sea background spectra presented in chapter 5. Generally these lines are the same as the lines generated by path emission, which can be seen by comparing for instance Figure 5.1 and Figure 5.21. Thus it could be difficult to distinguish surface reflection from path emission. However, there is one exception. In the region 1000-1100 cm^{-1}, the sky radiance presented in Figure 5.1 shows a spectral feature caused by emission from the ozone molecule. This molecule is mostly concentrated at high altitudes of the atmosphere (25 km). Since its concentration is much lower close to the earth surface, its contribution to path radiance is very low as shown in Figure 5.21.

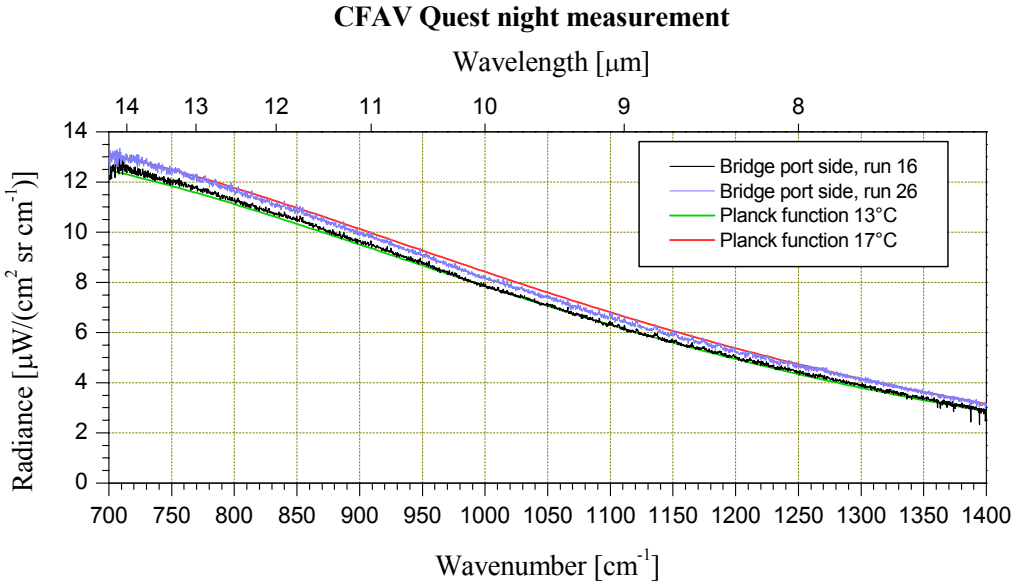

Figure 6.2 Two port side measurements of bridge at night time with the CMT detector, SIMVEX runs 16 and 26

When we study Figure 6.3, we can hardly observe the ozone structure at all. This indicates that the contribution from sky and sea reflected in the ship surface is very low, and generally below the signal to noise ratio of the spectral measurements. Therefore we conclude that the weak emission lines observed in this scenario, mainly originate from atmospheric path radiance.

Figure 6.4 shows two spectra from the bridge measured during runs 15 and 27 with the InSb detector. Also in the 3-5 μm band the apparent radiance of the ship surface is close to a blackbody. Again, the atmospheric lines (most visible in run 15) are weak, but appear mostly as emission lines, indicating apparent surface temperatures below air temperature. In the low wavenumber region, a few lines appear as absorption lines. The reason is probably variation in temperature close to the instrument, since these lines have very high line strength, according to FASCODE calculations as those presented in section 5.5.

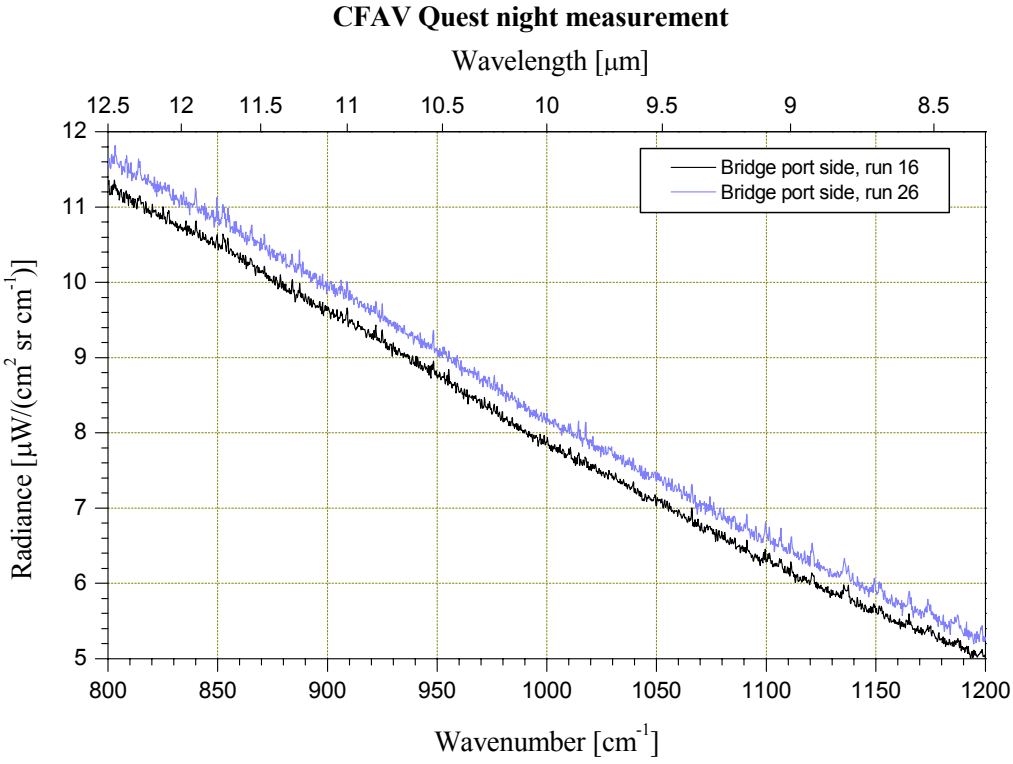

Figure 6.3 Detailed view of the bridge night time measurement above

According to the results from the paint reflection measurements, a higher reflection from the ship surface is expected in the 3-5 μm spectral region. Since the ozone molecule does not have any significant contribution in this region, we are unable to use the same evaluation as for the 8-12 μm band. The total contribution from path radiance may also be more complicated to interpret, since both water vapor lines below 2000 cm^{-1} as well as CO_2 lines in the region 2300-2400 cm^{-1} are strong, such that results are affected by air temperature variations close to the instrument.

The atmospheric transmission is very good, and thus the sky radiation is very low in the 2500-2700 cm^{-1} spectral region, as shown in Figure 5.2. If the influence on the ship signature due to reflection of the sky was significant, the spectral characteristics of the sky radiance should be visible in this part of the spectrum. Although the signal to noise ratio is getting rather poor in this region, it is not possible to observe any significant deviation from blackbody curve in the measured ship surface spectra. We therefore conclude that the influence of reflected radiation is very small, also in the 3-5 μm band, in this scenario. In section 6.2.3 we will show that the reflection definitely exists, during our analysis of day runs with sun reflection. In section 6.2.4 we will show that the reflection is also possibly observable at night time, when calculating apparent temperature by averaging data over a specific spectral band.

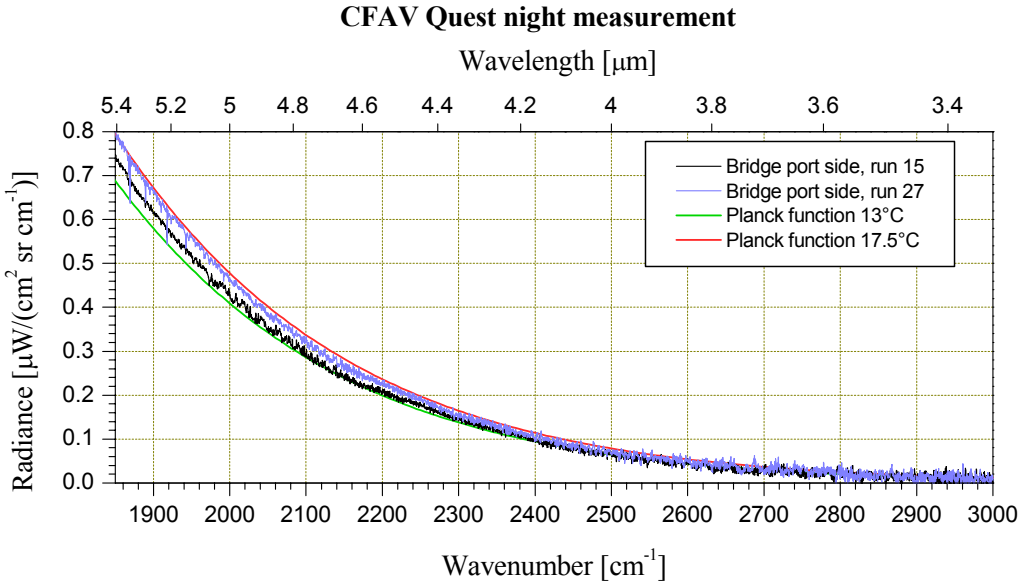

Figure 6.4 Two port side measurements of bridge at night time with the InSb detector, SIMVEX runs 15 and 27

Since the spectra from the side of the bridge during night runs seem to be close to a blackbody, it should be possible to model the ship signature with good precision over a wide infrared band using a blackbody with appropriate temperature. It should also be possible to make a realistic comparison of the results of equivalent temperature calculations from the different IR cameras that were in use during the SIMVEX trial.

6.1.2 Temperature comparisons

Except for variations in apparent temperature, the different night run spectra do not show much variation. For all runs we also measured the ship hull, typically in a position as indicated in Figure 6.5. The results from these measurements are generally very close to the bridge measurements. Therefore we will not show all these spectra. Instead we present the calculated apparent bridge and hull temperatures for each run.

The calculated apparent temperatures are presented in Table 6.1. The table also presents surface temperatures measured by thermocouple on board the ship, and temperature predictions using the ShipIR model.

Figure 6.5 Milcam IR image from a night run, measuring the port side of the hull, SIMVEX run 26

Run	Date	Start run (UTC)	Detec-tor	FTIR apparent temperature [°C]		Thermocouple measurement [°C]		ShipIR surface temperature prediction [°C]	
				Bridge	Hull	Bridge (T01)	Wall deckhouse (T21)	Bridge (sup1_ p_p4)	Hull (sup2_ p_p2)
7	13	23:24	CMT	14.4	14.7	16.4	16.4		
11	14	23:26	CMT	15.3	15.6	16.3	15.9	12.3	12.2
12	15	00:14	InSb	14.2	14.7	15.8	15.5	11.9	11.9
15	15	23:24	InSb	13.3	14.0	14.7	14.1	10.5	10.5
16	16	00:12	CMT	13.7	13.9	14.5	14.0	11.2	11.2
20	16	23:23	CMT	15.1	15.5	15.8	15.3	13.3	13.3
21	17	00:10	InSb	15.0	15.5	15.4	15.3	12.7	12.7
26	17	23:22	CMT	15.8	16.3	16.7	16.0	13.0	13.0
27	18	00:14	InSb	15.6	16.0	16.4	16.1	13.2	13.2
34	19	23:27	InSb	14.7	14.9	16.0	15.7	11.4	11.4
35	20	00:20	CMT	13.5	13.9	15.2	15.0		
39	20	23:26	CMT	15.1	15.6	15.9	15.3		
40	21	00:22	InSb	14.8	14.7	15.5	15.1		

Table 6.1 Side of bridge and hull surface temperature comparisons at night

The ShipIR model predictions are thoroughly described in (3). The ShipIR temperature predictions in the table refer to plates sup2_p_p4 and sup1_p_p2 for the brigde and hull, respectively. The temperature sensor on board the ship located closest to the FTIR hull measurement area is the I-button 102. But from our analysis of the data, we suspect that the temperatures measured by this sensor are not very reliable. We think that thermocouple T21, which was located on the deckhouse wall, may represent the hull temperature better, so we have used those data instead. For the bridge measurement, thermocouple T01 is used. The definition of equivalent temperature assumes that the source has emissivity equal to 1. Thus apparent and equivalent temperatures are not directly comparable with the temperatures predicted by ShipIR. The ShipIR predictions shown in this table were made using the air temperatures measured at the shore station. During the night runs this temperature was

normally lower than the air temperatures measured by the ship. In some ShipIR simulations presented in (3) we have used the air temperature measured by the ship. Those results show that the predicted surface temperatures then increase, but still ShipIR underpredicts the temperatures.

The bridge results in Table 6.1 are presented as graphs in Figure 6.6, including the air temperature measured at the shore station.

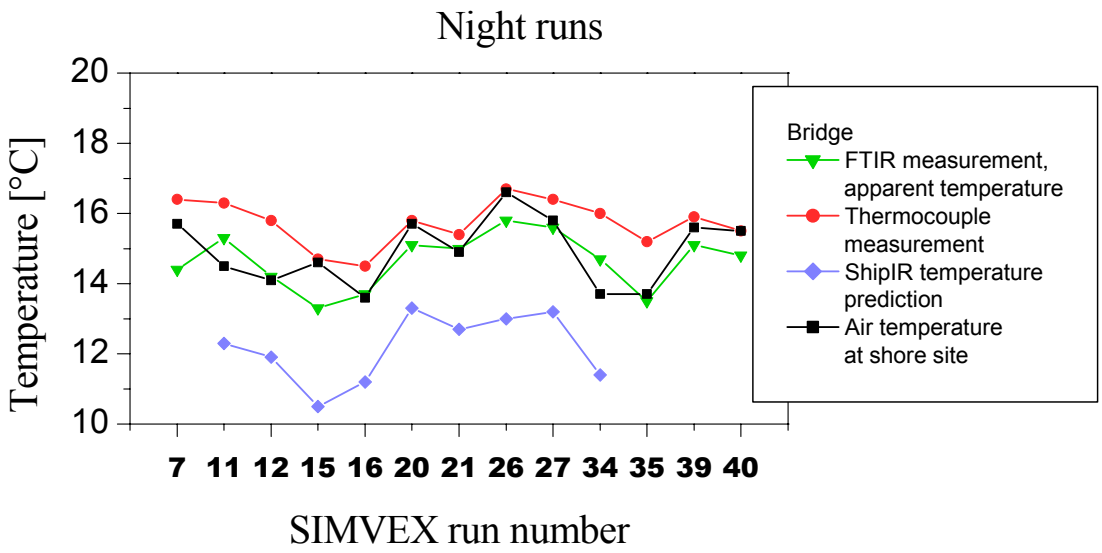

Figure 6.6 Comparison of measured and predicted bridge side surface temperatures at night

Note that the results from both detectors are merged together in these presentations. Bearing in mind that there is some uncertainty in the precision of the absolute values from the FTIR measurements (section 2.5), we observe a high correlation between the FTIR results and measured temperatures. For most runs the FTIR apparent temperature is a bit lower than the air temperature measured at the shore, indicating that the ship surface cools down by radiation towards the clear sky. However, the measured effect is much lower than what ShipIR predicts. This conclusion is in accordance with a similar conclusion in (3).

6.1.3 Front and starboard side measurements

We also measured the front of the bridge during the D runs. Figure 6.7 shows an IR image of the ship during a measurement of the front (due to low contrast it is difficult to distinguish between the bridge front and side in this image). Again the spectral characteristics are very similar to the side of bridge results. Results from these measurements, similar to those in the previous section, are presented in Table 6.2 and Figure 6.8, using data for I-button I34 and

ShipIR prediction for plate supm_f2_p1. The results show small temperature differences between the front of the bridge and the ship hull. Also regarding the front of the bridge, ShipIR generally predicts lower temperatures than those measured with the I-button and calculated from the FTIR measurements.

Figure 6.7 Milcam IR image from a night run, measuring the front of the bridge, SIMVEX run 26

Run	Date	Start run (UTC)	Detec-tor	FTIR apparent temperature [°C]	I-button measurement [°C] (I 34)	ShipIR surface temperature prediction [°C] (supm_f2_p1)
15	15	23:24	InSb	13.6	14.5	10.6
16	16	00:12	CMT	13.8	14.5	11.3
20	16	23:23	CMT	15.4	15.5	13.8
21	17	00:10	InSb	15.0	15.5	13.1
26	17	23:22	CMT	16.0	16.5	13.1
27	18	00:14	InSb	15.6	16.0	13.4
34	19	23:27	InSb	15.0	14.0	12.1
35	20	00:20	CMT	13.9	14.0	
39	20	23:26	CMT	15.7	15.5	
40	21	00:22	InSb	14.5	15.5	

Table 6.2 Front of bridge surface temperature comparisons at night

The starboard side of the ship hull was measured after the ship had turned during the night runs. The results are similar to the port side results. The spectral variations are very small, and generally the apparent temperature variations are smaller than the estimated precision of the results. The IR camera results presented in (3), showed variations in IR signature caused by wind. These variations are too small to be confirmed by FTIR results.

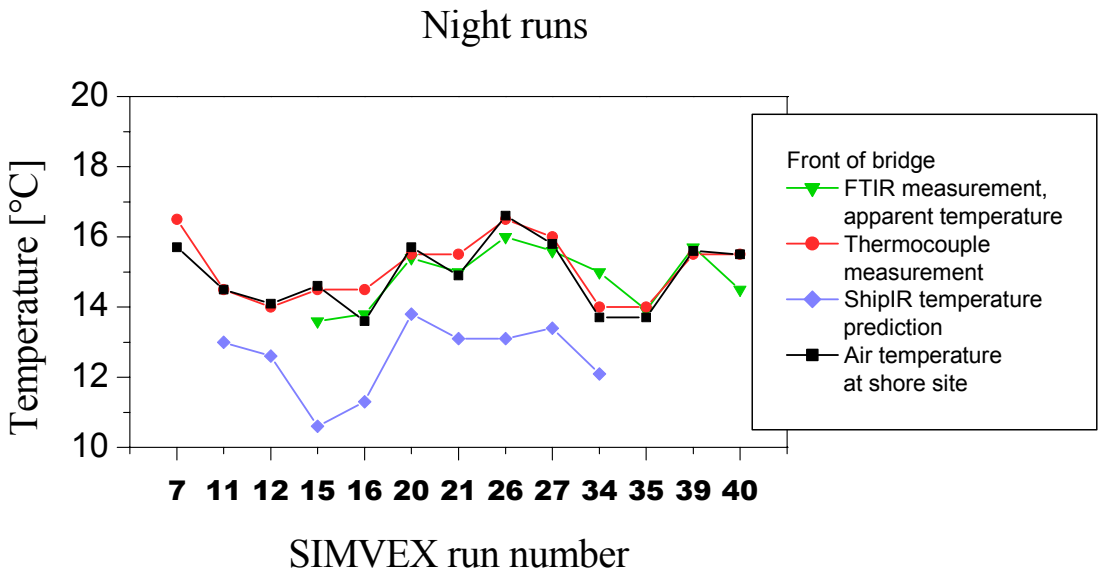

Figure 6.8 Comparison of measured and predicted bridge front surface temperatures at night

6.1.4 Funnel measurements

Figure 6.9 shows an IR image from a funnel measurement. Figure 6.10 and Figure 6.11 show spectral results from measurements of the funnel during runs 26 and 27 measured with the CMT and InSb detectors, respectively. These FTIR results do probably not have the same precision as the results for the ship hull. The reasons for this are large temperature gradients in the funnel area, and possible field of view variations due to our manual tracking of the instrument. We attempted to aim at the coolest part of the funnel, away from the hot stack outlet.

We can observe some important features from the funnel spectra.

- The spectral signature of the funnel, which is painted with a different paint than the rest of the ship (yellow), is close to a blackbody signature over the entire infrared region.

- Atmospheric lines are almost invisible in the funnel spectra, indicating apparent temperatures close to air temperature. The temperature of the funnel is not much higher than the ship hull during night runs.

- In the 8-12 μm region the contribution from reflected sky radiance is very small, since we do observe line structures originating from ozone sky radiation. In the 3-5 μm region the spectral distribution is almost unchanged compared to the hull measurement.

Figure 6.9 *Milcam IR image from a night run, measuring the port side of the funnel, SIMVEX run 26*

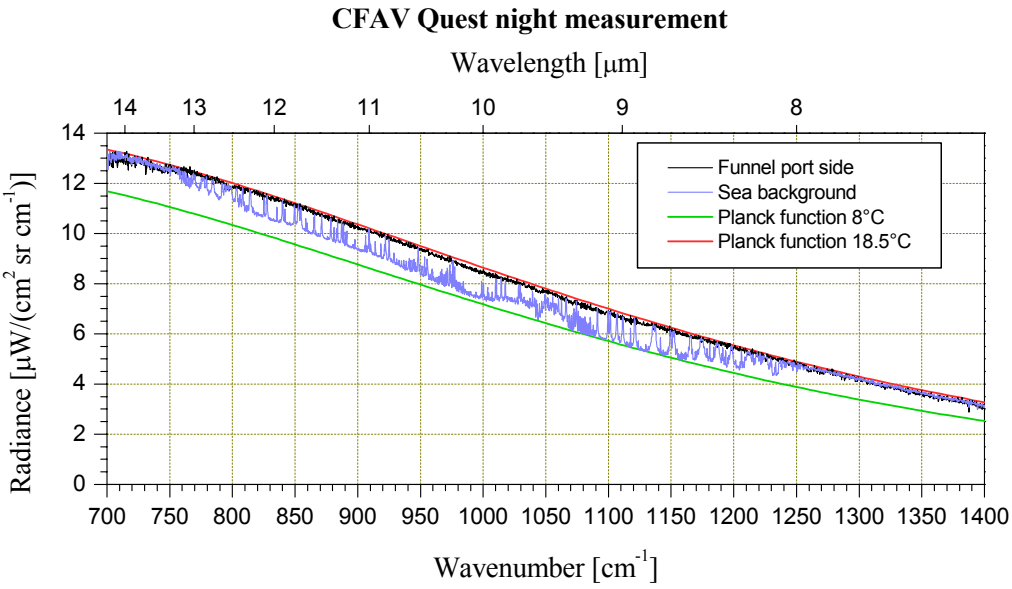

Figure 6.10 *Port side measurement of the funnel and the sea background at night time with the CMT detector, SIMVEX run 26*

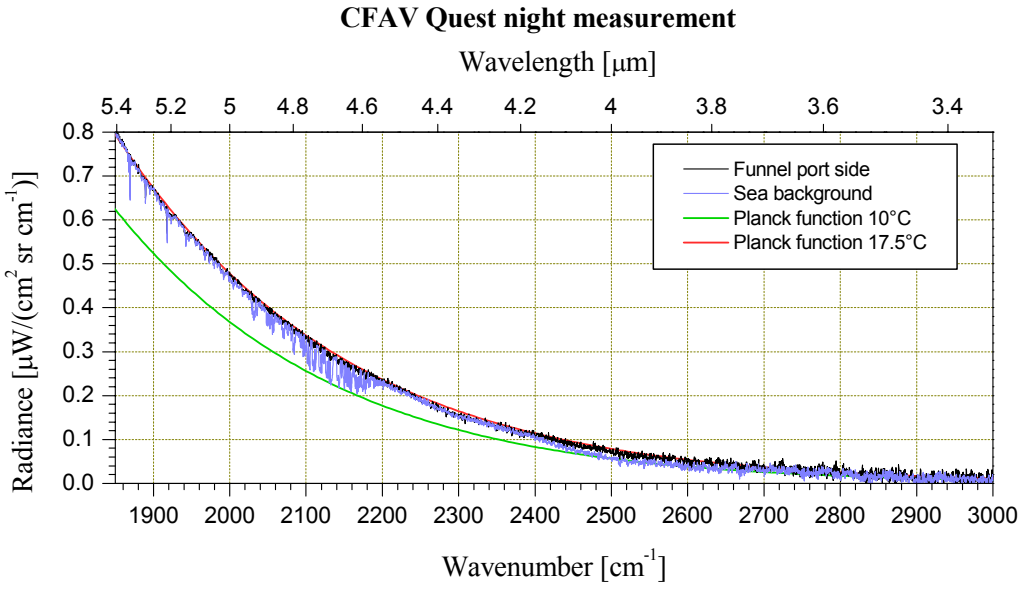

Figure 6.11 Port side measurement of the funnel and the sea background at night time with the InSb detector, SIMVEX run 27

6.2 Day runs

6.2.1 Shaded ship measurements

As mentioned in section 4.1 we decided to measure both shaded and sun illuminated parts of the ship during the same run with the FTIR instrument, to improve the reliability of comparison of results. Therefore we have concentrated our analysis of shaded ship on our measurements of the front of the bridge during C runs. But we will first show an example of a type A run measurement, which was a scenario measured by all teams.

The type A run geometry was set up to measure the shaded starboard side of the ship at day time. In this scenario the port side and the front of the bridge were sun illuminated. An IR image from a measurement is shown in Figure 6.12. Figure 6.13 shows a spectrum from the shaded starboard side of the bridge during run 18 measured with the CMT detector. The result from run 31, which was measured with the InSb detector, is shown in Figure 6.14. The spectral signature is similar to the night run measurement, giving radiance from the ship surface close to a blackbody. The calculated apparent temperatures are rather close to air temperatures at the ship, within the estimated precision of the FTIR results. For run 31 the apparent temperature is about 1°C below the air temperature measured at the shore station. The effect of this condition is observed in the spectrum, where atmospheric lines appear as emission lines.

Figure 6.12 Milcam IR image from a day run, measuring the shaded starboard side of the bridge, SIMVEX run 18

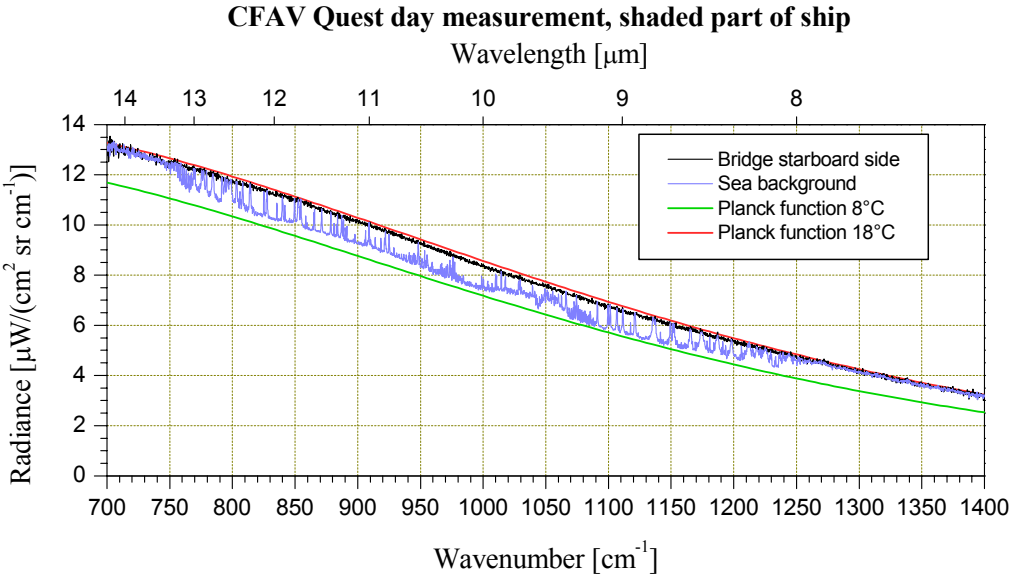

Figure 6.13 Starboard side measurement of shaded bridge at day time with the CMT detector, SIMVEX run 18

We now continue with shaded front of bridge measurements during type C runs. Figure 6.15 shows an IR image of this scenario. Figure 6.16 shows two spectra from the shaded front of the bridge obtained during runs 19 and 38, measured with the CMT detector. The results from runs 14 and 32, which were measured with the InSb detector, are shown in Figure 6.17. Again, all spectra are very close to a blackbody spectrum. The two CMT spectra are almost identical, but we have included both for comparison with sun illuminated parts of the ship in section 6.2.3. The InSb spectra show that the apparent temperature of the surface is different in the two runs.

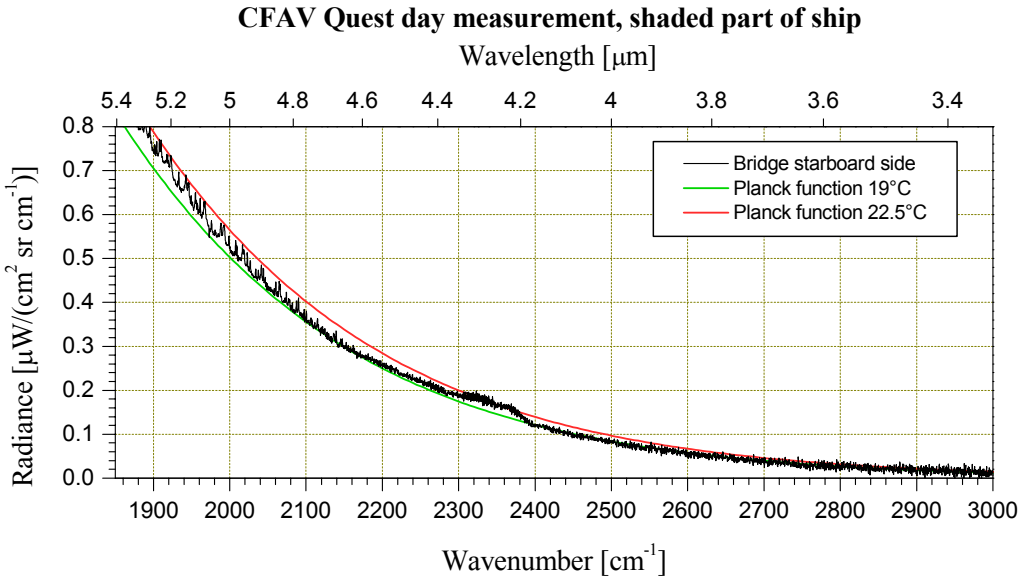

Figure 6.14 *Starboard side measurement of shaded bridge at day time with the InSb detector, SIMVEX run 31*

Figure 6.15 *Milcam IR image from a day run, measuring the shaded front of the bridge, SIMVEX run 32*

6.2.2 Shaded ship temperature comparisons

Table 6.3 and Figure 6.18 show calculated apparent temperature results for the shaded front of the bridge similar to those presented for night runs. The calculated FTIR apparent temperatures are generally close to the air temperatures. During most of the C runs the air temperature difference between the ship and the shore stations is less than 1°C. For this scenario the ShipIR temperature predictions are less than 1°C lower than the apparent FTIR temperatures, except for run 14, where the difference is 2°C. We remind the reader that the shore station air

temperatures were used in these ShipIR simulations, which may deviate from the air temperatures measured on board the ship (see appendix A).

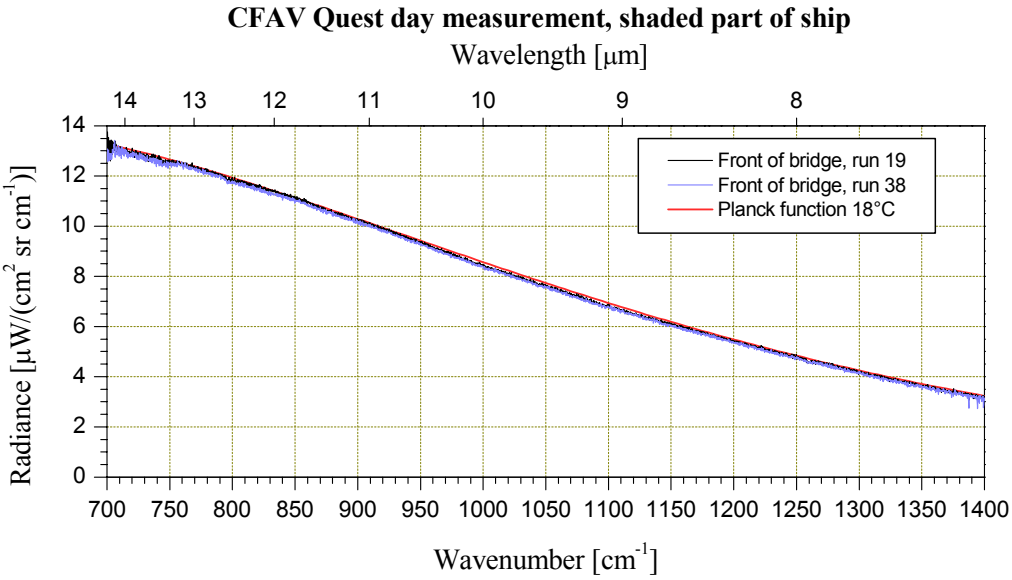

Figure 6.16 Two measurements of the shaded front of the bridge at day time with the CMT detector, SIMVEX runs 19 and 38

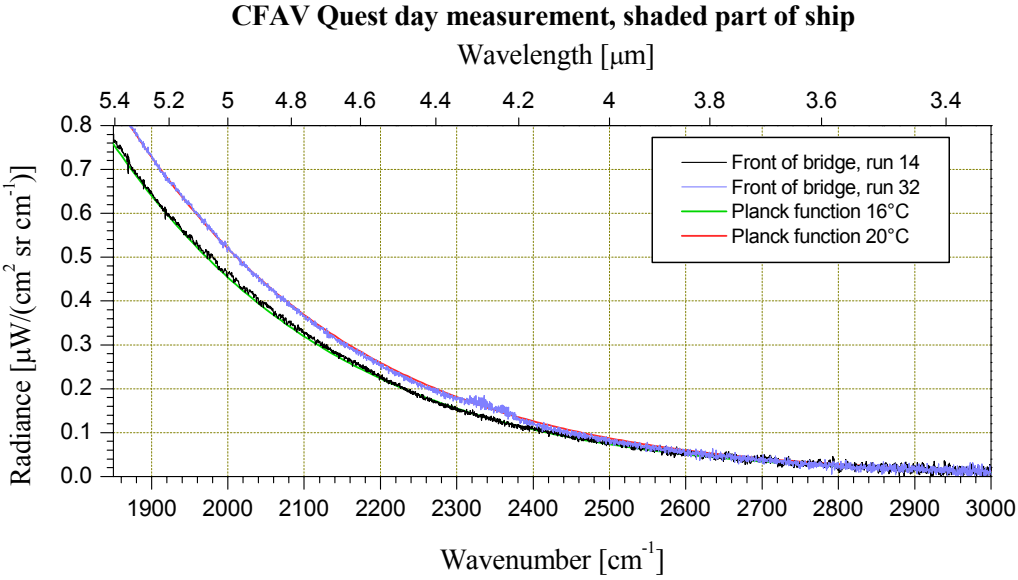

Figure 6.17 Two measurements of the shaded front of the bridge at day time with the InSb detector, SIMVEX runs 14 and 32

Since the spectra from shaded parts of the ship at day time are close to blackbody spectra, we can draw the same conclusions as for the night runs. Except from higher radiance levels due to higher surface temperature, the spectral properties of shaded ship at day time seem to be close to the night time properties. The conditions for foreground reflection from the surface are also to be comparable, since the IR properties of sea and sky do not change much. Thus the contribution from surface reflections may be considered as negligible. It should therefore be possible to model the ship signature assuming a blackbody spectrum, and it should be possible to make a good comparison of results from different IR cameras for this case.

Run	Date	Start run (UTC)	Detec-tor	FTIR equivalent temperature [°C]	I-button measurement [°C] (I 34)	ShipIR surface temperature prediction [°C] (supm_f2_p1)
14	15	21:03	InSb	16.8	14.5	14.9
19	16	21:02	CMT	17.5	16.5	16.7
24	17	21:02	CMT	17.7	16.5	17.3
32	19	20:47	InSb	19.7	15.0	18.7
38	20	21:00	CMT	17.0	16.0	-

Table 6.3 Shaded front of bridge surface temperature comparisons at day

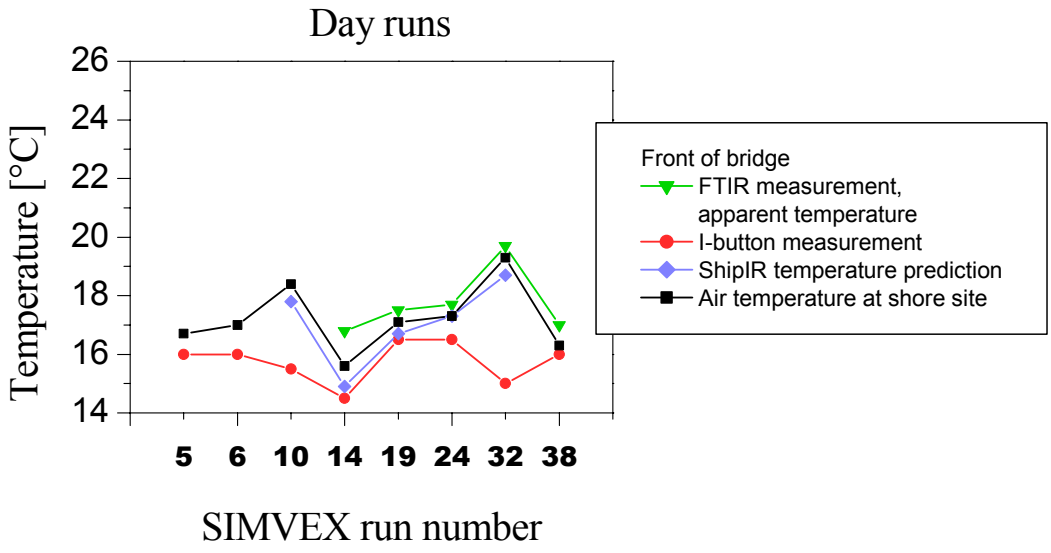

Figure 6.18 Comparison of measured and predicted shaded front of bridge surface temperatures at day

6.2.3 Sun illuminated ship measurements

During C run geometries, the measured port side of the ship was illuminated by sun. Due to variations in cloud cover from day to day, there are also variations in sun intensity, see Table A.4. Sun illumination of the ship side has several implications for the infrared signature of the ship surface.

Due to absorption of light the surface heats up, and thus the emission from the surface increases in the infrared region. The change of surface temperature is a slowly varying function.

A part of the sunlight striking the ship surface is reflected, which again may be divided into two categories. Some light is reflected in random directions, similar to the reflection from a Lambertian surface. For a human observer this diffuse reflection appears as higher light intensity in the sun illuminated than in the shaded part of the surface, as shown in the visible light image of the ship in Figure 6.19. Also in the infrared region we have some diffuse reflection of sunlight, which are shown in spectra below. Spectra presented in this section, are assumed to mainly contain contribution from diffuse reflection, since IR images and FTIR intensities are quite stable during the time of measurement.

Figure 6.19 CCD camera image from a day run, showing the visible contrast between shaded and sun illuminated areas of the ship, SIMVEX run 32

In addition to diffuse reflection, there is also a specular reflection of light, due to more mirror-like properties of the surface. In the image in Figure 6.19 there is specular reflection from parts of the ship hull. This image is almost saturated in most of the sun illuminated parts of the ship. Therefore the image does not represent the intensity of the sun glint as observed with human eyes, and it is difficult to distinguish specular and diffuse reflection in this image. Results from specular sun reflection are presented in section 6.2.6.

Figure 6.20 shows an IR image from the Milcam camera taken while measuring the sun illuminated port side of the bridge. From infrared images it is difficult to separate increased radiation due to surface heating from diffusely reflected light. Two spectra from the port side of the bridge, measured with the InSb detector in run 14 and 32, are shown in Figure 6.21. The spectra show that the apparent radiances from the surface are higher than the path radiance from the atmosphere, especially for run 14, since atmospheric lines appear as absorption lines. The spectra show that the ship side was most heated by the sun in run 14, since the atmospheric lines are most visible here, The consequence is a higher contrast between the sun illuminated and shaded parts of the ship in run 14 than run 32. Even though both runs had good weather, the meterorological conditions are quite different, for instance the wind direction is almost opposite (see appendix A).

Figure 6.20 Milcam IR image from a day run, measuring the sun illuminated port side of the bridge, SIMVEX run 32

In Figure 6.22 the radiance from the sun illuminated hull in run 32 is plotted together with the shaded front radiance, first presented in Figure 6.17. The spectra illustrate the radiance contrast between sun illuminated and shaded parts of the ship. The most striking difference between the spectra presented is that the spectrum from the sun illuminated hull does not fit a blackbody function over a wide spectral region. In the high wavenumber part of the 3-5 μm band, some spectral features of the signature appear. The reason for this is the contribution from reflected sunlight. The effect of reflected sunlight becomes even more evident, if we look at higher wavenumbers, as shown in Figure 6.23 covering the band up to 4800 cm^{-1} (2.1 μm). Above 4000 cm^{-1} we have a spectral region with high atmospheric transmittance. The signal level originating from emission from the ship does not exceed the noise level, as the spectrum from the shaded part of the ship shows. The sun illuminated hull has a strong signature in this region, originating from reflected sunlight. The main reason for the strong sunlight contribution in this band is the spectral distribution of sunlight, which increases strongly with wavenumber due to the high temperature of the sun, while the emission from the ship surface decreases rapidly. A spectrum of the solar irradiance calculated by MODTRAN 4 is presented in Figure 6.24, using the user defined atmospheric profile in Table A.8.

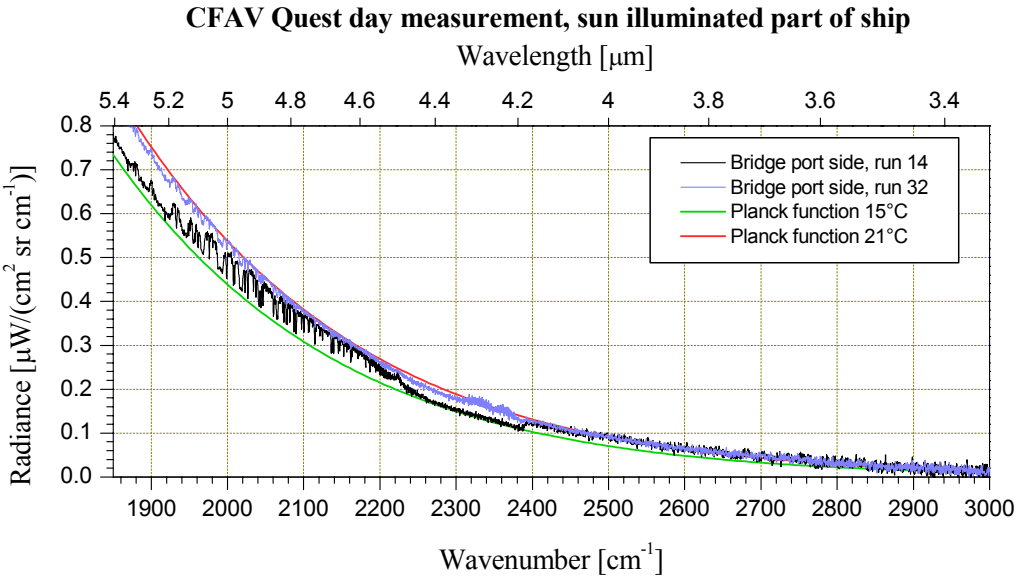

Figure 6.21 Two measurements of the sun illuminated side of the bridge at day time with the InSb detector, SIMVEX runs 14 and 32

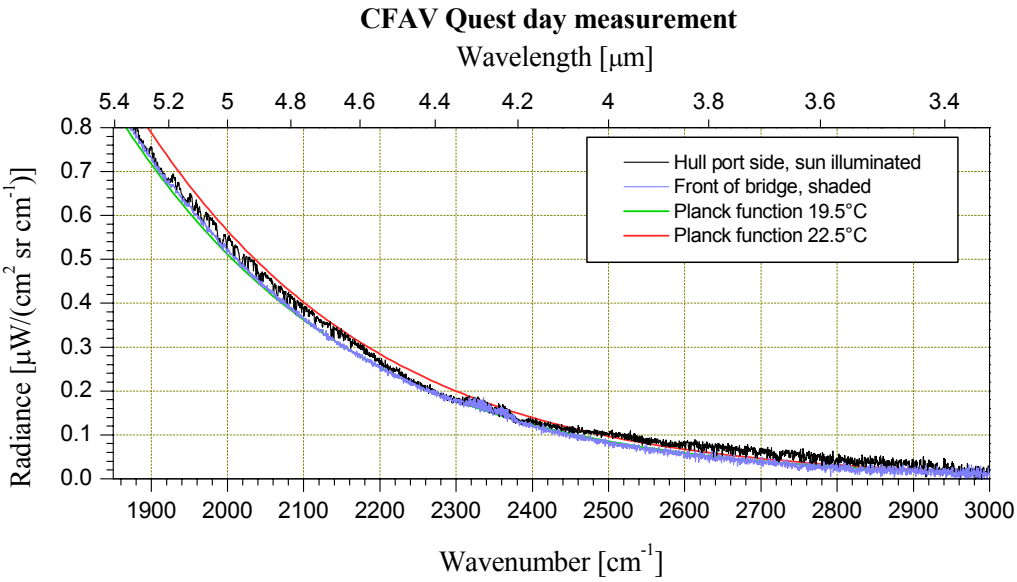

Figure 6.22 Comparison of sun illuminated and shaded parts of the ship measured with the InSb detector, SIMVEX run 32

Although no blackbody function fits the hull spectrum presented in Figure 6.22 and Figure 6.23 over the whole band, we see that the plotted Planck function at 22.5°C fits the low wavenumber part of the spectrum with high atmospheric transmittance quite well. However, in

this scenario it is more uncertain if the selected temperature of the blackbody function represents the equivalent temperature of the surface. Although the spectrum indicates that the contribution from reflected sunlight is small in the low wavenumber region, it could still be significant. In the spectral region with the best atmospheric transmittance (2500-2700 cm^{-1}), the contribution from reflected sunlight is clearly significant, such that the apparent temperature in this region becomes higher than the equivalent surface temperature.

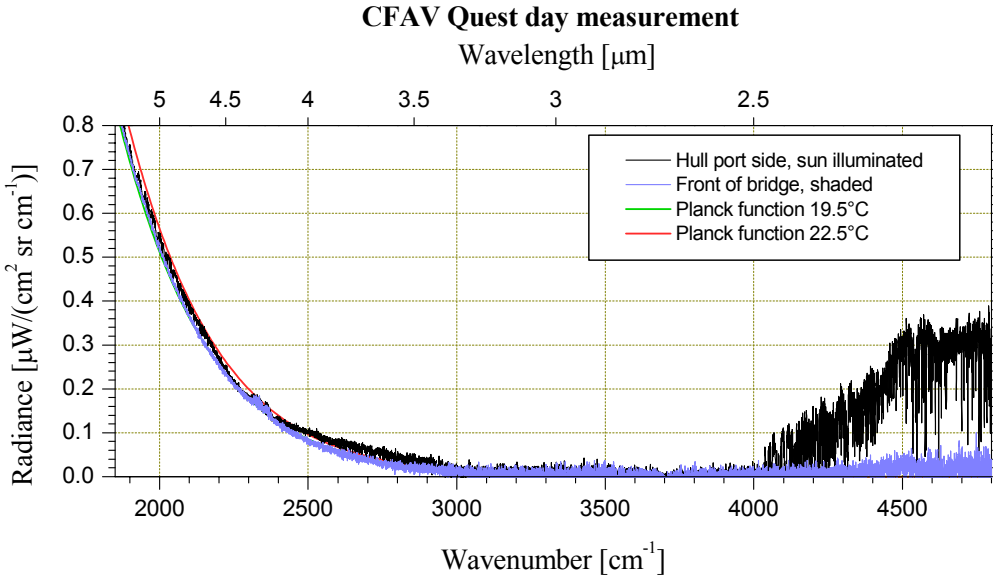

Figure 6.23 Comparison of sun illuminated and shaded parts of the ship, including the high wavenumber part of InSb detector's spectral range, SIMVEX run 32

Figure 6.25 shows an IR image from the Sentinel camera during a day run with sun illumination of the port side of the ship. Two spectra from the bridge, measured with the CMT detector in run 19 and 38, are shown in Figure 6.26. Similar to the InSb results, these spectra show variation in how much the ship surface was heated. While the shaded front spectra presented in Figure 6.16 showed almost equal radiances in these two runs, a clear difference between the runs is observed in Figure 6.26. The spectra show that the ship side was most heated by sun in run 19, where the atmospheric lines clearly appear as absorption lines, resulting in a higher contrast between the sun illuminated and shaded parts of the ship in run 19 than run 38. Again, there are differences in the meteorological conditions. In run 38 the sky was covered by thin clouds, and the solar irradiance was lower than in run 19.

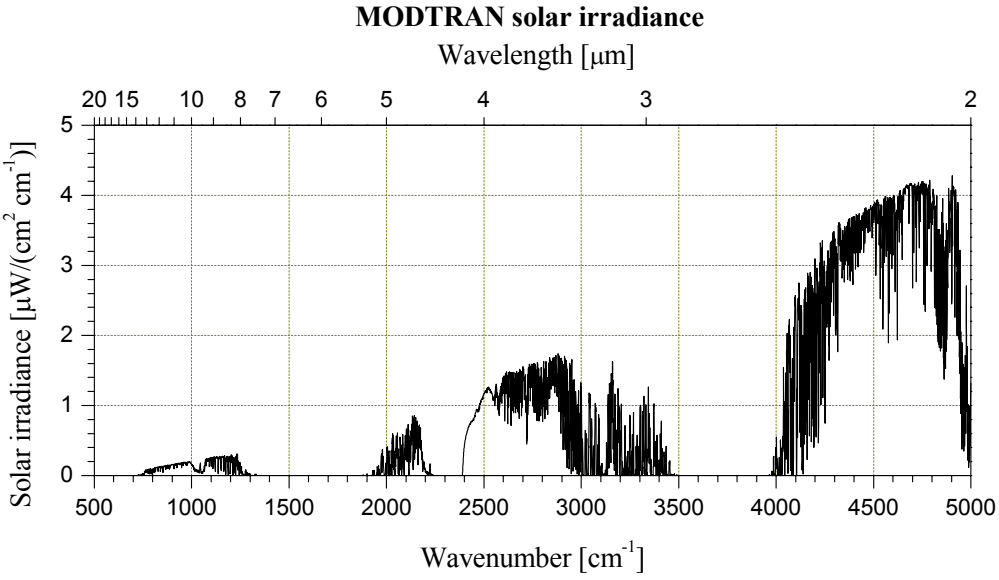

Figure 6.24 Spectral solar irradiance received on the ground calculated by MODTRAN 4, using the user defined atmospheric profile

Figure 6.25 Sentinel IR image from a day run, showing the sun illuminated port side and the shaded front of the ship, SIMVEX run 19

In Figure 6.27 the radiances from the sun illuminated hull in run 19 is plotted together with the shaded front, illustrating the radiance contrast. The figure shows that the hull has a higher radiance than the front. But unlike the InSb spectrum, the spectral distribution of the sun illuminated hull is still close to a blackbody. This indicates that the contribution from diffusely reflected sunlight is negligible. Extending the comparison of the 2-2.5 μm region and 3-5 μm region to the 8-12 μm region, this seems reasonable. Figure 6.24 showed that the contribution from diffusely reflected sunlight is much lower in the low wavenumber region of the 3-5 μm band. When comparing the spectral distribution of solar irradiance (Figure 6.24) with the radiance from the ship surface, the solar irradiance is strongly reduced when we move from the 3-5 μm band to the 8-12 μm band, while the ship surface radiance is strongest in the 8-12 μm

band. In addition the reflection coefficient of the surface paint is lower in the 8-12 μm band, according to the paint reflection measurements.

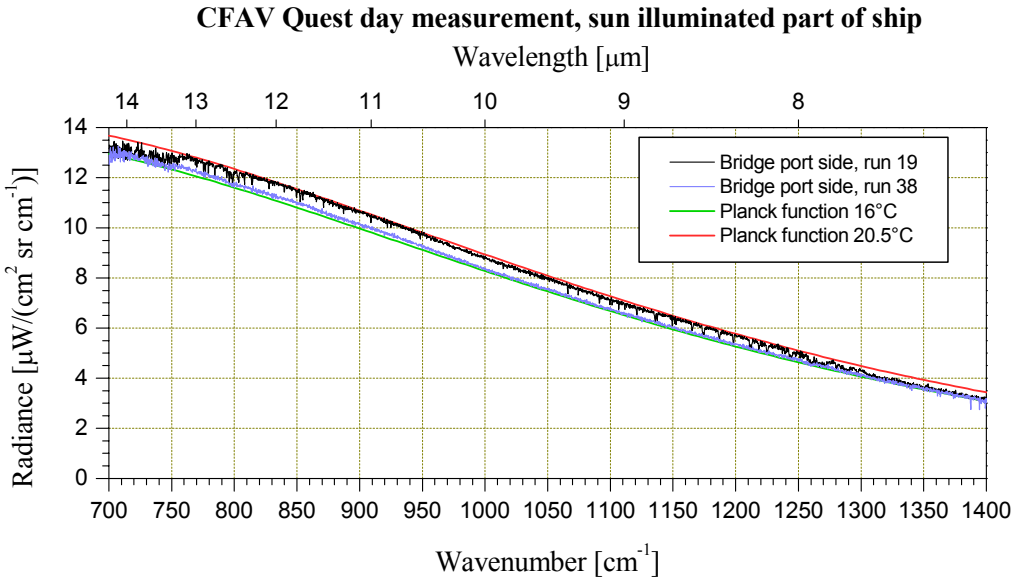

Figure 6.26 Two measurements of the sun illuminated side of the bridge at day time with the CMT detector, SIMVEX runs 19 and 38

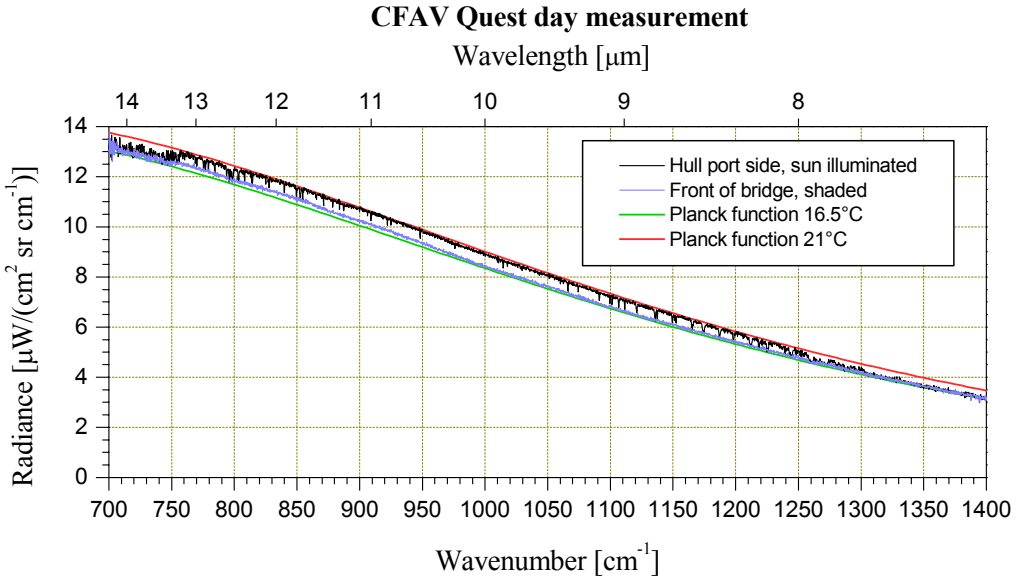

Figure 6.27 Comparison of sun illuminated and shaded parts of the ship measured with the CMT detector, SIMVEX run 19

Figure 6.28 shows the same spectra as Figure 6.27 up to 4800 cm^{-1}. Although the signal to noise ratio for the CMT detector is poor in the high wavenumber region in this figure, the contribution from reflected sunlight is visible above 4000 cm^{-1}. The signal level is comparable with the results from the InSb measurements.

Figure 6.29 shows an IR image from a measurement of the sun illuminated front of the bridge in a run of type A (run 18). Figure 6.30 show a spectrum from the front of the ship in another run of type A (run 31). In this scenario the front is strongly illuminated by the sun, the contribution is visible in the spectrum, especially in the high wavenumber region. However, the heating of the surface seems to be quite small, indicated by weak atmospheric absorption lines in the low wavenumber region of the figure. The FTIR field of view covers an area a little above the I-button position. The calculated apparent temperature is 21.6°C, while the measured temperature with I-button I34 was 18.5°C. The surface temperature predicted by ShipIR for the same plate is 33.1°C, far above the measurements, but the predictions for adjacent plates were up to 6° lower than this temperature. According to the image in Figure 6.29, these large temperature gradients do not seem reasonable.

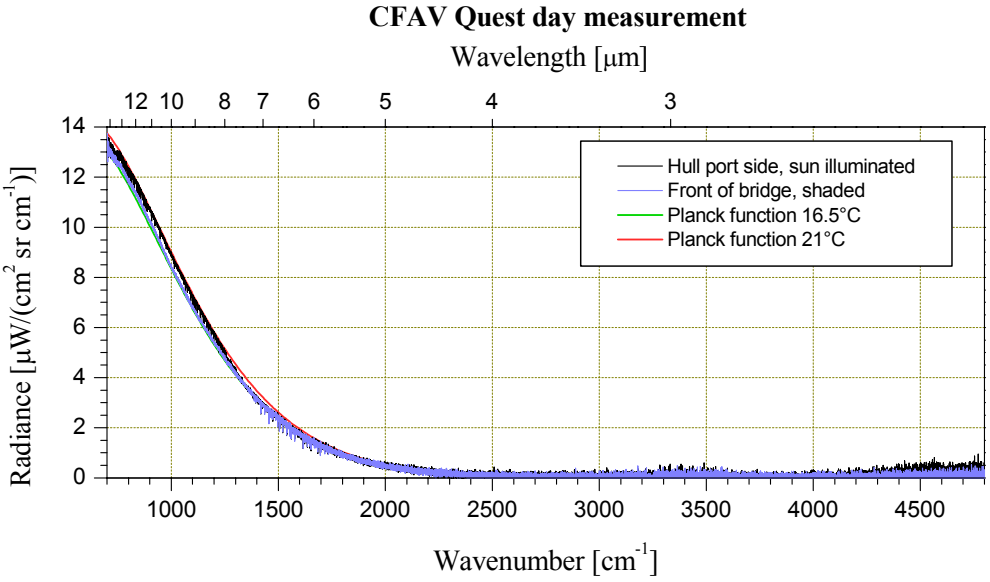

Figure 6.28 Comparison of sun illuminated and shaded parts of the ship, including the high wavenumber part of CMT detector's spectral range, SIMVEX run 19

Figure 6.29 Milcam IR image from a day run, measuring the sun illuminated front of the bridge, SIMVEX run 18

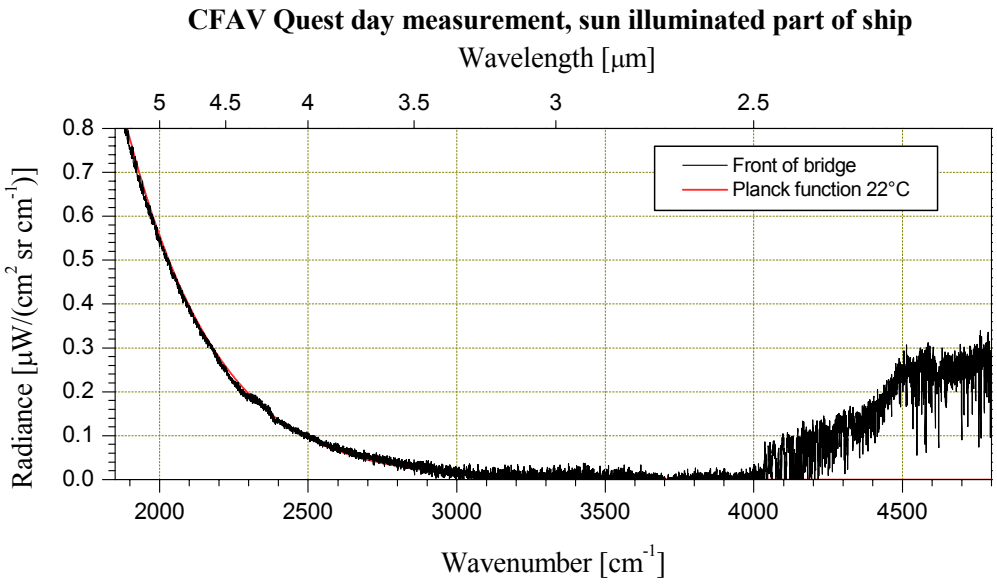

Figure 6.30 Sun illuminated front of bridge measurement with the InSb detector at day, SIMVEX run 31

Regarding ship modelling and IR camera result comparisons, our earlier conclusions should also be valid for the 8-12 μm band when the ship is sun illuminated. However, in the 3-5 μm band, the result of an equivalent blackbody temperature calculation is dependent on the selected optical bandwidth. A consequence is that even though all IR cameras measured the same scenario at the same time, one cannot expect to get the same results when converting images to equivalent temperatures, if the spectral response of the cameras is different. Thus comparison of IR images from different cameras used during the SIMVEX trial should be made with caution, when the observed object is the sun illuminated ship.

6.2.4 Sun illuminated ship temperature comparisons

Similarly to the night runs, the different day run measurements of the side of the bridge do not show many variations in spectral features, so we do not show every spectrum. We observe variations in apparent temperature from run to run, and to some extent variation in the contribution from diffusely reflected sunlight. Similarly, the different spectra of the shaded front of the bridge only show variation in apparent temperature.

The measurements of the ship hull generally give results close to the bridge side measurements, but some differences in apparent temperature are observed. The contribution to the spectrum from reflected sunlight seems to be a bit higher for the hull than for the bridge. A Milcam IR image of a sun illuminated hull measurement is shown in Figure 6.31.

Figure 6.31 Milcam IR image from a day run, measuring the sun illuminated port side of the hull, SIMVEX run 32

As earlier we have calculated the apparent temperatures for the bridge and the hull from each run. As mentioned in section 4.2.3, we have calculated the apparent temperature in two different spectral regions for some of the InSb detector runs. Some day and night measurements of the ship hull were selected. In addition to our normal calculation at 2100 cm^{-1}, we have also calculated the apparent temperature from the average of the spectrum between 2600 and 2700 cm^{-1}. The latter is rather uncertain, due to the poor signal to noise ratio in this spectral region. Figure 6.32 shows the calculated apparent temperatures for the selected runs, together with the thermocouple measurements and the air temperature at the shore site.

The figure shows significant differences in calculated apparent temperature for the two spectral regions, when the ship is strongly sun illuminated (run 14 and 32). Thus the influence of diffusely reflected sunlight is illustrated. When the sun illumination is weak (run 5) and at night time the differences between the two spectral regions are small (within the precision of the calculation). At night time a consequent lower apparent temperature is observed in the 2600-2700 cm^{-1} spectral region, compared to the apparent temperature at 2100 cm^{-1}. Although the apparent temperature calculated in 2600-2700 cm^{-1} spectral region is rather uncertain due to poor signal to noise ratio, the foreground sky and sea radiation reflected from the ship surface (discussed in section 6.1.1), could be the reason for this difference.

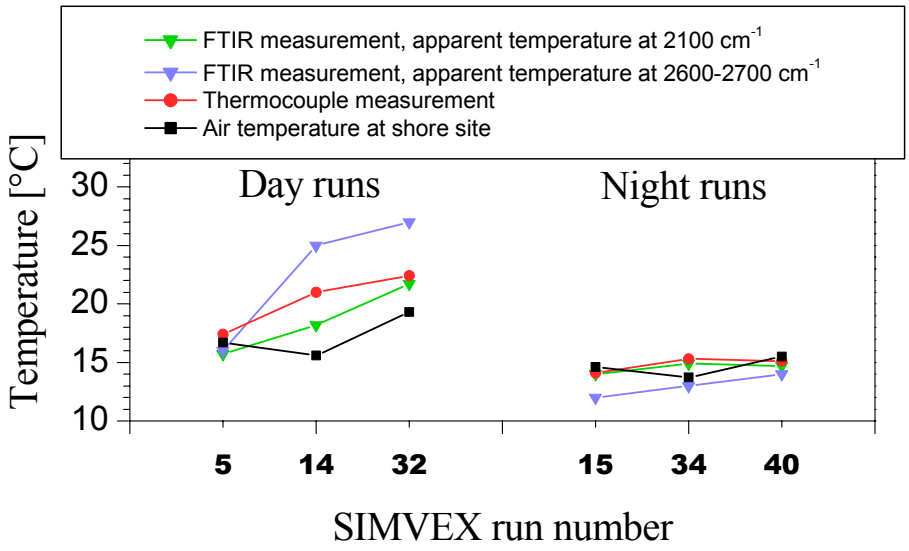

Figure 6.32 Comparison of temperatures, using two different spectral windows for FTIR apparent temperature calculation

Table 6.4 and Figure 6.33 show calculated apparent temperatures at 2100 cm^{-1}, thermocouple measurements and ShipIR predictions for the port side of the bridge during day runs, similar to those presented earlier.

Run	Date	Start run (UTC)	Detec-tor	FTIR apparent temperature [°C]		Thermocouple measurement [°C]		ShipIR surface temperature prediction [°C]	
				Bridge	Hull	Bridge (T01)	Wall deckhouse (T21)	Bridge	Hull
5	13	20:59	InSb	15.2	15.7	17.4	17.4		
6	13	22:18	CMT	16.0	16.0	18.1	18.2		
10	14	20:56	CMT	19.1	19.8	21.1	21.1	21.6	22.5
14	15	21:03	InSb	20.0	18.2	21.2	22.0	25.3	27.0
19	16	21:02	CMT	20.0	20.5	21.6	22.1	25.2	26.8
24	17	21:02	CMT	18.7	18.7	20.4	20.2	23.4	24.6
32	19	20:47	InSb	20.7	21.7	22.7	22.4	23.1	24.1
38	20	21:00	CMT	16.9	17.4	18.1	17.8		

Table 6.4 Sun illuminated of bridge and hull surface temperature comparisons at day

Although the contribution from reflected sunlight seems to be small in this spectral region, the calculated apparent temperatures may still be affected by the sunlight contribution. Thus the

apparent temperatures could be higher than the real surface temperatures. In spite of these assumptions, the calculated apparent temperatures are a little lower than the thermocouple temperatures, but higher than the air temperature (Figure 6.33), so the heating effect is confirmed (except for test runs 5 and 6 when the sun intensity was low). The ShipIR calculations predict a much higher temperature than what we have observed. The results confirm the results presented in (3), which indicate a temperature overprediction by ShipIR in this scenario.

6.2.5 Sun illuminated funnel

The yellow painted funnel was also measured during most of the C runs. Figure 6.34 shows an IR image from a measurement of the sun illuminated funnel. Figure 6.35 and Figure 6.36 show results from the spectral measurements of the funnel for runs 19 and 32, measured with the CMT and InSb detectors respectively. Measurements of the sea background for each run are included in the plots.

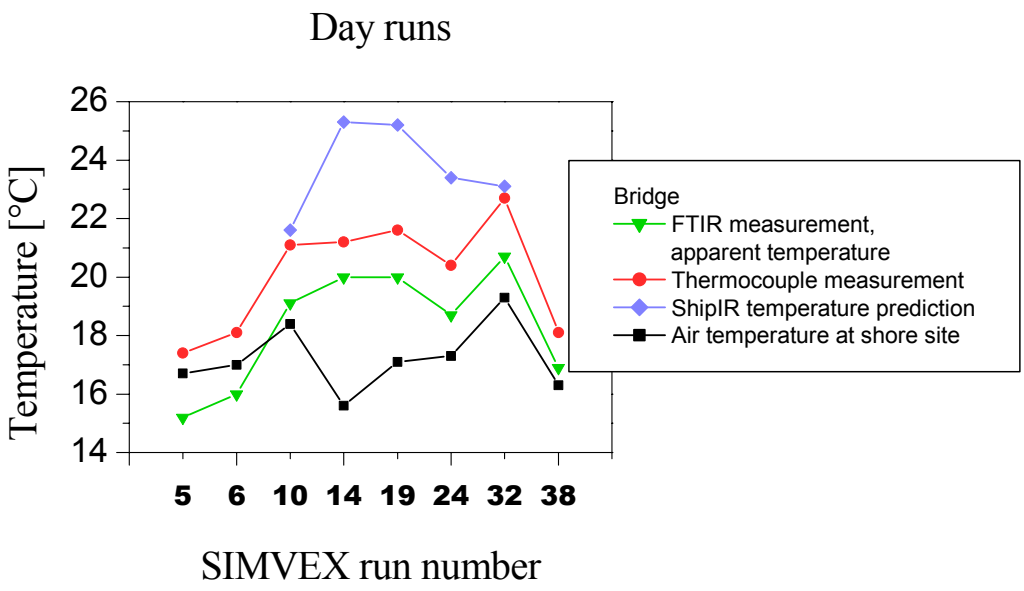

Figure 6.33 Comparison of measured and predicted surface temperatures on sun illuminated port side of bridge at day time

In section 6.1.4 we observed that the coolest part of the funnel was only slightly warmer than the ship hull. Figure 6.35 and Figure 6.36 both show that the apparent temperature of the funnel increases more than the hull when the surface is sun illuminated. The great temperature difference between the measured source and the air makes the atmospheric lines more visible in the spectrum. But in regions with good atmospheric transmittance the spectrum still fits a

blackbody function quite well. The result indicates that the contribution from reflected sunlight is negligible also for the yellow paint in the 8-12 μm region.

Figure 6.34 Milcam IR image from a day run, measuring the sun illuminated port side of the funnel, SIMVEX run 32

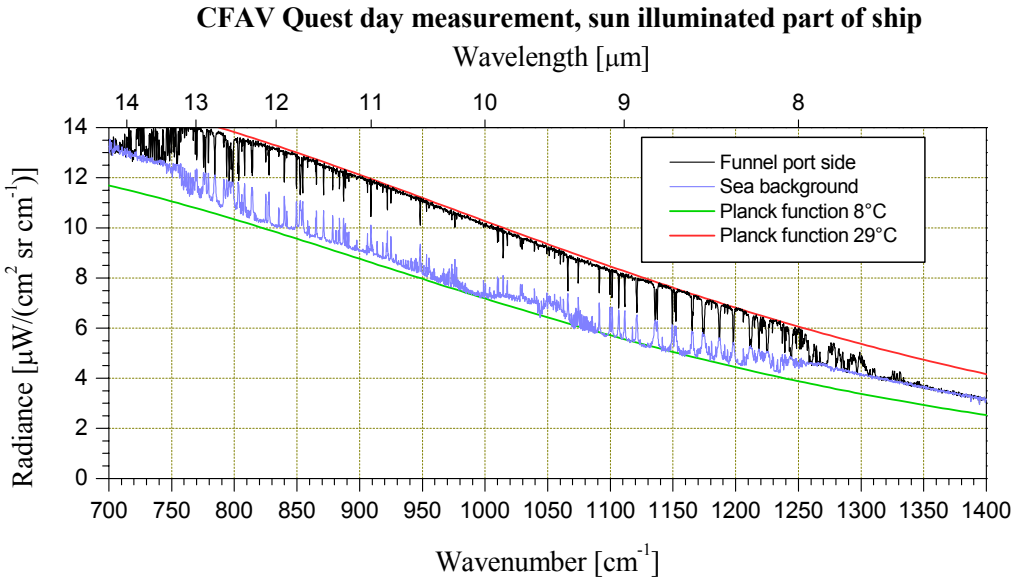

Figure 6.35 Port side measurement of the funnel and the sea background at day time with the CMT detector, SIMVEX run 19

As for the white paint, the InSb spectrum from the funnel in Figure 6.36 clearly shows a contribution from the reflected sunlight. The plotted blackbody function indicates an increased apparent temperature comparable with the CMT result. The plotted blackbody function only fits the measured spectrum over a narrower band than our previous examples. The main reason is that with this high temperature contrast between the measured object and the atmosphere, the effect of spectral variations in atmospheric transmittance in the low wavenumber region becomes more visible. And again it would not be correct to use the spectral region with best

atmospheric transmittance (2500-2700 cm^{-1}) for apparent temperature calculations, because of the contribution from reflected sunlight. Figure 6.37 shows the high wavenumber region of the funnel measurement. As for the white paint, the sun reflection gives a significant signature in this region. But the values for the yellow paint measurement are slightly below the white paint results, indicating a lower reflection in this region.

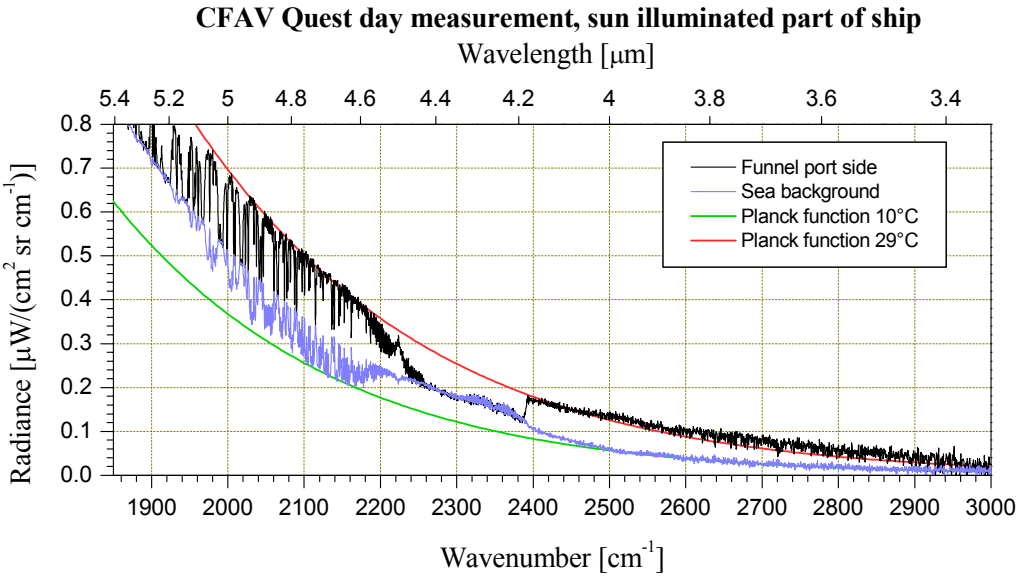

Figure 6.36 Port side measurement of the funnel and the sea background at day time with the InSb detector, SIMVEX run 32

6.2.6 Specular sun reflection

For many materials the properties of light reflection from the surface are mirror-like, so that energy from the radiating source is reflected in a narrow angle related to the incoming angle. During the C type runs this kind of reflection was observed from the surface of CFAV Quest. We made a measurement with the FTIR instrument using the InSb detector while a reflection was observed. Figure 6.38 and Figure 6.39 show simultaneous IR images from the Milcam and Sentinel cameras with specular reflection of sunlight from the ship hull. The area with specular reflection appears very intense compared to the rest of the hull in the Milcam image, and the camera is saturated in this area.

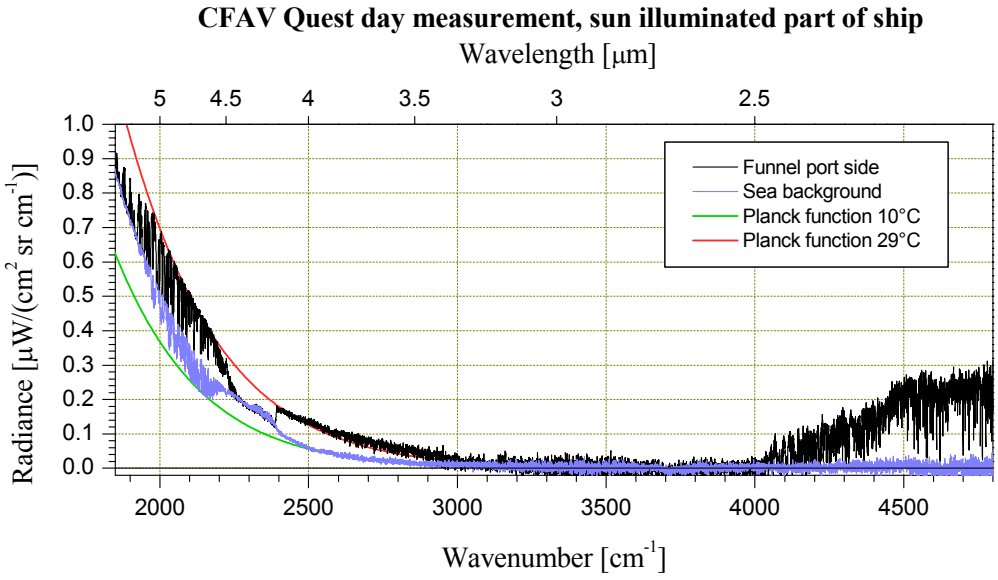

Figure 6.37 *Port side measurement of the funnel and the sea background at day time, including the high wavenumber part of the InSb detector's spectral range, SIMVEX run 32*

Figure 6.38 *Milcam IR image (3-5 µm) from a day run, measuring specular sun reflection from the port side of the hull, SIMVEX run 32*

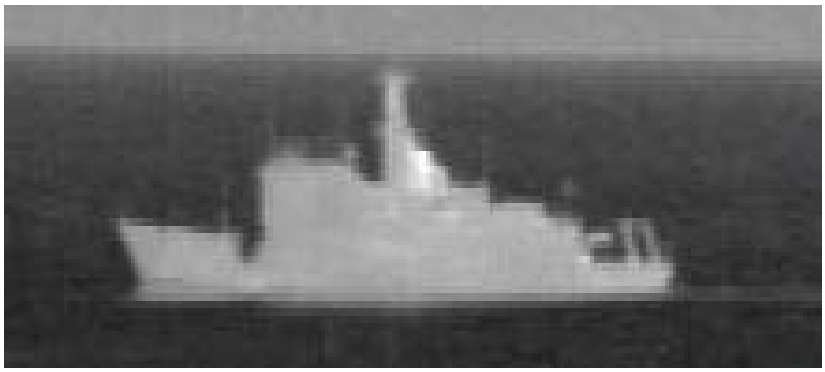

Figure 6.39 *Sentinel IR image (8-12 µm) from a day run, in a scenario with specular sun reflection from the port side of the hull, SIMVEX run 32*

Figure 6.40 and Figure 6.41 show the spectra of diffuse and specular sun reflection from the ship hull, measured with the InSb detector. Due to movements of the ship caused by waves, the intensity of reflected light varies through this measurement, and the presented results should be considered as an average. The figures show that specular reflected sunlight has spectral characteristics quite similar to diffusely reflected sunlight. However, the intensity is much higher throughout the entire covered spectral region. Again the intensity is increasing with wavenumber. Taking a closer look at the spectra, we observe spectral variations in how much the intensity increases when specular reflection occurs. Around 2600 cm^{-1} the radiance difference between parts of the ship illuminated by diffusely reflected sunlight and shaded part of the ship (Figure 6.23) is about 0.025 $\mu W/(cm^2\ sr\ cm^{-1})$, while the difference between the hull measurements with and without specular reflection (Figure 6.41) is about 0.25 $\mu W/(cm^2\ sr\ cm^{-1})$. The values indicate that the specular reflection in this spectral region gives a signature about 10 times the diffuse reflection (The effect of increased surface temperature is omitted, but would have increased the factor if included). If we make the same comparison around wavenumber 4500 cm^{-1}, we get the values 0.3 and 0.7 $\mu W/(cm^2\ sr\ cm^{-1})$, respectively, giving a factor of 2.3. Thus the relative effect of specular reflection is much higher in the 3-5 µm region than in the 2-2.5 µm region.

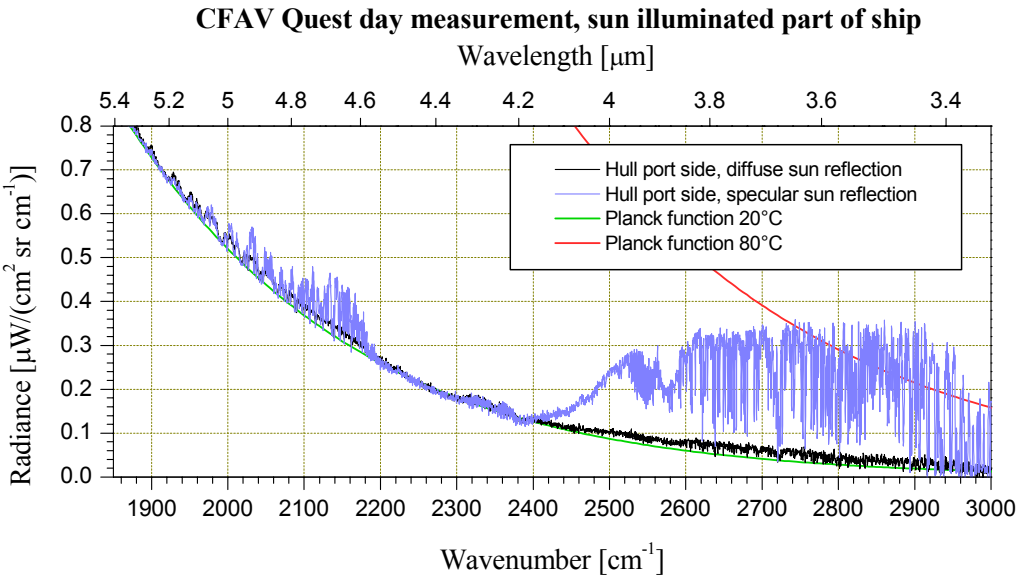

Figure 6.40 Comparison of specular and diffuse sun reflection from the ship hull, measured with the InSb detector, SIMVEX run 32

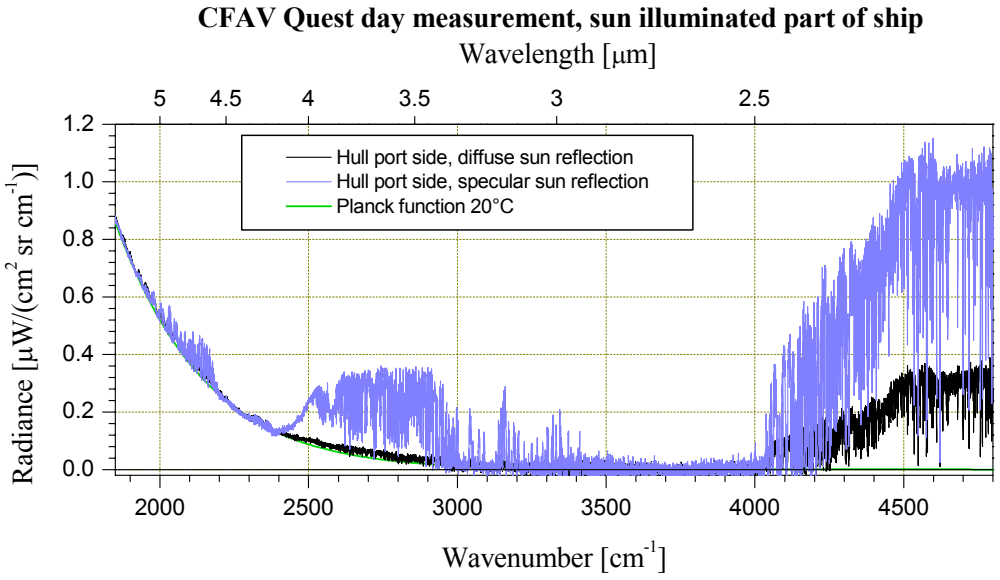

Figure 6.41 Comparison of specular and diffuse sun reflection from the ship hull, including the high wavenumber part of the InSb detector's spectral range, SIMVEX run 32

The ship hull was not measured with the CMT detector when specular sunlight reflection was present. According to the measurements of diffuse sunlight reflection, spectral radiance from the sun, and spectral measurements of the paint reflection, the effect of specular reflection in the 8-12 μm band is expected to be much smaller than the 3-5 μm band. This expectation is also confirmed by the Sentinel image in Figure 6.39. Due to smaller temperature difference, (and different gain and contrast settings for the camera), the contrast between the shaded front and the sun illuminated side of the ship appears less visible in this image than the Sentinel image shown in Figure 6.25. Although the camera is not very sensitive, any contribution from specular sun reflection should have been visible, if it had been significant. Still, with the lack of direct spectral measurements, specular reflection cannot be ruled out in the 8-12 μm band. Further measurements of this scenario in future trials are preferable.

6.2.7 DRDC-V test panels

The ship made a few runs with two painted test panels mounted on the deck. The panels were prepared by Defence Research & Development Canada – Valcartier (DRDC–V) to study the infrared properties of the paint. Figure 6.42 shows two visible images of the panels. In the image to the left, the ship was in a position with normal sun illumination, without specular reflection from the panels. In the image to the right, the ship had moved to a position giving specular reflection from the panels, especially from the panel to the left. Maximum reflection from the two panels occurred at different times. Due to ship movement the background also changes, such that the background above the panels in the image to the right consists of other

parts of the ship. Figure 6.43 shows an IR image of the latter scenario, dominated by specular reflection from one of the panels.

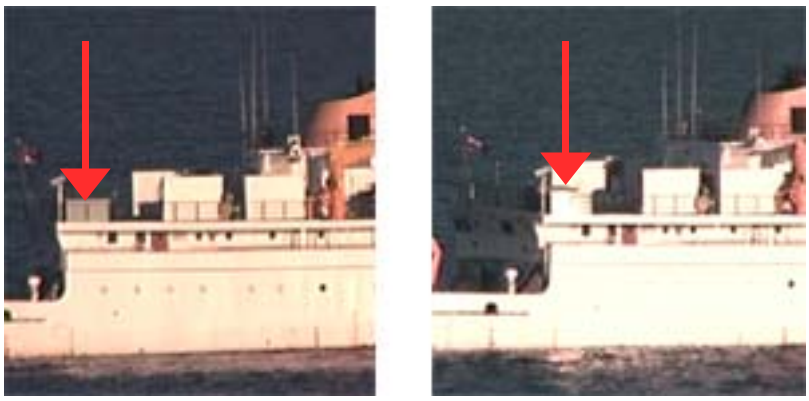

Figure 6.42 Images of the two grey test panels from DRDC-V mounted on the starboard side of CFAV Quest, illuminated by sun. In the image to the right there is specular reflection, especially from the panel to the left, SIMVEX run 33C

The spectral radiance from the panels was measured with the InSb detector, and is shown in Figure 6.44. The absolute values of the result are quite uncertain. The time interval with specular reflection is rather short, reducing the signal to noise ratio of the spectrum. During the measured interval there were strong intensity fluctuations. The panels did not fill the field of view of the spectroradiometer, and it was not possible to separate the two panels while they were measured. The presented radiance is the average from all objects inside the instrument's field of view. According to the right image in Figure 6.42, the specular reflection is probably dominated by one of the panels. Thus the true radiance from the panels is higher than shown in Figure 6.44. Since the absolute values of the panel spectrum reach almost the same level as the ship hull spectrum in Figure 6.41, we expect that the reflection is higher in the panels. The spectral distribution of the reflected sunlight is very similar in the panel and hull spectra. These results could be analyzed further by taking the area of the panels into account.

Figure 6.43 Milcam IR image, from the measurement of specular sun reflection from the test panels mounted by DRDC-V, SIMVEX run 33C

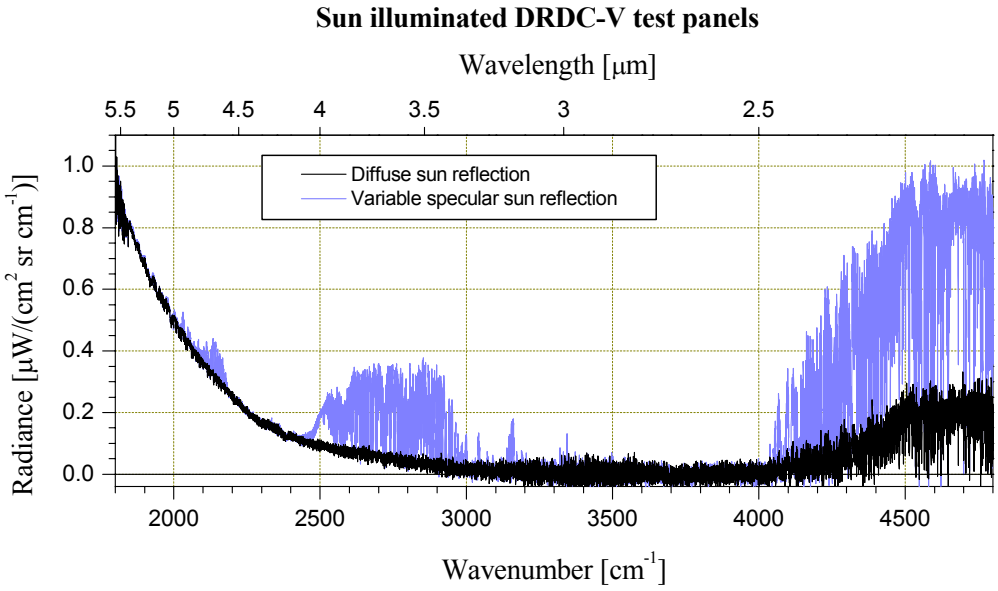

Figure 6.44 Comparison of specular and diffuse sun reflection from panels supplied by DRDC-V, measured with the InSb detector, SIMVEX run 33C

7 SHIP PLUME MEASUREMENTS AND MODELLING

The CFAV Quest is equipped with both gas turbine and diesel engines. Unfortunately the gas turbine engines could not be applied during the SIMVEX trial, so we were able to measure the plume only from the diesel engines. The ship plume was measured in separate runs. During these runs the engines were run at maximum power in order to obtain maximum IR intensity from the plume.

Figure 7.1 shows an IR image of the plume. The spectroradiometer's field of view is the area inside the circle. We see that the size of this plume is very small compared to the field of view of our FTIR instrument.

This reduces the signal to noise ratio of the calculated plume spectra and causes higher uncertainty in absolute radiance values. The intensity variations observed in individual spectra has shown that the intensity is very sensitive to the aiming position of the instrument, which varies slightly because of manual tracking. The results indicate that most of the radiance originates from the area with high intensity close to the stack outlet seen in the IR image. It was not easy to keep this area inside the field of view, and at the same time the hot stack outlet outside the field of view. Therefore the number of interferograms available for averaging in each run is limited, reducing the signal to noise ratio further. The data we present are from the

second part of the plume runs, after the ship had turned, as the best signal to noise ratio was obtained then.

Figure 7.1 Milcam IR image from a measurement of the ship plume, SIMVEX run 23B

Regarding the quality of the FTIR measurements it would have been more optimal to measure the ship plume at shorter distance, but due to shallow waters near the shoreline, it might have been risky for the ship to come closer to the shore station. Our results of the measured plume are presented in section 7.1. A summary of the plume runs and meteorological parameters is presented in appendix A. A description FTIR measurements of combustion gases and results from short-range measurements are given in (21) and references cited in (21).

During the trial, a gas analyzer mounted by Davis in the stack outlet measured the temperature and concentration of several exhaust gases. The total spectral radiance from a plume is determined by the thickness of the plume, as well as the temperature and the concentration of each molecule contributing to the radiance. We have performed an analysis of the measured spectral radiance from the plume in the 3-5 μm band to see if we were able to estimate the temperature of the plume and concentration of contributing molecules from our data. In this work we have used the FASCODE program to model the radiance from a plume, and we have developed additional software to compare the modelled plume with measured results (8). We will show that for a set of temperatures and concentrations, the apparent spectral radiance of the modelled plume approaches the measured spectrum. Since the precision of the InSb results is uncertain, and the CMT measurements too poor to be used at all, the resulting values are also quite uncertain, and should be used with caution. The results obtained by the plume model are described in section 7.2.

After we had established a model of the plume radiance in the 3-5 μm band, we have used the model to simulate the spectral plume radiance in the 8-12 μm band. We also ran simulations to estimate the spectral radiance for both bands at other distances. These additional simulations are presented in section 7.3.

7.1 Measured spectral plume radiance

The measured spectral radiances from the plume and the sea background in run 23A are presented in Figure 7.2. These spectra are calculated with maximum resolution for the interferograms recorded with the InSb detector, 0.5 cm^{-1}. We see from the figure that the plume spectrum contains several characteristic line patterns. The line patterns are emission lines that originate from different molecules in the combustion gas.

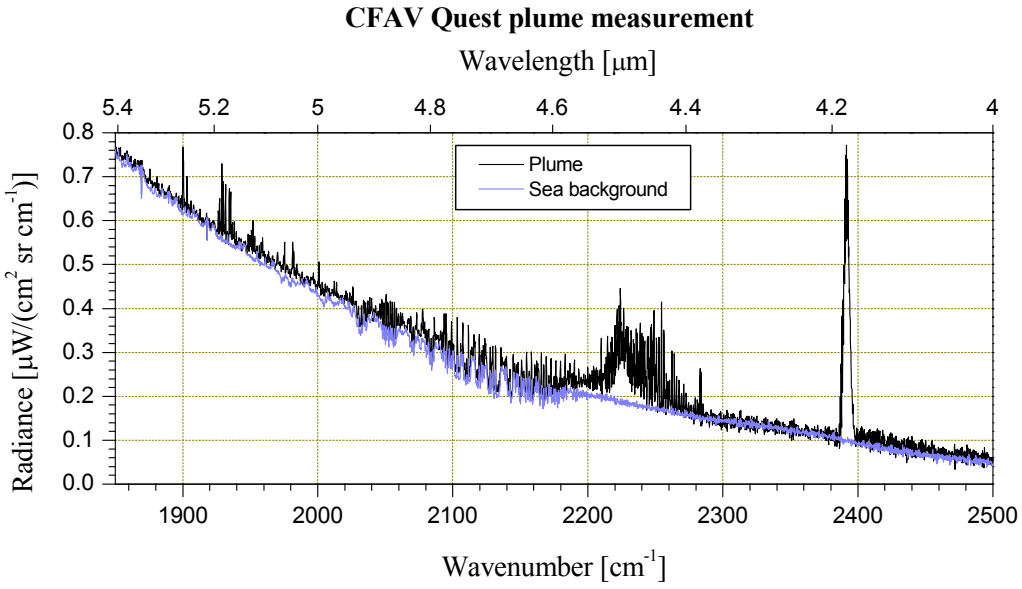

Figure 7.2 Measurement of the plume and the sea background with the InSb detector, SIMVEX run 23A, second part. Resolution 0.5 cm^{-1}

We also tried to measure the plume radiance with higher spectral resolution (0.2 cm^{-1}). The noise then increases if the same number of interferograms is averaged. At the same time the peak intensity should increase for narrow emission lines that are not completely resolved at lower resolution. The results from run 23B are shown in Figure 7.3. This spectrum has increased noise compared to the run 23A spectrum, but some emission lines are better resolved. The CO_2 emission lines in the spectral region 2380 to 2400 cm^{-1} are shown in Figure 7.4 for the two runs. In total, we think that the measured spectrum from run 23B is the best plume spectrum obtained during the SIMVEX trial, and we have chosen that result for our further analysis in sections 7.2 and 7.3.

Since the radiant intensity of the plume is too small to be optimal, the increased engine power was important to achieve the results presented in Figure 7.2 and Figure 7.3. For comparison we have included a spectrum of the plume from an ordinary type C run, with ship speed 10 knots. The intensity of the emission lines is very small in this spectrum, which is shown in Figure 7.5.

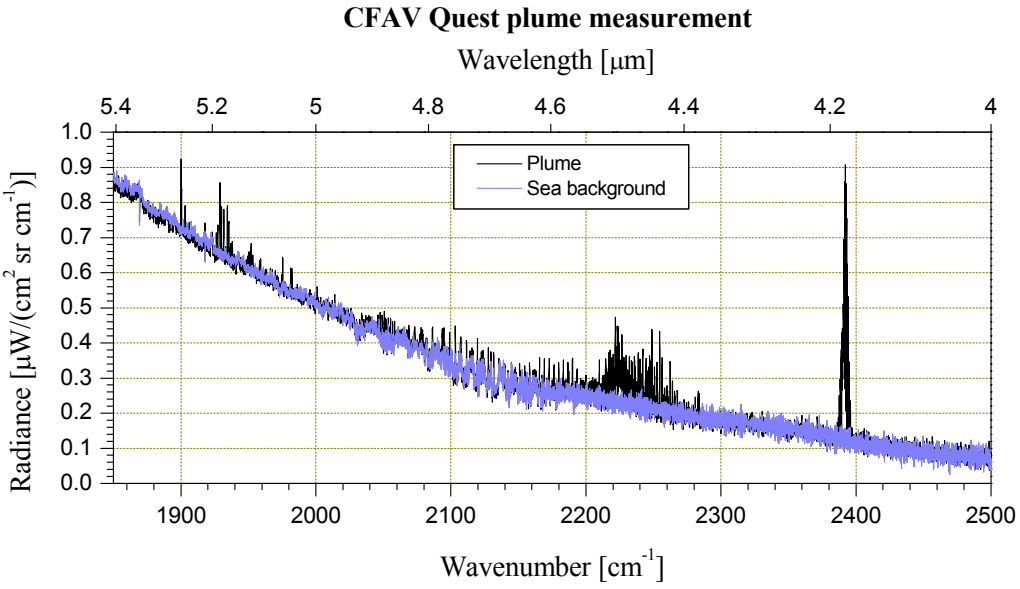

Figure 7.3 High resolution (0.2 cm^{-1}) measurement of the plume and the sea background with the InSb detector. SIMVEX run 23B, second part

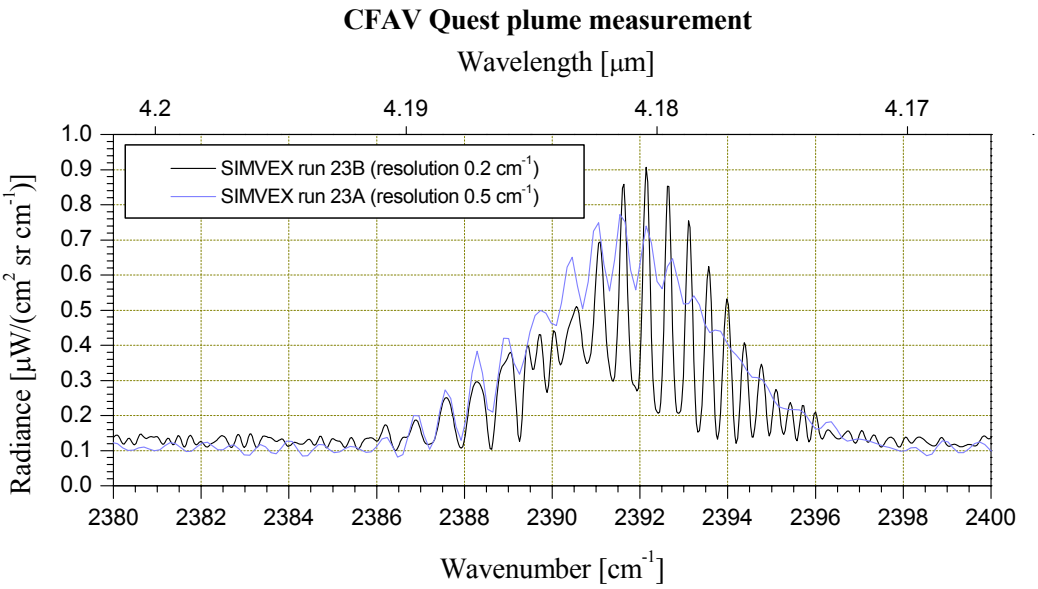

Figure 7.4 Two measurements of the plume with different resolution with the InSb detector

It is noted that not all lines are reduced with the same factor from Figure 7.2 to Figure 7.5, which indicates variations in the relative concentration of different molecules, when the engine power changes. Studying the gas analyzer data, large differences in infrared signature are not surprising. At 10 knots the plume temperature is typically reduced with 150°C, and the

concentrations of CO_2 and NO are reduced with 50-75%, compared to maximum engine power.

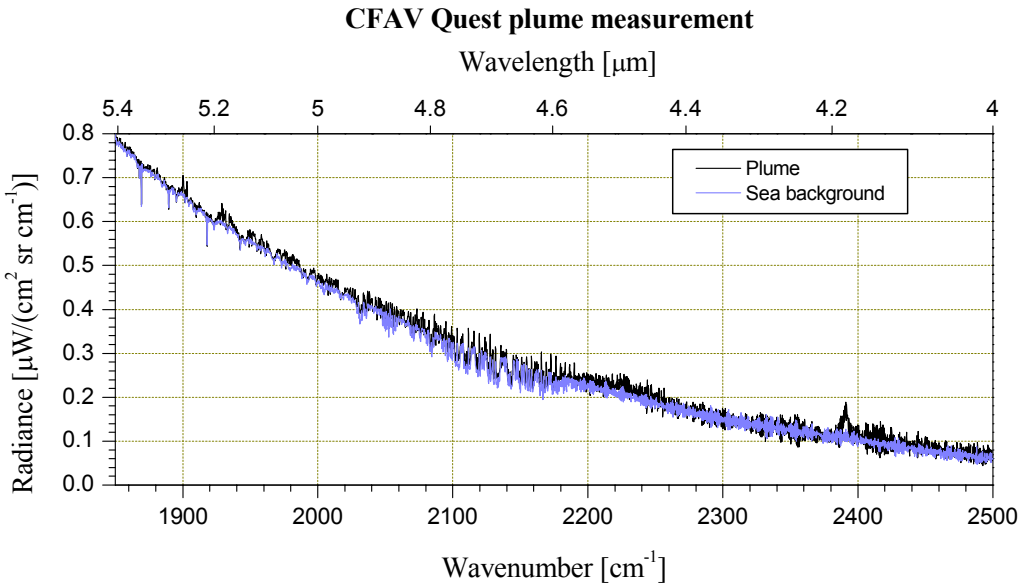

Figure 7.5 Measurement of the plume and the sea background with the InSb detector during an ordinary ship night run, SIMVEX run 21, resolution 0.5 cm^{-1}

In run 25, we used the CMT detector to measure the spectral plume radiance in the 8-12 μm band. The radiance from the plume and the sea background is presented in Figure 7.6. We see that the difference between the plume and background spectra is generally very small, giving too poor signal to noise ratio to use this result for further analysis. Reducing the resolution does not help much. Since the emission lines are narrow, their intensity is generally more reduced than the noise when reducing the resolution. But we will comment on this result again in section 7.3.2, when we present a modelled spectral radiance of the plume in the 8-12 μm band.

7.2 Modelling the spectral plume radiance to estimate temperature and chemical composition

7.2.1 Parameters affecting the spectral plume radiance

The radiance from a combustion gas may be modelled using the FASCODE program, with thickness, temperature and molecular concentrations input as parameters. In section 2.5.3 we

described how the measured spectrum from a plume is influenced by the size of the plume, the background radiance, the atmospheric transmittance and the path radiance.

The background radiance was measured after each plume measurement. We tried to keep the aiming pitch angle for the background measurement unchanged from the plume measurement. The purpose was to obtain a background spectrum that also represents the background we had during the plume measurement. Knowing the meteorological parameters during the measurement, the atmospheric transmittance and path radiance may be found using the FASCODE software.

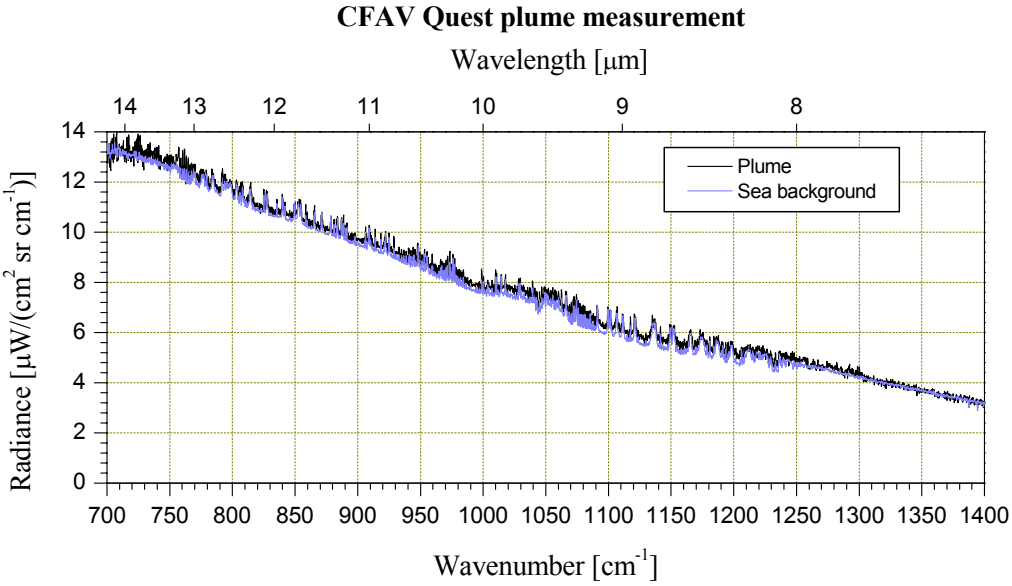

Figure 7.6 Measurement of the plume and the sea background with the CMT detector, SIMVEX run 25, second part, resolution 0.5 cm^{-1}

The spectrum from the plume is also expected to contain a contribution from hot soot particles. The spectral distribution of this contribution is typically close to a blackbody distribution, and should be visible in spectral regions with few gas emission lines, for instance 2400-2500 cm^{-1}. Figure 7.2 shows that the plume spectrum level only exceeds the background level by a small amount in this region. The soot contribution from this ship's plume is thus too small to be characterized by the FTIR measurement. Therefore we have not included any contribution from soot in our model.

7.2.2 Plume size estimate

To get any further in our analysis, we need to estimate the size and thickness of the plume. Leaving the stack outlet, the combustion gas is expected to cool down gradually, and the

concentration of molecules is gradually reduced, as the combustion gas is mixed with air. In our analysis we have not attempted to model this process. We have instead used a simplified model where a limited volume of the combustion gas has a constant temperature and constant molecular concentrations.

Figure 7.7 shows an IR image of the plume taken by the Indigo Merlin camera installed on the helicopter operated by NRL. This camera operates in the 3-5 μm band, and the image was captured at a distance from the ship of 72 m.

Figure 7.7 IR image taken by NRL with the Indigo Merlin camera installed on helicopter. The opaque, yellow circle embedded in the image represents the size of the FTIR Spectroradiometer's field of view, while the brighter square represents the estimated size of the area used in our plume model, SIMVEX run 23B

This close-up image shows more details of the plume than IR images from the shore station. The image is not taken at the same time as the plume measurement in run 23B, but the conditions should be comparable. As already mentioned, the analysis of individual spectra indicates that the major contribution to the total radiance originates from the area close to the stack outlet. Based on the image in Figure 7.7 we decided to use a square with size 0.7 × 0.7 m as the area of the plume in our model. Assuming that the thickness of the plume is comparable with the width, we also chose to use a thickness of 0.7 m in the model.

7.2.3 Comparison of modelled and measured plume

Using the above simplifications, the remaining unknowns are the plume temperature and the molecular concentrations. The contribution to the spectral radiance from a specific, single molecule may be modelled by FASCODE calculations, which uses data from the HITRAN database. This way it is possible to identify spectral regions where the radiance is dominated by emission from a single molecule. The total plume radiance may also be modelled when inputting appropriate temperature and concentration values for all contributing molecules. If

the model is correct, the contrast should be equal to the contrast given by the difference between the measured plume and background when evaluated according to equation (2.41). The impact on the spectral radiance may be studied by varying the input parameters.

The program we have developed at FFI for plume spectrum analysis partly automates the comparison of a modelled and a measured spectrum. This program calculates the contrast between a plume and the background at an observer's position according to equation (2.41). To obtain a quantitative measure of how well the modelled plume fits the measured spectrum, the program computes the variance of the difference between the measured and modelled contrast spectra. The calculation is sensitive to noise, and due to the noise, the variance will never be zero. But the best fit between the model and the measurement occurs when the variance reaches its minimum value. By calculating the variance for different values of temperature and molecular concentration it is possible to find the combination giving the best fit.

7.2.4 Estimate of plume temperature and molecular concentrations

The best way to ensure a reliable result is to select a spectral region with high signal to noise ratio, where a single molecule dominates the radiance. From Figure 7.3 and Figure 7.4 we assumed that the region 2380-2400 cm^{-1} might possibly give a reliable result. This spectral region has the best signal to noise ratio, and we know that the distinct line structure is caused by emission from CO_2. The calculated variance as a function of temperature and concentration is shown as a contour plot in Figure 7.8. The plot shows that the variance has its minimum value when the temperature is close to 250°C and the concentration of CO_2, given as partial pressure, is close to 30 mb (or 3 % by volume).

The temperature measured in the principle stack outlet (named MPDE A) by the Davis gas analyzer was 328°C, and the concentration of CO_2 was 4.43%. Since the exhaust gas is mixed with air when it leaves the stack outlet, the values obtained from Figure 7.8 seem reasonable. However, the contour plot in Figure 7.8 indicates that the calculated variance forms a rather "long, flat valley". If the concentration of CO_2 is reduced to 2 % or increased to 4 %, a temperature change of a few degrees will yield a spectral radiance not deviating much from the best fit. To verify the result we tried to do similar calculations in other spectral regions, also including other molecules. Unfortunately the signal to noise ratio of the measured plume is too low to give reliable results in other spectral regions. The best verification would probably have been to use a spectrum in the 8-12 μm band measured under similar conditions, but as Figure 7.6 showed, poor signal to noise ratio made that spectrum unusable.

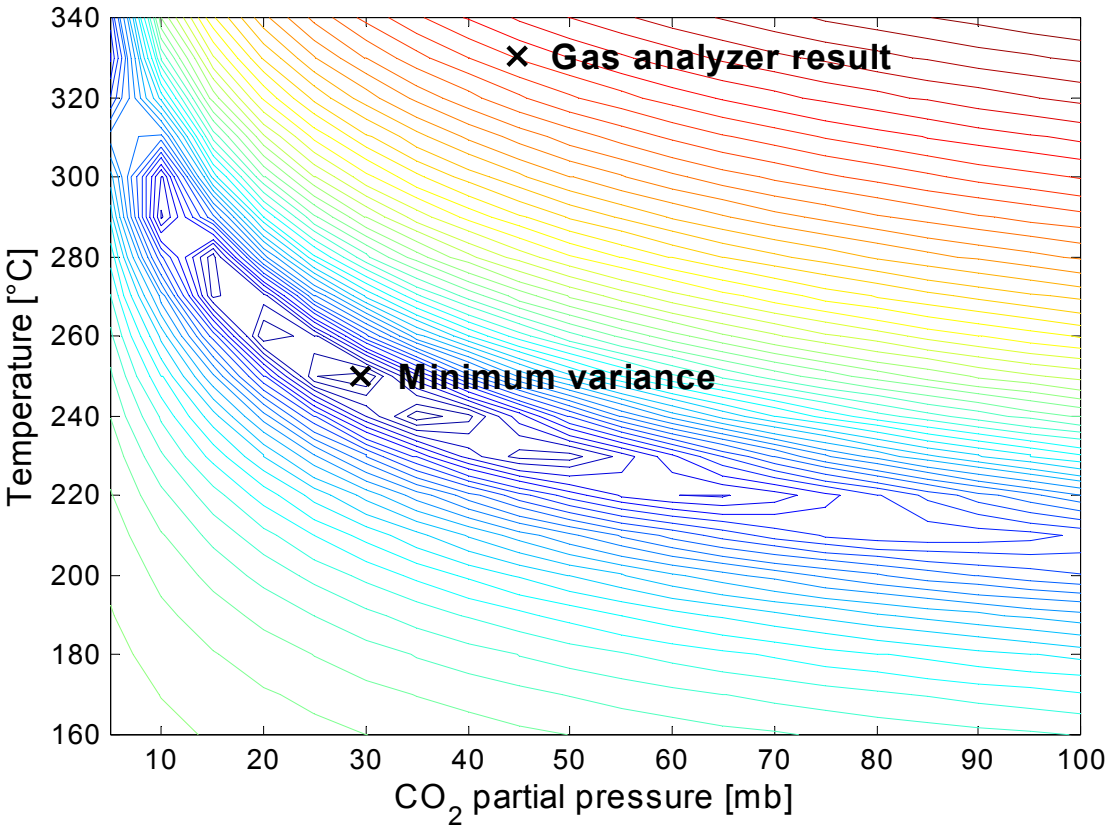

Figure 7.8 *Computed variances between modelled and measured spectra as function of molecular concentration and temperature*

In addition to the contour plot option described above, our program has an option using a Simplex search to find the optimal combination of temperature and molecular concentration, normally a much faster algorithm. We found this option unreliable to use on this spectrum, since the Simplex search often ended up in secondary minimum combinations. However, the Simplex search option seemed more reliable when keeping one of the parameters constant, and performing the search with only one unknown parameter. We have used this option to estimate the concentrations of all molecules contributing to the signature in Figure 7.3, assuming that the temperature we selected from Figure 7.8 (250°C) is representative for all emitting molecules. Table 7.1 shows the estimated molecular concentrations of H_2O, CO_2, CO and NO (given as partial pressures), as well as the spectral regions used for each molecule.

Molecule	Spectral region [cm^{-1}]	Estimated partial pressure [mb]
H_2O	1973 - 2005	36.4
CO_2	2380 - 2400	28.0
CO	2150 - 2200	0.0428
NO	1895 - 1945	0.721

Table 7.1 *Estimated partial pressures for the plume from CFAV Quest assuming the plume temperature is 250°C*

The gas analyzer result for the NO molecule for run 23B was 1208 ppm (1.2 mb). Our FTIR estimate seems reasonable compared with this number, taking the mixing with air into account. For the CO molecule the gas analyzer result was 0 % for this run (and most other runs). Probably the sensor did not work properly, or its sensitivity was too low for this purpose. The gas analyzer did not have any sensor to measure H_2O concentration.

7.3 Simulations using the plume model

7.3.1 Simulation of the measured spectrum

In this section we compare measured and simulated contrast from the plume observed against a sea background. All spectra presented are converted to apparent radiant intensity contrast (i.e $W/(sr\ cm^{-1})$), using the area given by the spectroradiometer's field of view at the distance to the plume for the measurements, and the area estimated in section 7.2.2 for the simulations. A multiplication of equation (2.34) by $\Omega_s x_t^2$, taking into account the definition of ω in equation (2.31), shows that these different conversions of measured and simulated plume radiance contrasts give comparable radiant intensity contrasts. The main reason for this conversion to radiant intensity contrast is to facilitate a comparison between our results and NRL determined plume radiant intensity contrast using IR cameras; described in section 7.3.3.

In Figure 7.9 the measured spectral radiant intensity contrast between the plume and the sea background in run 23B is plotted. Figure 7.10 shows the estimated contribution from each molecule to the total spectral radiant intensity contrast, using the calculated concentrations in Table 7.1 to model the plume radiant intensity contrast as observed at the shore station position. Figure 7.11 to Figure 7.14 show close-ups of the measured and modelled spectra in two spectral regions.

We see that there is a good fit between the measured and the modelled plume when disregarding the noise in the measured spectrum. Due to the uncertainties in the measured plume spectra and the modelling, the temperature and concentrations found by our method are not necessarily the correct values. However, the calculated values may be used to model the plume, since the radiant intensity from the modelled plume is close to the measured radiant intensity.

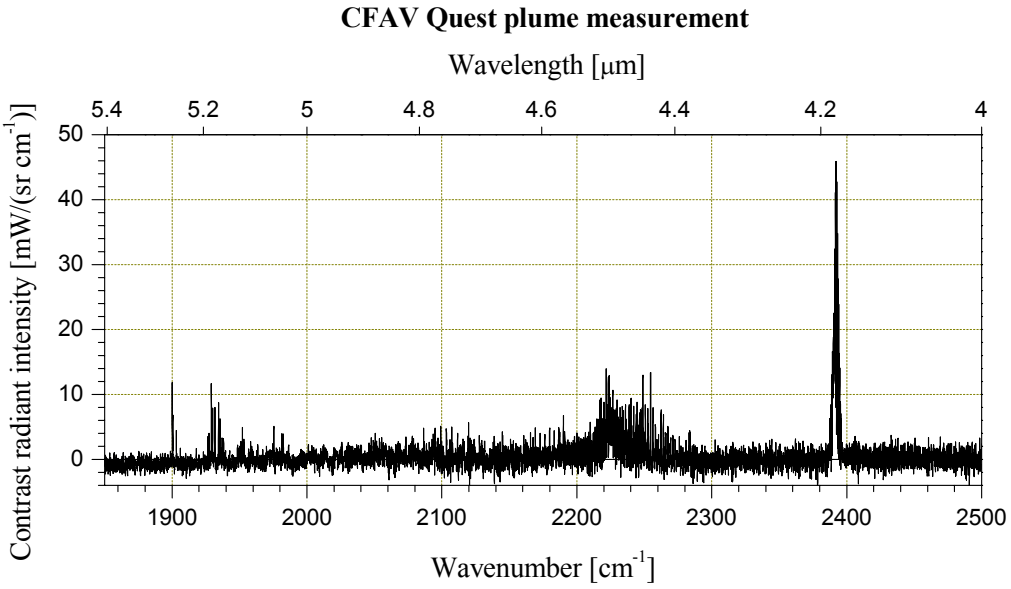

Figure 7.9 Measured contrast between the plume and the sea background with the InSb detector, SIMVEX run 23B, second part, resolution 0.2 cm^{-1}

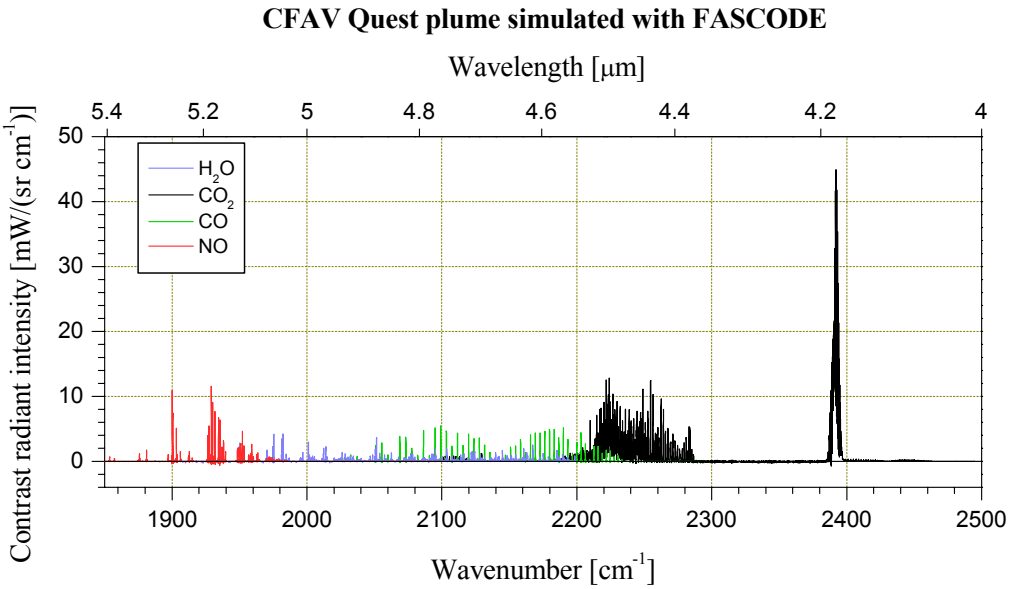

Figure 7.10 Simulated contrast between the plume and the sea background at distance 1 km, showing the simulated contributions from different molecules in different colours

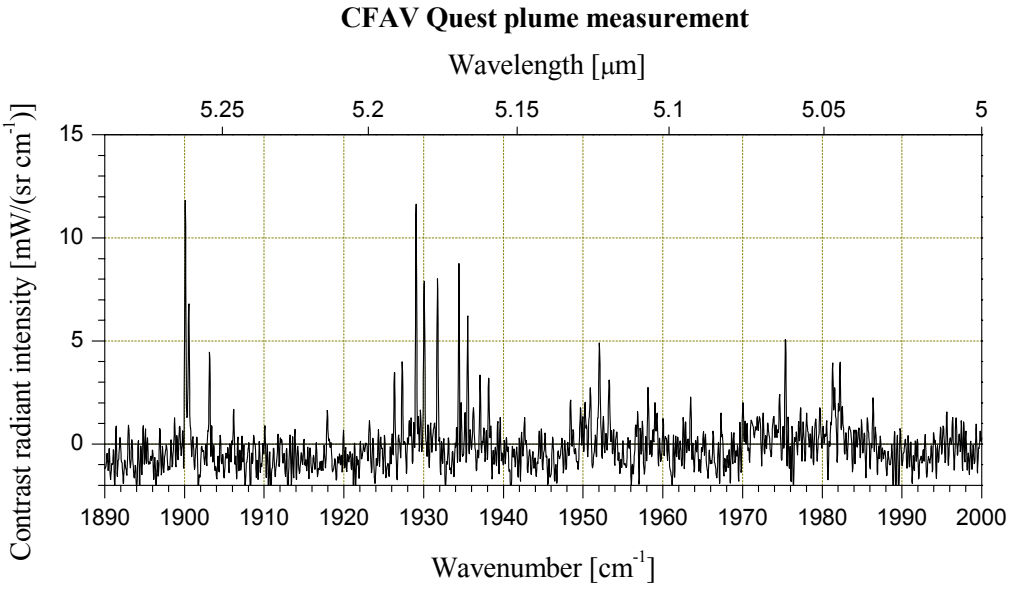

Figure 7.11 Measured contrast between the plume and the sea background with the InSb detector, SIMVEX run 23B, second part, resolution 0.2 cm^{-1}

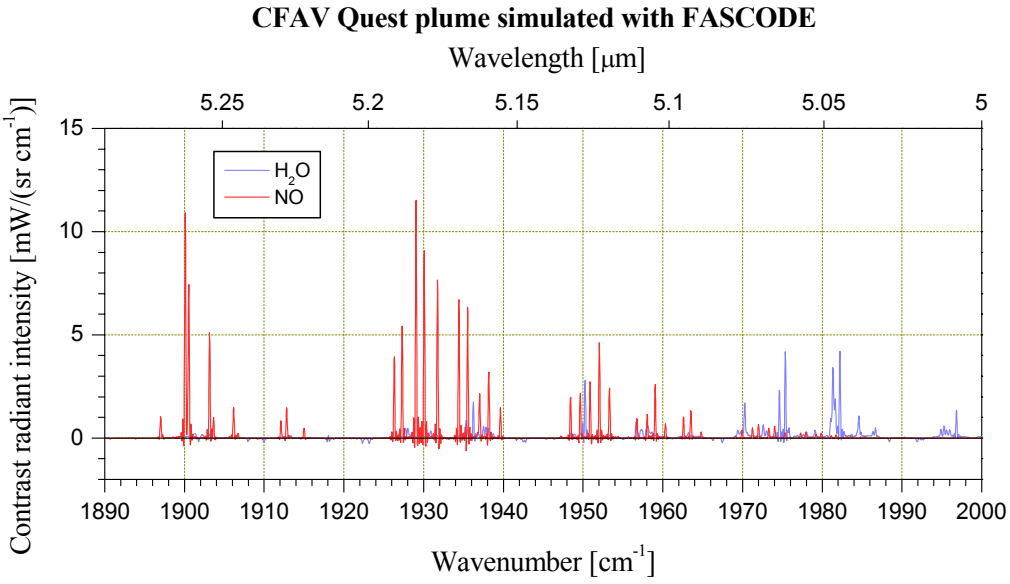

Figure 7.12 Simulated contrast between the plume and the sea background, showing the contributions from H_2O and NO in different colours

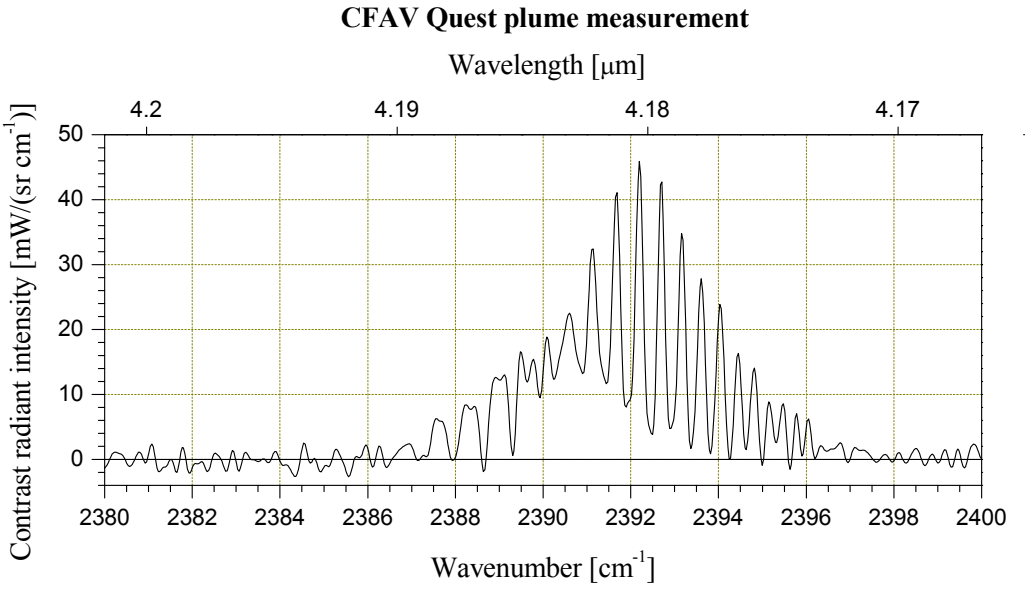

Figure 7.13 Measured contrast between the plume and the sea background with the InSb detector, SIMVEX run 23B, second part, resolution 0.2 cm^{-1}

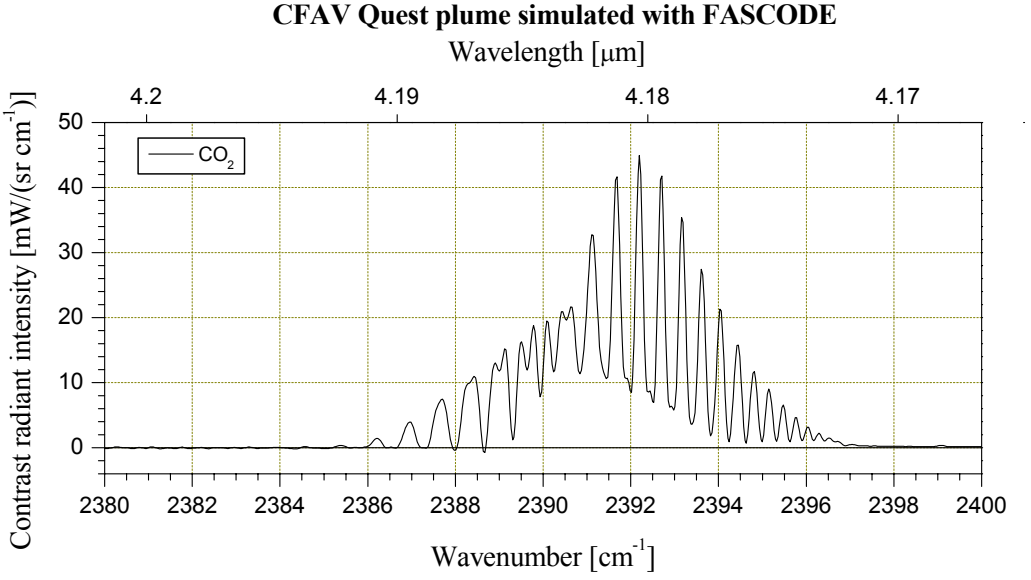

Figure 7.14 Simulated contrast between the plume and the sea background, showing the contribution from CO_2

7.3.2 Simulation of the measured scenario for the 8-12 μm band

We would like to use the plume model presented in the previous section to estimate the plume radiance in the 8-12 μm band, and at other ranges.

In Figure 7.15 the measured spectral radiant intensity contrast between the plume and the sea background in run 25 is plotted. Figure 7.16 shows the modelled contribution from H_2O and CO_2, to the total apparent radiant intensity contrast from the plume observed at a range of 1 km.

The CO and NO molecules are omitted, as they do not have any significant emission lines in the plotted spectral region. On the other hand, other molecules, for instance SO_2, may contribute to the signature. Since the concentration of SO_2 is too low to be identified from the 3-5 μm spectra, the concentration of SO_2, and thus the relative contribution from this molecule is unknown. The relative contribution from this molecule is much higher in the 8-12 μm band than the 3-5 μm band. But we have not included this molecule in the model, since the concentration is unknown.

Since our plume model is based upon uncertain temperature and concentration values found from the 3-5 μm band spectrum, the modelled 8-12 μm band radiance is not expected to fit the measured radiance as well as Figure 7.11 to Figure 7.14. But Figure 7.16 might explain why it is difficult to identify the plume contribution in the CMT measurement presented in Figure 7.15. The signal level of the strongest emission lines in the modelled plume radiant intensity only reach the same level as the noise level of CMT measurement. However, if we take a close look at Figure 7.15, it is possible to recognize some of the strongest lines in Figure 7.16. We also observe an offset level in Figure 7.15. A part of this level probably represents the contribution from soot. However, due to the manual aiming of the instrument, the hot stack outlet could be inside the field of view in parts of the measurement. Thus we will not use Figure 7.15 to estimate the soot contribution.

7.3.3 Plume simulation compared to NRL short range measurements

In some of the SIMVEX runs the ship plume was measured at short distance by IR cameras operated from helicopter by NRL. We will now apply our model to estimate the apparent spectral radiant intensity contrast from the plume at the same distance as the helicopter measurements. Figure 7.17 and Figure 7.18 show the calculated contributions from modelled molecules in the 3-5 μm and 8-12 μm bands, at distances 72 m and 88 m, respectively. The figures show that the apparent radiant intensity contrast has increased a lot at these short distances due to better atmospheric transmittance. In addition, we observe a significant change in spectral distribution of the radiant intensity.

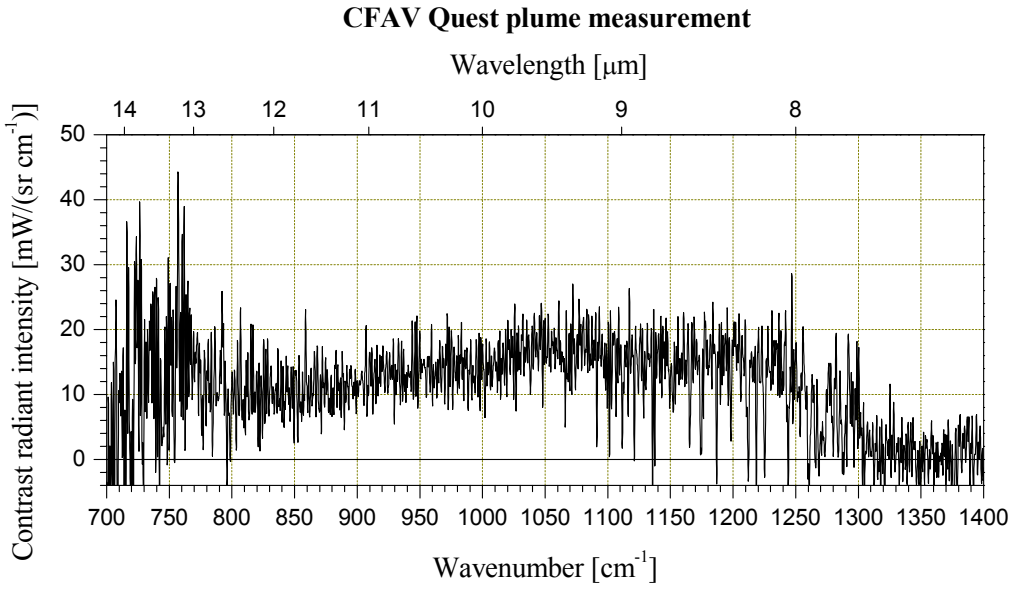

Figure 7.15 Measured contrast between the plume and the sea background with the CMT detector, SIMVEX run 25, second part, resolution 0.5 cm^{-1}

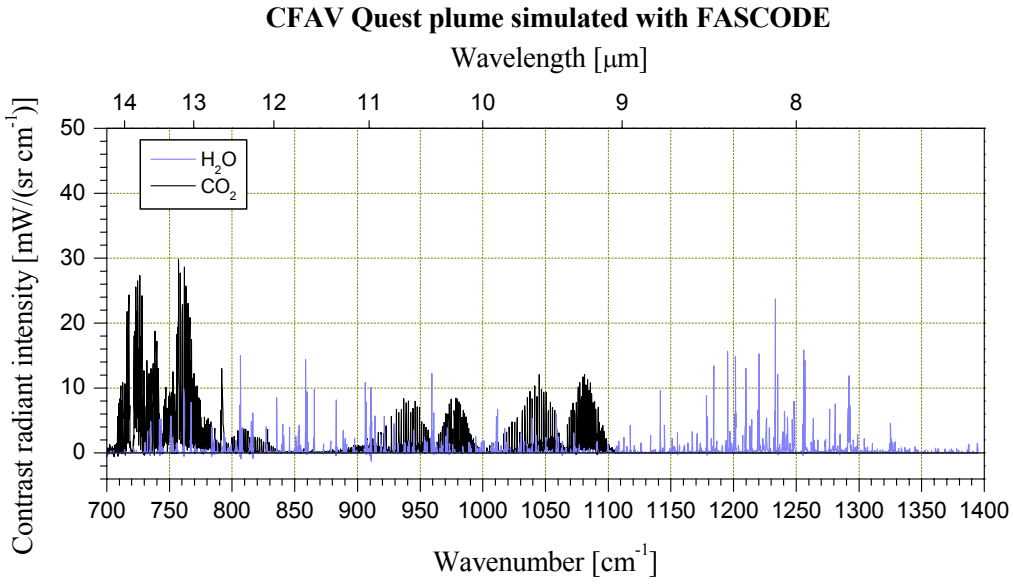

Figure 7.16 Simulated contrast between the plume and the sea background at distance 1 km, showing the contributions from H_2O and CO_2 in different colours

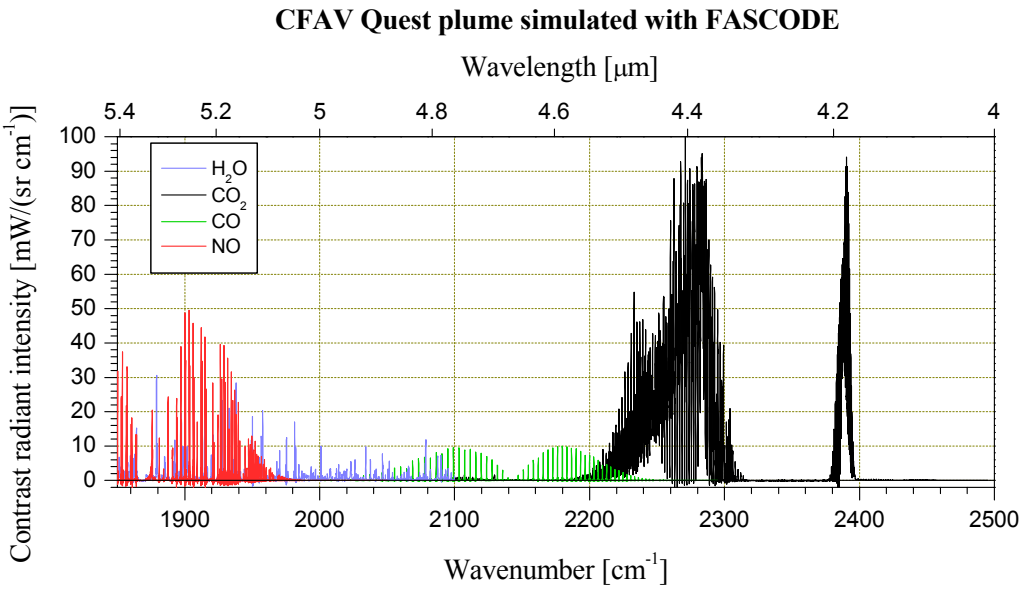

Figure 7.17 Simulated contrast between the plume and the sea background at the distance measured by the NRL helicopter (72 m), showing the simulated contributions from different molecules in different colours

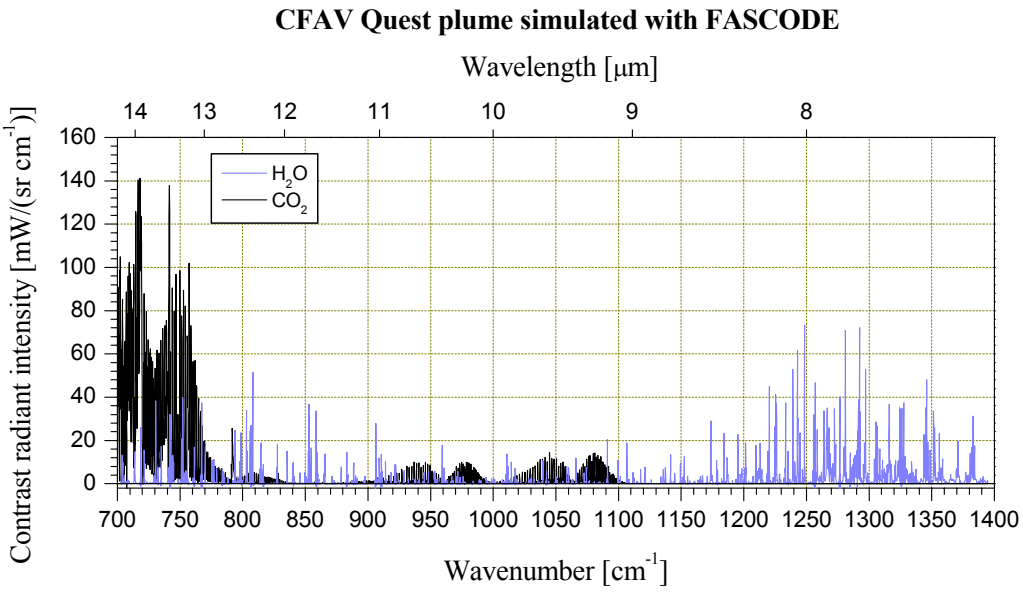

Figure 7.18 Simulated contrast between the plume and the sea background at the distance measured by the NRL helicopter (88 m), showing the simulated contributions from different molecules in different colours

To compare these spectra with the radiant intensity contrast obtained by NRL, we multiply the spectra with the relative spectral response of the cameras. This operation removes the contributions in Figure 7.17 and Figure 7.18 outside the spectral range of the cameras. By integrating the results, we get an estimate for the plume's radiant intensity in the two bands, similar to the method described in section 2.3 in (3). The results are 2.8 W/sr for the 3-5 μm band, and 0.45 W/sr for the 8-12 μm band. The values calculated by NRL from the helicopter images were 4 W/sr for the Indigo Merlin camera covering the 3-5 μm band and 1 W/sr for the Agema camera covering the 8-12 μm band (20).

We see that our values are below NRL's values, especially the 8-12 μm band values. One reason for the deviations may be the contribution from soot, which is not included in our model. As mentioned in the previous section, we are not able to model the contribution from SO_2. As a numerical example, an SO_2 concentration of 0.01 % would increase our predicted radiant intensity with 15 % in the spectral band covered by NRL's Agema camera. Further, our simplified model with constant temperature and constant molecular concentrations within a fixed area, may introduce errors. Finally, we know that there are fluctuations in the plume intensity, and as mentioned in the introduction of this chapter, the precision of our plume measurements are lower than other measurements.

7.3.4 Simulation of the plume at long distance

To study the influence of the atmosphere further, we have also calculated the plume apparent spectral radiant intensity contrast at longer distances. We have made the same calculations as above using our model at a distance of 3 km and 10 km. Figure 7.19 and Figure 7.20 show the calculated contributions from all the included molecules in the 3-5 μm and 8-12 μm bands, respectively, at a distance of 10 km. The total apparent radiant intensity contrast is strongly reduced at long distances, and again the figures show a change in spectral distribution compared to the measured plume at 1 km.

Figure 7.10 and Figure 7.16 to Figure 7.20 have shown that the relative contribution from each molecule to the total radiant intensity is dependent on the distance. Table 7.2 shows the integrated radiant intensity contrast from the molecules we have modelled at the selected distances for the most important part of the 3-5 μm band. The corresponding results for the 8-12 μm band are shown in Table 7.3. The results in Table 7.2 are plotted in Figure 7.21 with logarithmic scale on both axes.

The results show that for the given meteorological conditions, CO_2 is the major contributor to the radiant intensity at all calculated distances in the 3-5 μm band, followed by H_2O. However, the relative contribution from CO_2 radiation is reduced from 80.9 % to 67.7 % when the distance is increased from 72 m to 10 km. The relative contribution from H_2O increases from 10.3 % to 20.3 %. Similarly the relative contribution form CO increases strongly, and the relative contribution from NO decreases strongly, at long distances. In the 8-12 μm band ,

where only H_2O and CO_2 are modelled, the signature is dominated by the H_2O contribution at short distances, and by the CO_2 contribution at long distances.

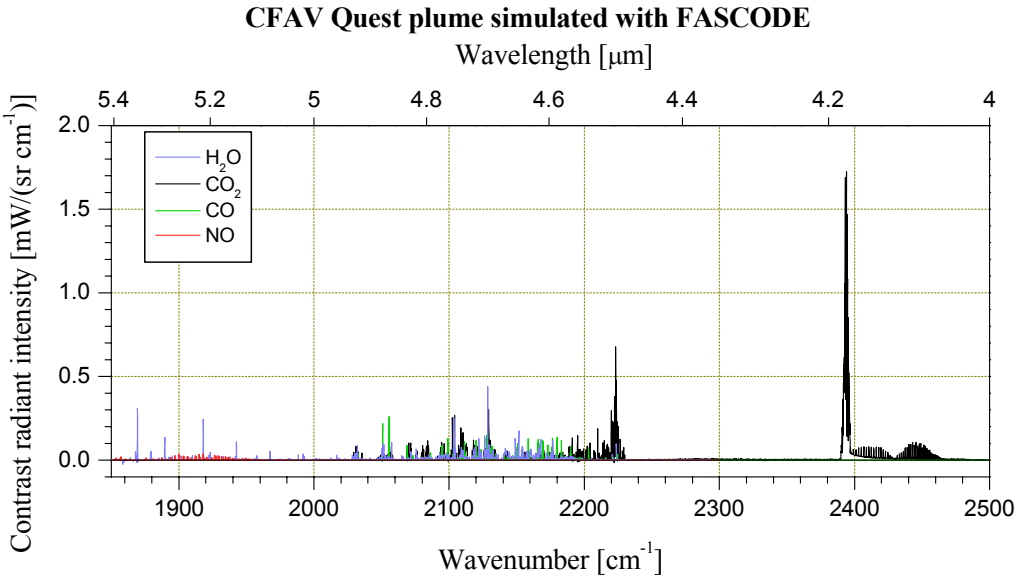

Figure 7.19 Simulated contrast between the plume and the sea background at a distance of 10 km, showing the simulated contributions from different molecules in different colours

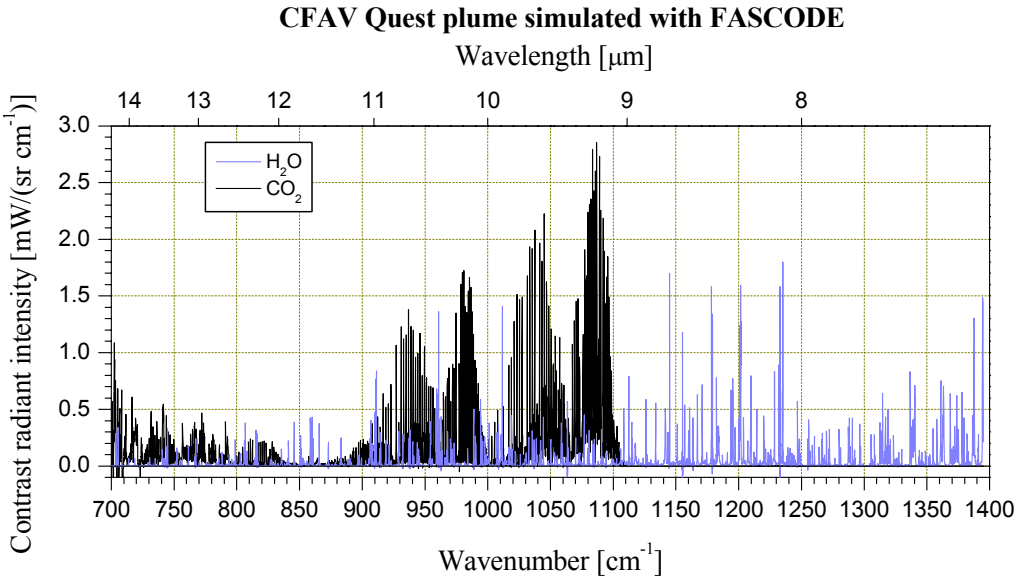

Figure 7.20 Simulated contrast between the plume and the sea background at a distance of 10 km, showing the simulated contributions from different molecules in different colours

Distance [km]	H_2O contribution		CO_2 contribution		CO contribution		NO contribution		Total radiant intensity contrast [W/sr]
	Abso-lute [W/sr]	Rela-tive	Abso-lute [W/sr]	Rela-tive	Abso-lute [W/sr]	Rela-tive	Abso-lute [W/sr]	Rela-tive	
0.072	0.354	10.3 %	2.778	80.9 %	0.059	1.7 %	0.245	7.1 %	3.436
1	0.054	13.9 %	0.280	72.7 %	0.030	7.8 %	0.021	5.5 %	0.385
3	0.017	15.0 %	0.085	74.0 %	0.011	9.8 %	0.0014	1.2 %	0.114
10	0.003	20.3 %	0.010	67.7 %	0.0016	10.8 %	0.0002	1.2 %	0.015

Table 7.2 *Absolute and relative contribution to the total radiant intensity of the plume from modelled molecules at different distances. The modelled spectra are integrated from 1850-2500 cm^{-1} (4-5.4 μm)*

Distance [km]	H_2O contribution		CO_2 contribution		Total radiant intensity contrast [W/sr]
	Absolute [W/sr]	Relative	Absolute [W/sr]	Relative	
0.072	0.412	63.1 %	0.241	36.9 %	0.653
1	0.166	45.2 %	0.201	54.8 %	0.367
3	0.081	36.3 %	0.142	63.7 %	0.223
10	0.019	28.1 %	0.048	71.9 %	0.067

Table 7.3 *Absolute and relative contribution to the total radiant intensity of the plume in the 8-12 μm band from modelled molecules at different distances. The modelled spectra are integrated from 833-1250 cm^{-1} (8-12 μm)*

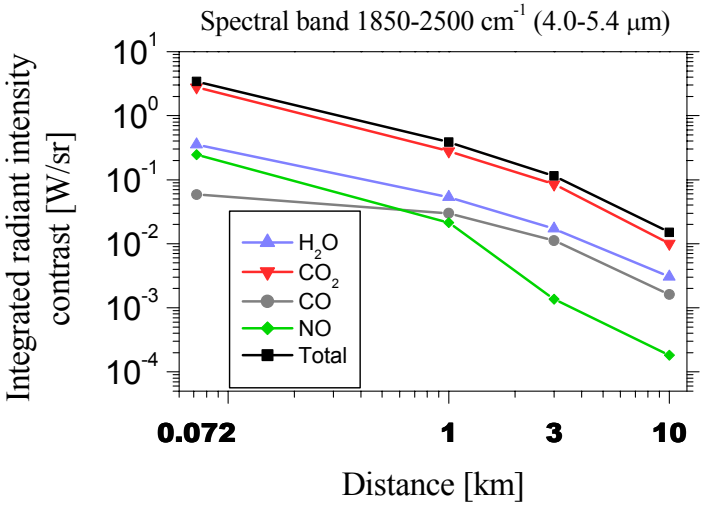

Figure 7.21 *Integrated radiant intensity contrast contribution from different molecules as function of distance*

If the plume model is applied at other speeds, the relative contributions from included molecules could change, since it might be significant changes in molecular composition of the combustion gas when the engine settings and the ship speed are changed.

The results shown in Table 7.2, Table 7.3 and Figure 7.21 are based upon the atmospheric transmittance related to the meteorological conditions in SIMVEX run 23B and the ship engine settings during this run. The spectral transmittance is quite different under other meteorological conditions, which affects the contribution from the molecules. Another engine setting will change the molecular composition of the combustion gases The results from our plume simulations show that the selection of molecules to be included in a plume model, may depend on the conditions under which the model will be applied.

7.3.5 Importance of using high spectral resolution in radiance modelling

To illustrate the importance of using high spectral resolution, when measured results from targets with rapid spectral variations in radiance are used for modelling purposes, we show an example using our plume model. Figure 7.22 shows two curves.

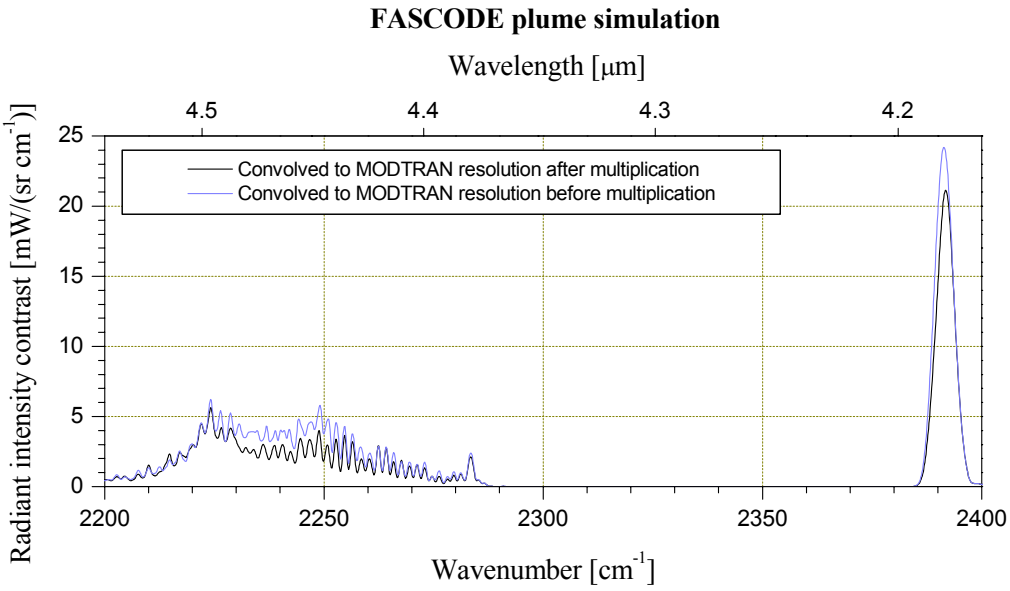

Figure 7.22 Demonstration of two different methods for simulation of plume radiance with FASCODE

The black curve shows the results in Figure 7.10 smoothed to a spectral resolution of 1 cm^{-1} (MODTRAN resolution) by convolution with a slit function having 1 cm^{-1} Full Width Half Maximum. Thus for the black curve target radiance and atmospheric transmittance, both at

high spectral resolution, are multiplied before the resolution is reduced by convolution with the slit function.

The blue curve shows the result when the target radiance and the atmospheric transmittance separately are convolved with the slit function, and then multiplied. This is equivalent to using low spectral resolution models (based on low resolution measurements), for target radiance and atmospheric transmittance in computer models such as ShipIR

The two curves do not agree very well. When integrating the two curves, the result for the blue curve is 23 % greater than the result for the black curve. If the resolution is further reduced, this difference will increase. The result tells us that it is difficult to establish a model of the plume based upon measurements, if the spectral features of the plume are not resolved. Even if a correct model of the plume radiance exists, a calculation of apparent radiance at an observer's location may be wrong, if the resolution is too low in the software used to calculate atmospheric transmittance.

The resolution of the plume model in ShipIR (50 cm^{-1}) is low compared to the rapid spectral variations in a real plume, as shown in this chapter. A consequence of this property is that even if ShipIR predicts correct radiance at a specific distance and meteorological condition, the low resolution of the plume model will be a source of error, when using ShipIR to predict the radiance of the plume at a different distance, and under different meteorological conditions.

Based on the results from this trial we recommend that spectral measurements of ship plumes in future field trials are carried out with as high resolution as possible. We will also recommend that the distance between the ship and the instrument should be as short as possible, for two reasons. First, the best signal to noise ratio is achieved when the plume fills the field of view. Second, the possibility for estimating correct radiance in the target plane is best when the atmospheric transmittance between ship and instrument is high. This would make it possible to obtain a plume model in ShipIR with a higher resolution. The spectral resolution in the current plume model is far too low.

8 CONCLUSIONS

FFI participated in the SIMVEX field trial arranged by NATO RTO/SET/TG16 at Osborne Head near Halifax, Canada in September 2001. Large amounts of data were collected with different instrumentation. Results from the analysis of the data acquired by the IR cameras and our meteorological equipment have been presented in (3). In this report we have presented and analyzed data collected with the Bomem DA5 FTIR Spectroradiometer. The instrument had been in use for 4 years when SIMVEX was arranged. During this time we have developed procedures to improve the absolute precision of calibrated spectra, and demonstrated good results from this work.

The measurements of IR radiation from the surface of CFAV Quest have shown that the spectral radiance is close to a blackbody at night time. The same property is observed for shaded parts of the ship at day time. The apparent radiance at the observer's location is influenced by atmospheric absorption and path emission. The contribution from sky and sea foreground radiance seems to affect the total radiance very little, although we know that there is some reflection from the surface.

When the ship surface is illuminated by sun, we observe different impacts on the infrared signature of the surface. The ship is heated, so that the surface temperature and the radiance from the ship increase. A contribution to the signature from reflected sunlight is also observed. In the 8-12 μm band, this contribution is too small to be separated from the radiation from the surface. Also in the 3-5 μm band, the contribution is rather low at low wavenumbers, but increases with wavenumber. In the spectral window around 2-2.5 μm the emission from the ship surface is well below the instrument's noise level, but the spectral radiance caused by reflected sunlight is clearly visible. When the geometry is such that we get specular reflection of sunlight from the surface, the total radiance increases strongly. Especially in the high wavenumber region of the 3-5 μm band this contribution dominates the total signature. We did not perform measurements of any scenario with specular sun reflection in the 8-12 μm band.

The temperature of the funnel gets higher than the hull of the ship due to heat transfer from the hot exhaust gases. When the ship is not sun illuminated the temperature difference between the cooler parts of the funnel and the hull is rather small. When the ship is sun illuminated, the temperature of the funnel, which is painted with yellow colour, increases more than the hull, due to absorption of sunlight. However, the diffuse reflection of sunlight in the infrared region from 2-5 μm is only slightly lower from the funnel than from the hull.

Apparent temperatures calculated from measured spectra have been compared with ShipIR temperature predictions and thermocouple measurements on the ship surface. The results indicate that ShipIR underpredicts the surface temperature when the sky is clear at night time, while the temperatures are overpredicted for surfaces heated by the sun.

Measurements of the sky show that clear sky radiates close to a blackbody function just above the horizon, but the radiance decreases rapidly with increasing angle, and the spectral radiance contains distinct line structures due to molecular emission lines. Measurements of the sea background show that the contribution from reflected sky radiance is significant. The spectral characteristics show the same line structures as sky radiance spectra. The total radiance changes little when the pitch angle is between -4° and -1°, and then increases gradually up to the horizon.

ShipIR predictions of sky and sea backgrounds have shown that ShipIR predicts a clear sky background very well, if the meteorological conditions as function of altitude are known, and input to the model. But the predicted sky radiance is sensitive to variations in meteorological parameters. Our simulations have also shown that ShipIR underpredicts the sea background

radiance when the sky is clear. This effect is observed both in the 8-12 μm and 3-5 μm bands, but our results for the 3-5 μm band are more uncertain, due to lack of correct meteorological data at higher altitudes when the measurements were performed.

The plume from CFAV Quest was also measured with the spectroradiometer. At the actual distance the size of the plume was too small to make high quality measurements, but we managed to characterize the spectral signature in the 3-5 μm band. The following molecules have been clearly identified in the measured plume spectra, H_2O, CO_2, CO and NO. From the measured spectrum it is difficult to calculate exact values for temperature and molecular concentration of combustion gases, but the results we obtained seem reasonable compared to data from the gas analyzer mounted in the stack outlet. We have shown that when applying this combination of parameter values, the apparent spectral radiance from a modelled plume is very close to the measured spectrum. Also when using the model to predict measured signature of the plume observed by NRL from helicopter mounted IR cameras, the results agree reasonably well. The model also shows that when observing a plume, the relative contribution to the total signature from the different molecules is strongly dependent on atmospheric transmittance, which varies with distance and meteorological conditions.

Results from the IR cameras belonging to the different nations participating in the SIMVEX trial are compared by converting the pixel values of the images to equivalent temperature. For cameras with different optical bandwidths this method will only give comparable results when the spectral radiance from objects in the image is close to blackbody functions. The spectral measurements have shown that this condition is fulfilled for the ship surface at night time, for shaded parts of the ship at day time, and for the sky background just above the horizon. This condition also seems to be fulfilled in the 8-12 μm band when observing diffusely reflected sunlight from the ship surface, since the contribution from diffusely reflected sunlight is observed to be very small. Thus the different IR cameras should give comparable results when analyzing the objects mentioned.

The spectral measurements show that radiance from the sea and sky backgrounds (except just above the horizon) deviates from a blackbody. The same applies to the sun illuminated surface in the 3-5 μm band. For these objects one can only expect to get the same results from an equivalent temperature calculation if the IR cameras have identical optical bandwidths. The same precaution applies to comparison of radiance contrasts in different images, when the sea background is used for contrast calculation. When comparing contrasts in IR camera images with ShipIR predictions, the results are expected to have the best agreement if the area just above the horizon is used as background reference, since the ShipIR prediction seems to be quite correct here.

Although there are uncertainties in some results, we are generally satisfied with our results from the spectral measurements during the SIMVEX trial, and we believe that most of the data have high quality. The trial was very well organized by Canada as hosting nation, and there was close collaboration between participating nations in the preparation process through the

NATO RTO/SET/TG16 work group. These factors, in addition to data exchange during the post-processing phase, have been important in achieving these results. We hope that the results presented in this report will increase the knowledge about spectral emission and reflection properties of ship surface materials, sea and sky backgrounds, and combustions gases in the infrared region. We also hope that the results may be useful for future work on upgrading and improving the ShipIR/NTCS signature model.

References

(1) Vaitekunas D A, Alexan K, Lawrence O E, Reid F (1996): SHIPIR/NTCS: a naval ship infrared signature countermeasure threat engagement simulator, *SPIE* **2744**, 411-424.

(2) Stark E, Brendhagen E, Lippert E, Bingen E (2000): Spectral IR measurements of ships and decoys by FFI during NATO SWG/4 EW Trial 1999, FFI/RAPPORT-2000/02789, Forsvarets forskningsinstitutt, (Confidential)

(3) Stark E, Heen L T, Wikan K (2002): SIMVEX 2001 Trial - Radiant intensity contrast, FFI/RAPPORT-2002/02568, Forsvarets forskningsinstitutt

(4) Bell R J (1972): Introductory Fourier Transform Spectroscopy, Academic Press.

(5) Selnes O (1976): Fourier Transform Spektroskopi (FTS), en dokumentasjon av programmer til spektrometeret PFS201A, Teknisk Notat E-816, Forsvarets forskningsinstitutt (In Norwegian)

(6) Lachance R L, Villemaire A, Rochette L (1998): Correction of the non-linearity of FT remote sensing instruments, Fourth Workshop on Infrared Measurements by FTIR, Bomem Inc, Québec, Canada.

(7) Jeseck P, Camy-Peyret C, Payan S, Hawat T (1998): Detector nonlinearity correction scheme for the LPMA balloonborne Fourier transform spectrometer, *Applied Optics* **37**, 27, 6544-6549.

(8) Lippert E (2002): Private communication.

(9) Revercomb H E, Buijs H, Howell H B, LaPorte D D, Smith W L, Sromovsky L A (1988): Radiometric calibration of IR Fourier transform spectrometers: solution to a problem with the High-Resolution Interferometer Sounder, *Applied Optics* **27**, 15, 3210-3218.

(10) Mertz L (1967): Auxiliary computation for Fourier spectrometry, *Infrared Physics* **7**, 17-23.

(11) (1999): PCDA software user's guide, revision 1.3, ABB Bomem Inc, Québec, Canada.

(12) Smith H J P, Dube D J, Gardner M E, Clough S A, Kneizys F X, Rothman L S (1978): FASCODE - Fast Atmospheric Signature Code (Spectral transmittance and radiance), Air Force Geophysics Laboratory Technical Report AFGL-TR-78-0081, Hanscom AFB, MA, USA.

(13) Anderson G P (1996): The Modtran 2/3 Report and LOWTRAN7 Model, F19628-91-C-0132, Air Force Research Laboratory, USA.

(14) Rothman L S et al (1998): The HITRAN Molecular Spectroscopic Database and HAWKS (HITRAN Atmospheric Workstation): 1996 Edition, *Journal of Quantitative Spectroscopy and Radiative Transfer* **60**, 665-710.

(15) Bingen E (2002): Private communication.

(16) Stark E, Steenfeldt-Foss P, Brendhagen E, Almklov B (2001): SIMVEX 2001 Trial - FFI test plan for infrared measurements, FFI/NOTAT-2001/04023, Forsvarets forskningsinstitutt

(17) Almklov B (2003): Bruk av "Matrox 4sight" som hjelpemiddel ved opptak med FTIR spektrometer, (Under preparation), FFI/NOTAT-2003/00554, Forsvarets forskningsinstitutt (In Norwegian).

(18) Vaitekunas D (2001): Davis instrumentation plan for the SIMVEX Trial, A117-001 Rev 1, W. R. Davis Engineering Ltd, Ottawa, Canada.

(19) Vaitekunas D (2002): Preliminary Assessment of the SIMVEX Database, Presentation at the NATO ShipIR/NTCS Workshop, Québec, Canada, 8 Oct 2002.

(20) Fraedrich D (2002): Private communication.

(21) Schäfer K et al (2000): Nonintrusive optical measurements of aircraft engine exhaust emissions and comparison with standard intrusive techniques, *Applied Optics* **39**, 3, 441-455.

APPENDIX

A OVERVIEW OF SIMVEX RUNS AND METEOROLOGICAL CONDITIONS

In this appendix we present an overview of the conditions for FTIR measurements performed by FFI during the SIMVEX trial. Table A.1 presents data for a selection of runs during the two series of sea and sky background measurements discussed in chapter 5. These measurements were performed by the FFI team only, and were not assigned any SIMVEX run number. The table contains the run number used by FFI, measured object, date and time, detector in use on the FTIR spectrometer, and meteorological parameters measured at the shore station. Air temperature, relative humidity, solar irradiance, wind speed and wind direction parameters are taken from the meteorological station close to the container. Absolute humidity is calculated from air temperature and relative humidity observations. Sea temperature was measured close to the shoreline. More information on the meteorological sensors is given in (3).

Tables A.2 to A.5 present the corresponding parameters for the type A, B, C and D ship runs discussed in chapter 6. The SIMVEX run number and manual observations of the cloud cover are included in these tables, as well as air temperature measured on board the ship. The D run parameters presented in Table A.5 represent the first part of the runs (before the ship turns). Table A.6 presents the conditions during the DRDC-V test panel runs.

The conditions during the plume runs discussed in chapter 7 are presented in Table A.7. The parameters presented in Table A.7 (except run 37) represent the second part of the runs (after the ship has turned).

FFI run no	***Pitch angle***	***Date and time (UTC)***		***Detector***	***Shore station meteorological data***						
					Air temp [°C]	Humidity		Solar irradi-ance [W/m^2]	Wind		Sea temp [°C]
		D	T			Rel [%]	Abs [g/m^3]		Speed [m/s]	Dir [°]	
156	Sea, -4°	16	17:33	CMT	17.1	65.4	9.5	716	9.6	197	16.1
160	Sea, -0.3°	16	17:46	CMT	17.2	68.9	10.1	697	8.2	200	16.1
162	Sky, 0°	16	17:54	CMT	17.2	69.5	10.2	685	8.8	201	16.1
166	Sky, 15°	16	18:08	CMT	17.2	68.9	10.1	660	9.4	210	16.2
275	Sea, -4°	19	21:59	InSb	17.4	39.1	5.8	32	4.1	22	16.7
281	Sea, -0.3°	19	22:20	InSb	16.0	46.2	6.3	3	2.9	6	16.7
283	Sky, 0°	19	22:29	InSb	15.5	47.3	6.3	1	3.0	1	16.7
287	Sky, 15°	19	22:45	InSb	14.8	50.9	6.4	0	3.2	0	16.7

Table A.1 Measurements of sea and sky backgrounds with the FTIR spectroradiometer. The sky was clear during these measurements

Run no		***Date and time (UTC)***		***Det***	***Shore station meteorological data***								***Ship*** air temp [°C]
					Air temp [°C]	Humidity		Solar irradi-ance [W/m^2]	Cloud cover	Wind		Sea temp [°C]	
SIM-VEX	FFI	D	T			Rel [%]	Abs [g/m^3]			Speed [m/s]	Dir [°]		
9	104	14	18:28	CMT	19.6	38.7	6.5	591	Few	5.2	308	15.2	18.2
13	128	15	18:28	InSb	16.0	56.5	7.7	616	Few	7.5	202	16.1	14.8
18	169	16	18:32	CMT	17.1	68.0	9.9	608	Few	9.6	214	16.2	16.4
31	259	19	18:29	InSb	20.5	29.9	5.3	610	Clear	3.8	13	17.3	19.2

Table A.2 SIMVEX A runs (day) measured with the FTIR spectroradiometer

Run no		***Date and time (UTC)***		***Det***	***Shore station meteorological data***								***Ship*** air temp [°C]
					Air temp [°C]	Humidity		Solar irradi-ance [W/m^2]	Cloud cover	Wind		Sea temp [°C]	
SIM-VEX	FFI	D	T			Rel [%]	Abs [g/m^3]			Speed [m/s]	Dir [°]		
8	99	14	16:52	CMT	20.8	45.5	8.2	704	Few	4.8	330	15.1	18.4
17	152	16	17:00	CMT	17.6	60.6	9.1	752	Few	9.4	204	16.1	17.0
22	196	17	17:03	InSb	17.4	68.7	10.2	562	Broken	2.1	170	16.0	16.6
29	254	18	17:02	InSb	22.0	47.7	9.3	570	Broken/ overcast	3.2	50	16.1	18.0
36	309	20	17:01	CMT	17.6	67.2	10.1	568	Broken	4.0	156	17.6	16.8

Table A.3 SIMVEX B runs (day) measured with the FTIR spectroradiometer

Run no		***Date and time (UTC)***		***Det***	***Shore station meteorological data***								***Ship*** air temp [°C]
					Air temp [°C]	Humidity		Solar irradi-ance [W/m^2]	Cloud cover	Wind		Sea temp [°C]	
SIM-VEX	FFI	D	T			Rel [%]	Abs [g/m^3]			Speed [m/s]	Dir [°]		
5	85	13	20:59	InSb	16.7	78.5	11.2	93	Broken	0.7	265	15.0	16.5
6	90	13	22:18	CMT	17.0	79.9	11.6	15	Broken	1.7	310	15.0	16.4
10	110	14	20:56	CMT	18.4	42.7	6.7	186	Scat-tered	5.6	327	15.1	17.8
14	134	15	21:03	InSb	15.6	59.5	7.9	192	Few	7.0	207	16.0	16.5
19	175	16	21:02	CMT	17.1	70.4	10.2	185	Clear	7.0	226	16.1	18.2
24	219	17	21:02	CMT	17.3	80.2	11.8	149	Broken	4.0	198	16.6	17.3
32	265	19	20:47	InSb	19.3	34.2	5.7	220	Clear	4.1	22	17.3	19.0
38	321	20	21:00	CMT	16.3	72.0	10.0	99	Broken/ overcast	5.4	154	17.9	16.5

Table A.4 SIMVEX C runs (day) measured with the FTIR spectroradiometer

Run no		***Date and time (UTC)***		***Det***	***Shore station meteorological data***								***Ship*** air temp [°C]
					Air temp [°C]	Humidity		Solar irradi-ance [W/m^2]	Cloud cover	Wind		Sea temp [°C]	
SIM-VEX	FFI	D	T			Rel [%]	Abs [g/m^3]			Speed [m/s]	Dir [°]		
7	93	13	23:24	CMT	15.7	79.4	10.6	0	Broken	2.5	330	14.9	16.5
11	116	14	23:26	CMT	14.5	58.7	7.3	0	Broken	2.9	350	15.3	15.4
12	122	15	00:14	InSb	14.1	53.9	6.5	0	Broken	3.1	355	15.4	14.8
15	140	15	23:24	InSb	14.6	66.7	8.3	0	Few	3.7	233	15.9	15.2
16	146	16	00:12	CMT	13.6	73.5	8.6	0	Few	3.4	269	15.9	14.8
20	182	16	23:23	CMT	15.7	85.7	11.5	0	Few	3.6	242	16.0	16.5
21	189	17	00:10	InSb	14.9	86.8	11.1	0	Few	2.6	270	15.9	15.8
26	237	17	23:22	CMT	16.6	87.9	12.4	0	Broken	3.4	220	16.4	17.0
27	245	18	00:14	InSb	15.8	93.2	12.5	0	Broken	2.3	232	16.4	17.1
34	293	19	23:27	InSb	13.7	55.3	6.5	0	Clear	3.2	5	16.7	15.6
35	301	20	00:20	CMT	13.7	58.4	6.9	0	Clear	4.8	33	16.7	14.6
39	328	20	23:26	CMT	15.6	74.2	9.9	0	Broken/ overcast	6.2	154	17.2	16.0
40	336	21	00:22	InSb	15.5	73.1	9.7	0	Broken	6.1	148	17.1	-

Table A.5 SIMVEX D runs (night) measured with the FTIR spectroradiometer

Run no		***Date and time (UTC)***		***Det***	***Shore station meteorological data***								***Ship*** air temp [°C]
					Air temp [°C]	Humidity		Solar irradi-ance [W/m^2]	Cloud cover	Wind		Sea temp [°C]	
SIM-VEX	FFI	D	T			Rel [%]	Abs [g/m^3]			Speed [m/s]	Dir [°]		
33A	270	19	21:12	InSb	18.7	32.6	5.2	144	Clear	4.2	35	17.1	18.9
33B	271	19	21:22	InSb	18.4	35.4	5.6	116	Clear	4.3	17	17.1	18.7
33C	272	19	21:31	InSb	18.1	37.7	5.8	92	Clear	3.8	26	17.0	18.8

Table A.6 SIMVEX DRDC-V test panel runs measured with the FTIR spectroradiometer

Run no		***Date and time (UTC)***		***Det***	***Shore station meteorological data***								***Ship*** air temp [°C]
					Air temp [°C]	Humidity		Solar irradi-ance [W/m^2]	Cloud cover	Wind		Sea temp [°C]	
SIM-VEX	FFI	D	T			Rel [%]	Abs [g/m^3]			Speed [m/s]	Dir [°]		
23A	204	17	18:02	InSb	17.8	70.8	10.7	489	Broken	1.9	168	16.3	17.0
23B	208	17	18:52	InSb	18.6	72.6	11.6	418	Broken	2.4	179	16.4	17.4
23C	212	17	19:22	InSb	18.3	72.2	11.3	434	Broken	4.0	188	16.5	17.4
25	226	17	21:51	CMT	17.1	82.4	12.0	37	Broken	3.8	210	16.5	17.3
37	315	20	18:21	InSb	16.9	68.5	9.8	373	Broken	4.4	156	17.6	16.6

Table A.7 SIMVEX plume runs measured with the FTIR spectroradiometer

Table A.8 presents pressure, air temperature and absolute humidity as function of altitude, applied in the user defined profile discussed in section 5.4 to model our measurement of the sky with the CMT detector. Meteorological data from the shore station were used to specify the conditions at sea level. At altitudes from 0.6 to 10 km radiosonde data from Shearwater at 15 (UTC) on 17th September were used. Between 10 and 36 km radiosonde data from Sable Island at 0 (UTC) on 17th September were used. For all molecules except H_2O the default concentrations given by the "Midlatitude Summer" model were used.

Altitude [km]	Pressure [mb]	Temperature [°C]	Absolute humidity [g/m^3]
0.0	1010	17.0	10.000
0.6	954	14.8	5.480
0.8	925	12.8	5.870
1.5	857	7.8	4.780
2.2	788	3.6	2.660
3.0	717	4.6	1.440
4.0	626	-1.1	0.760
4.9	562	-5.3	0.250
5.8	500	-12.5	0.110
7.4	400	-25.9	0.015
8.0	372	-30.5	0.014
9.5	300	-38.7	0.012
10.2	269	-42.5	0.006
12.0	200	-56.1	0.007
14.1	143	-59.5	0.002
16.4	100	-58.3	0.001
17.5	83	-59.5	0.001
19.9	58	-56.3	0.000
22.5	39	-52.7	0.000
26.7	20	-47.9	0.001
30.0	12	-47.5	0.001
36.1	5	-35.5	0.003

Table A.8 Meteorological parameters of a user defined atmospheric profile. This profile was used to simulate the measurement of sky radiance with the CMT detector

Our measurement of the sky with the InSb detector was modelled using a modified atmospheric profile. Since none of the available radiosonde data seem to represent the conditions for the measurement well, a profile based upon the data in Table A.8 was constructed. Meteorological data from the shore station during the InSb detector measurement were used to specify the conditions at sea level. Based upon these sea level parameters and the parameters in Table A.8, the new, scaled values as presented in Table A.9, were applied up to an altitude of 1.5 km. The same parameters as presented in Table A.8 were applied above 1.5 km.

Altitude [km]	Pressure [mb]	Temperature [°C]	Absolute humidity [g/m^3]
0.0	1022	16.0	6.3
0.6	962	14.0	3.5
0.8	932	12.0	3.5
1.5	850	7.0	3.5

Table A.9 Meteorological parameters of a modified user defined atmospheric profile. This profile was applied to simulate the measurement of sky radiance with the InSb detector. The parameters presented in Table A.8 were applied above 1.5 km

B FTIR SPECTRAL RESPONSIVITY, INSTRUMENT SELF EMISSION AND LINE SHAPE FUNCTION

The FTIR spectral responsivity and instrument self emission are presented in section B.1, and the instrument line shape function is presented in section B.2. Most of the contents in this appendix is taken from (2), but is updated according to conditions during the SIMVEX trial.

B.1 FTIR spectral responsivity and instrument self emission

The FTIR spectral responsivity and instrument self emission are obtained by using two blackbodies at different temperatures (150°C and 30°C during SIMVEX). When using the CdHgTe (CMT) detector, interferograms are first corrected for the nonlinear responsivity. This correction is especially important at elevated source temperatures (i.e at 150°C). The spectral responsivity and instrument self emission are then calculated according to equations (2.19) and (2.20). The functions are calculated at wavenumbers with high atmospheric transmittance, and interpolated between these data points to avoid distortions from strong absorption lines in the path between the blackbodies and the detector. In the wavenumber region above 3500 cm^{-1} the spectral responsivity is based upon a single measurement of a blackbody at high temperature (300°C) in the beginning of the trial. Variations in spectral responsivity during the trial is then not taken into account, and thus the absolute precision of calibrated spectra is reduced in this spectral region.

The FTIR spectral responsivity and self emission for the CMT detector configuration are shown in Figure B.1 and Figure B2. Figure B.3 and Figure B.4 show the same information for the InSb detector configuration.

As mentioned in section 4.2.2, significant variations in the calibration functions were observed during the SIMVEX trial. To illustrate this, we have included the results from two different runs in the figures. The reason for these variations is probably variation in instrument temperature due to sun and wind exposure as well as air temperature variations.

The reason for negative radiance values in some of the presented self emissions is that the contribution from the detector side of the beam splitter dominates over the source side contribution (section 2.2.1). The peculiarities in the functions at some wavenumbers are most probably due to some absorption in the instrument's beam splitter or another transmitting optical element.

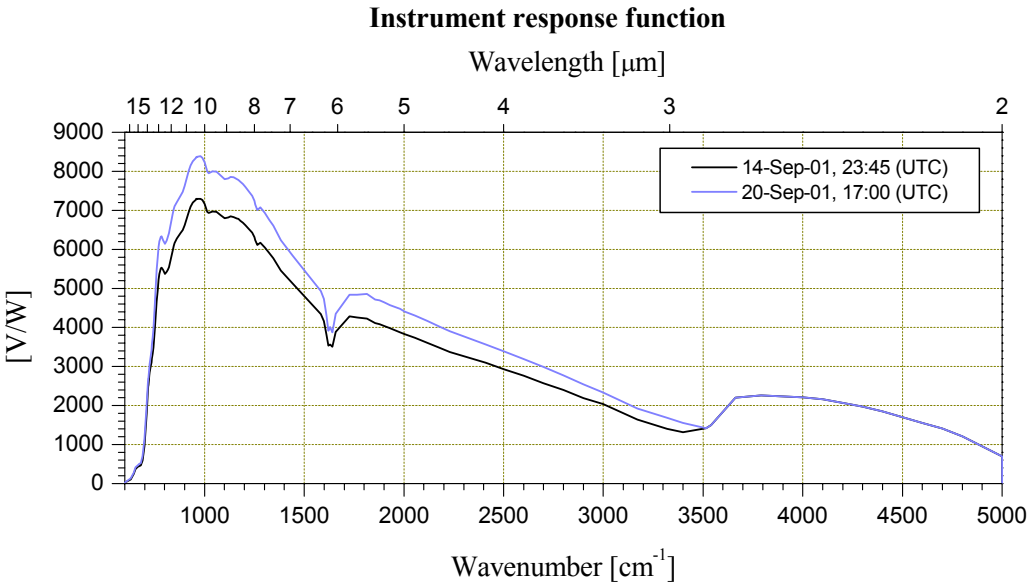

Figure B.1 FTIR spectral responsivity when the CMT detector is used

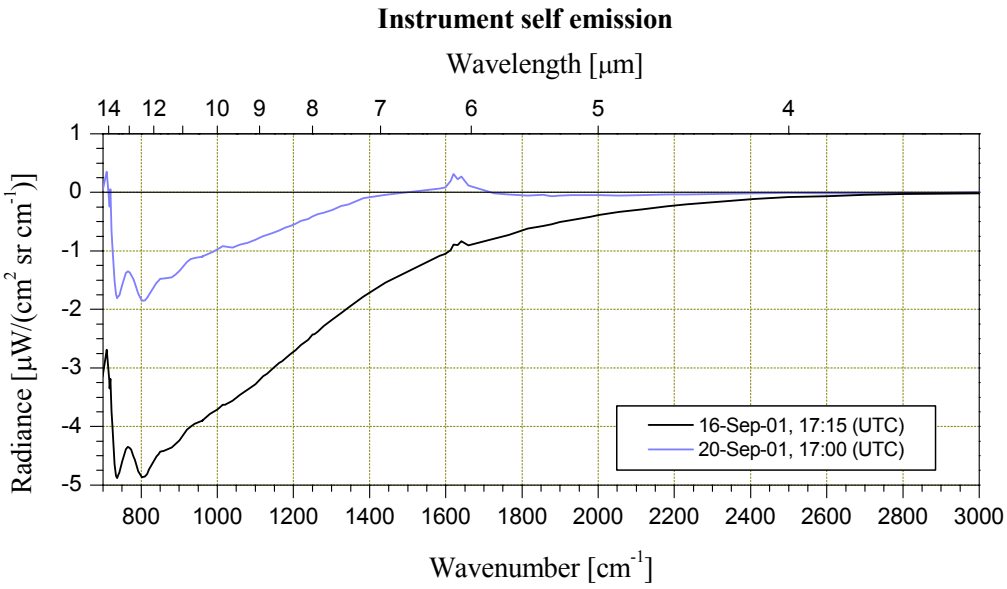

Figure B.2 FTIR self emission when the CMT detector is used

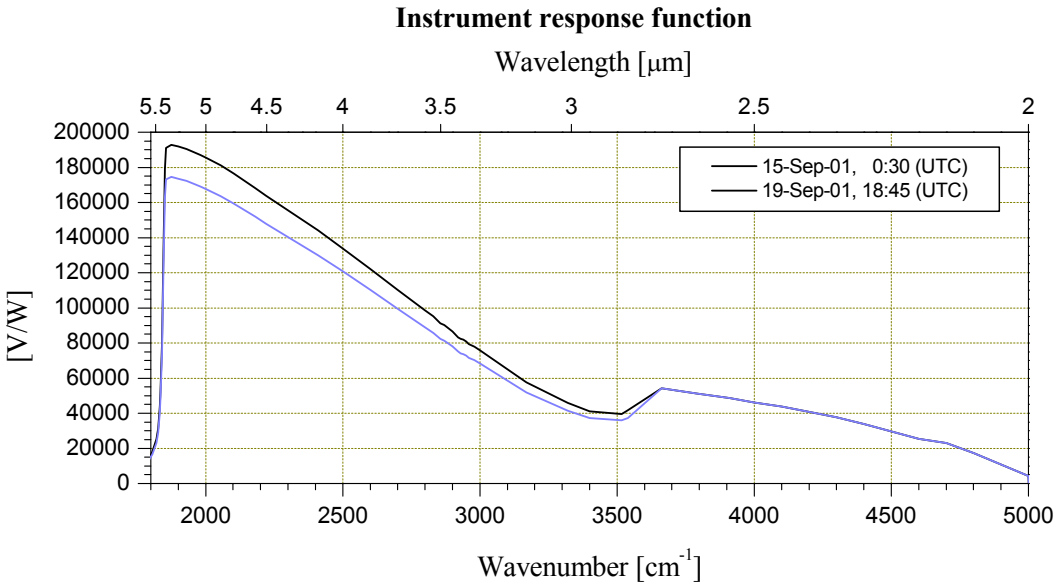

Figure B.3 FTIR spectral responsivity when the InSb detector is used

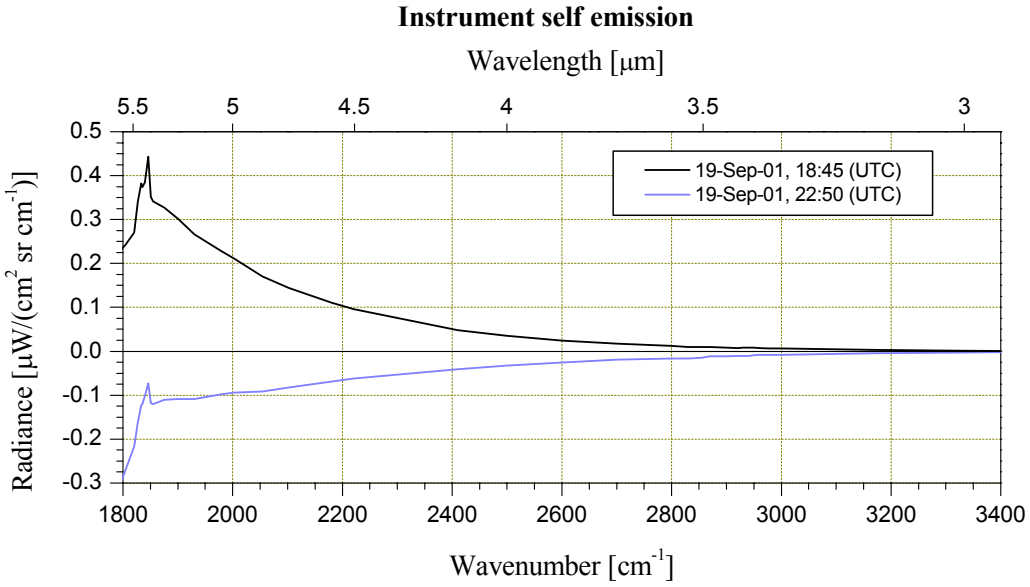

Figure B.4 FTIR self emission when the InSb detector is used

B.2 FTIR line shape function

The FTIR line shape function is defined as the spectral output from the instrument when a strictly monochromatic wave is applied as input; i.e the interferogram is an ideal sine-function.

Due to the selected optical path difference when real measurements are performed and apodization of the interferograms, the calculated spectral content of the result is a convolution of the spectral input radiation with the instrument's line shape function.

Figure B.5 presents the FTIR line shape function when an apodized sine-wave interferogram is Fourier transformed using exactly the same algorithm as for the measured results described in this report.

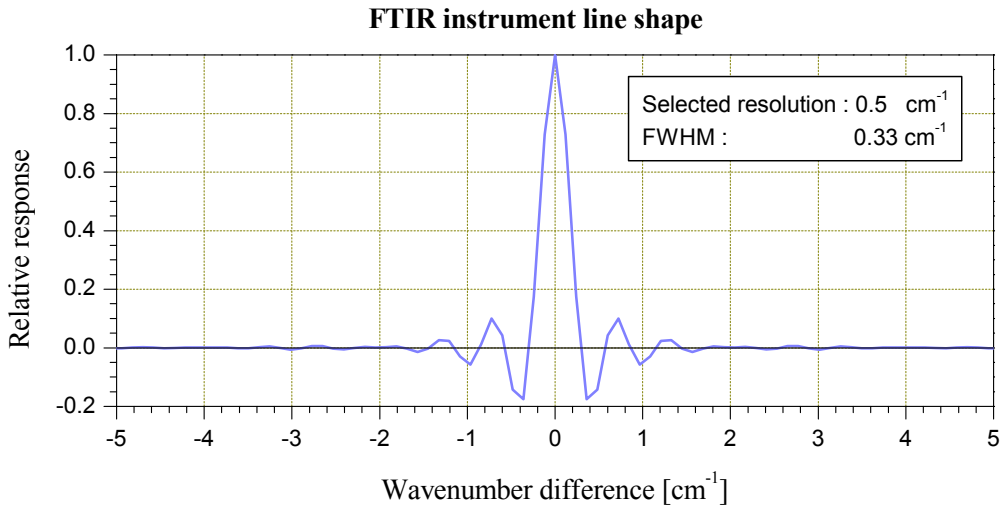

Figure B.5 Instrument line shape for the selected resolution given by the apodization function used for calculation of SIMVEX spectra

The figure shows the FTIR line shape function when the optical path difference used results in a spectral resolution of 0.5 cm^{-1} according to Bomem's definition (11). The discrete spectral interval between datapoints in the figure is 0.12 cm^{-1}, which is achieved by adding zeroes to the interferogram. The resulting line shape function has a full width at half maximum (FWHM) of 0.33 cm^{-1}.

Figure B.5 shows that the maximum under- and over-shoot is -17.5 % and +10 % respectively.

The resolution of 0.5 cm^{-1} was applied for all spectra presented in this report measured with the CMT detector, and some of the spectra measured with the InSb detector. To improve the signal to noise ratio most spectra measured with the InSb detector were calculated at a resolution of 0.8 cm^{-1}, and in some plume runs the resolution was 0.2 cm^{-1}. The FTIR line shape function at other resolutions than 0.5 cm^{-1} may be found from Figure B.5 simply, by scaling the wavenumber axis values by a factor

$$F_{res} = \frac{\sigma_{res}}{0.5\,cm^{-1}} \tag{B.1}$$

where

σ_{res} - resolution of the calculated spectrum

Dependent on the selected discrete spectral interval, the maximum under- and over-shoot may change a little compared to the values above.

The following comment apply to all spectral radiance results presented in this report: Every spectral feature in the input radiation, with a line width considerably smaller than the FWHM of the FTIR line shape function, will appear alike the FTIR line shape function in the presented results.

C FTIR SIGNAL TO NOISE PROPERTIES

The noise properties of the FTIR spectroradiometer was investigated by using a blackbody at ambient temperature after the SWG/4 trial in 1999, and the contents of this appendix is taken from (2). Spectra presented in this report have different Noise Equivalent Spectral Temperature Difference (NESTD) values, since the number of interferograms to be added, N is variable. The noise in a spectrum is proportional to $1/\sqrt{N}$. The numerical example below is based on N = 16. For most of the SIMVEX spectra N > 16, typical values are 25-40 for the ship and 64 for the backgrounds. This should give lower NESTD than the example shown. On the other hand absolute values for spectral reponsivity were lower during the SIMVEX trial than in 1999, which increases NESTD. As presented in appendix B, there were significant variations in the spectral responsivity during the trial, and the absolute values are generally 10-30% below the values used in the example.

The results from the investigation in 1999 showed that the noise rms value transformed to Noise Equivalent Spectral Radiance (NESR) could to a certain approximation be described by the following equations for the two detector configurations when the instrument mirror speed was 1 cm/s:

CMT:

$$NESR(\sigma) = \frac{0.106}{\sqrt{N\,\sigma_{res}}} \frac{R(\sigma_0)}{R(\sigma)} \frac{\mu W}{cm^2\, sr\, cm^{-1}} \quad ; \sigma_0 = 1000\, cm^{-1} \tag{C.1}$$

InSb:

$$NESR(\sigma) = \frac{7.7 \cdot 10^{-3}}{\sqrt{N\,\sigma_{res}}} \frac{R(\sigma_0)}{R(\sigma)} \frac{\mu W}{cm^2\, sr\, cm^{-1}} \quad ; \sigma_0 = 2000\, cm^{-1} \tag{C.2}$$

where

N - Number of interferograms added before the fourier transform is performed
σ_{res} - Spectral resolution
$R(\sigma)$ - Instrument's spectral responsivity (in V/W). For an ideal instrument and detector $R(\sigma_0) / R(\sigma) = \sigma / \sigma_0$

Numerical values for the instrument's spectral responsivity were given in B.1 for the two detector configurations.

The noise equivalent spectral radiance in equations (C.1) and (C.2) can be converted to a Noise Equivalent Spectral Temperature Difference (NESTD(σ)), which will be a function of the wavenumber. Assuming the source is a blackbody near atmospheric temperature (in most cases adequate for the ship surface and the sea background), NESTD(σ) is found by solving the following equation with respect to ΔT for different wavenumbers:

$$NESR(\sigma) = N_{BB}(\sigma, T_{atm} + \Delta T) - N_{BB}(\sigma, T_{atm}) \quad \text{(C.3)}$$

where

T_{atm} - Atmospheric temperature
N_{BB} - Spectral radiance from a blackbody

As an example equation (C.3) is solved for ΔT when T_{atm}=17°C, N=16 and σ_{res} = 0.5 cm^{-1}. The resulting noise equivalent spectral temperature differences are:

CMT:

$$NESTD(\sigma) = 0.26\,K \quad @\ \sigma = 1000\ cm^{-1} \quad \text{(C.4)}$$

$$NESTD(\sigma) = 4.1\,K \quad @\ \sigma = 2000\ cm^{-1} \quad \text{(C.5)}$$

$$NESTD(\sigma) = 60\,K \quad @\ \sigma = 3000\ cm^{-1} \quad \text{(C.6)}$$

InSb:

$$NESTD(\sigma) = 0.17\,K \quad @\ \sigma = 2000\ cm^{-1} \quad \text{(C.7)}$$

$$NESTD(\sigma) = 9.8\,K \quad @\ \sigma = 3000\ cm^{-1} \quad \text{(C.8)}$$

The implications of the results in equations (C.4) - (C.8) are that the measured parts of the ship must have an equivalent ΔT against the background at least 3-4 times the given NESTD(σ) values if the spectral radiance contrast between the ship and the background is to be

distinguished from the noise. This is normally accomplished with the CMT detector for wavenumbers around 1000 cm^{-1} but not for wavenumbers around 2000 cm^{-1}. With the InSb detector it is normally possible to distinguish the spectral radiance from the noise for wavenumbers around 2000 cm^{-1}. Similar considerations apply for distinguishing different parts of the ship surface. For typical SIMVEX runs it is possible to distinguish parts of the ship heated by sun from shaded parts at wavenumbers with low NESTD, but not possible to distinguish different parts of the ship during night runs.

DISTRIBUTION LIST

FFIE **Dato:** 11. desember 2002

RAPPORTTYPE (KRYSS AV)	RAPPORT NR.	REFERANSE	RAPPORTENS DATO
X RAPP ☐ NOTAT ☐ RR	2002/04911	FFIE/801/131	11. desember 2002
RAPPORTENS BESKYTTELSESGRAD		ANTALL EKS UTSTEDT	ANTALL SIDER
Unclassified		33	132
RAPPORTENS TITTEL		FORFATTER(E)	
SIMVEX 2001 TRIAL - SPECTRAL IR MEASUREMENTS		BRENDHAGEN Erik, HEEN Lars Trygve	
FORDELING GODKJENT AV FORSKNINGSSJEF		FORDELING GODKJENT AV AVDELINGSSJEF:	
Stian Løvold		Johnny Bardal	

EKSTERN FORDELING

ANTALL	EKS NR	TIL
		FO/SST
1		v/Kk Per Christian Borgen
		FLO/Sjø-T-VP
1		v/Kk Ove Rio
		FO/LST-LOI
1		v/Oblt Geir Ødegaard
		KNM T/SMOPS
1		v/Kk Trond Hermansen
1		v/Ok Rune Crowo
		FLO/Luft
1		v/Maj Geir Ove Nielsen
		FO/E
1		v/Rådgiver Asgeir Berg
		FLO/Sjø-P6026
1		v/Ok Hjalmar Johansen
1		v/Oing Jan Aasen
		KDA
1		v/Halfdan Glørud
1		v/Birger C Kommedal
		NATO RTO/SET/TG16
1		v/James Buss
		Elektronisk fordeling :
		ONR, USA
		v/James Buss
		Envisioneering, USA
		v/William Taczak
		NRL, USA
		v/Douglas Fraedrich
		DRDC-V, Canada
		v/Françoise Reid
		FGAN-FOM, Tyskland
		v/Anton Kohnle

INTERN FORDELING

ANTALL	EKS NR	TIL
9		FFI-Bibl
1		Adm direktør/stabssjef
1		FFIE
1		FFISYS
1		FFIBM
1		FFIN
1		Stian Løvold, FFIE
1		Egil Bingen, FFIE
1		Lars Trygve Heen, FFIE
1		Oddvar Selnes, FFIE
1		Erik Brendhagen, FFIE
2		Arkiv, FFIE
		Elektronisk fordeling:
		Øyvind Sjøvik, FFIE
		Kjell Wikan, FFIE
		Pål Steenfeldt-Foss, FFIE
		Eirik Ralm, FFIE
		Bernt Almklov, FFIE
		Eirik Blix Madsen, FFIE
		Erling M Sunde, FFIE
		Torbjørn Skauli, FFIE
		Ingebjørg Kåsen, FFIE
		Pål Erik Goa, FFIE
		Knut Stenersen, FFIE
		Espen Lippert, FFIE
		Randi Haakenaasen, FFIE
		Harald Hovland, FFIE
		Frode Berg Olsen, FFIE
		Morten Søderblom, FFIE
		Nils Greger Johansson, FFIE
		Arne Cato Jenssen, FFIE
		FFI-veven

FFI-K1 Retningslinjer for fordeling og forsendelse er gitt i Oraklet, Bind I, Bestemmelser om publikasjoner for Forsvarets forskningsinstitutt, pkt 2 og 5. Benytt ny side om nødvendig.

EKSTERN FORDELING

ANTALL	EKS NR	TIL
		DSTL, Storbritannia v/Keith Youern CTSN, Frankrike v/Bernhard Pezery Mariteleradar, Italia v/CDR Marco Scariot TNO Nederland v/Arie de Jong v/Wim de Jong FOFT, Danamark v/Henrik Vogel DSA, Portugal v/LCDR Clélio Ferreira Leite Hellencic Navy General Staff, Hellas v/CDR(E) Vassilios Flokas Arastirma Merkezi Komutanligi,Tyrkia v/Lt Emin Guven Naval Academy, Polen v/CDR Mariusz Zielinski WTD 71, Tyskland v/Jochen Stoehr QinetiQ, Storbritannia v/Marcus Wilson CISAM, Italia v/CDR Andrea Cini W. R. Davis Engineering Ltd, Canada v/David Vaitekunas Lockheed Martin, USA v/Melvin Parish ABB Bomem Inc, Canada v/Henry Buijs v/Luc Rochette Tromsø Tapet & Linoleumslager A/S v/Espen Stark www.ffi.no

INTERN FORDELING

ANTALL	EKS NR	TIL